

AD _____

Award Number: W81XWH-12-2-0055

TITLE: Sub-lethal Ocular Trauma (SLOT): Establishing a Standardized Blast Threshold to Facilitate Diagnostic, Early Treatment, and Recovery Studies for Blast Injuries to the Eye and Optic Nerve

PRINCIPAL INVESTIGATOR: Walter Gray, Ph.D

CONTRACTING ORGANIZATION: University of Texas at San Antonio
San Antonio, TX 78249

REPORT DATE: September 2014

TYPE OF REPORT: Annual Report

PREPARED FOR: U.S. Army Medical Research and Materiel Command
Fort Detrick, Maryland 21702-5012

DISTRIBUTION STATEMENT: Approved for Public Release;
Distribution Unlimited

The views, opinions and/or findings contained in this report are those of the author(s) and should not be construed as an official Department of the Army position, policy or decision unless so designated by other documentation.

REPORT DOCUMENTATION PAGE				Form Approved OMB No. 0704-0188	
Public reporting burden for this collection of information is estimated to average 1 hour per response, including the time for reviewing instructions, searching existing data sources, gathering and maintaining the data needed, and completing and reviewing this collection of information. Send comments regarding this burden estimate or any other aspect of this collection of information, including suggestions for reducing this burden to Department of Defense, Washington Headquarters Services, Directorate for Information Operations and Reports (0704-0188), 1215 Jefferson Davis Highway, Suite 1204, Arlington, VA 22202-4302. Respondents should be aware that notwithstanding any other provision of law, no person shall be subject to any penalty for failing to comply with a collection of information if it does not display a currently valid OMB control number. PLEASE DO NOT RETURN YOUR FORM TO THE ABOVE ADDRESS.					
1. REPORT DATE September 2014		2. REPORT TYPE Annual		3. DATES COVERED 15 August 2013 - 14 August 2014	
4. TITLE AND SUBTITLE Sub-lethal Ocular Trauma (SLOT): Establishing a Standardized Blast Threshold to Facilitate Diagnostic, Early Treatment, and Recovery Studies for Blast Injuries to the Eye and Optic Nerve				5a. CONTRACT NUMBER	
				5b. GRANT NUMBER W81XWH-12-2-0055	
				5c. PROGRAM ELEMENT NUMBER	
6. AUTHOR(S) Walter Gray, Matthew Reilly, Brian J. Lund, William E. Sponsel, Ralph D. Glickman E-Mail: ycnrtdtc@Bwu.cfw				5d. PROJECT NUMBER	
				5e. TASK NUMBER	
				5f. WORK UNIT NUMBER	
7. PERFORMING ORGANIZATION NAME(S) AND ADDRESS(ES) University of Texas at San Antonio San Antonio, TX 78249				8. PERFORMING ORGANIZATION REPORT NUMBER	
9. SPONSORING / MONITORING AGENCY NAME(S) AND ADDRESS(ES) U.S. Army Medical Research and Materiel Command Fort Detrick, Maryland 21702-5012				10. SPONSOR/MONITOR'S ACRONYM(S)	
				11. SPONSOR/MONITOR'S REPORT NUMBER(S)	
12. DISTRIBUTION / AVAILABILITY STATEMENT Approved for Public Release; Distribution Unlimited					
13. SUPPLEMENTARY NOTES					
14. ABSTRACT The report summarizes the results of tasks undertaken during Year 1 and 2 of the project "Sub-lethal Ocular Trauma (SLOT): Establishing a Standardized Blast Threshold to Facilitate Diagnostic, Early Treatment, and Recovery Studies for Blast Injuries to the Eye and Optic Nerve." The three year effort aims to fill a gap in our understanding of physical mechanisms and progression of primary blast-induced ocular injury. A fully-integrated experimental and computational study was undertaken. Blast experiments were conducted on 85 <i>ex vivo</i> porcine eye specimens and 13 <i>in vivo</i> rabbit eyes using a large diameter shock tube. The experiments were supported by numerical modeling using physics-based codes CTH and LS-DYNA. Post-blast evaluation of the porcine eye specimens using UBM and B-scan, as well as gross dissection and detailed histopathology, allowed for preliminary development of trauma risk curves for a number of sub-globe-rupture trauma categories. The shock tube produced a broad array of closed-globe injuries in the porcine eyes including angle recession, cyclodialysis, peripheral chorioretinal detachments, radial peripapillary retinal detachments, and internal scleral delaminations. Development of a rigorous experimental methodology as well as detailed statistical analyses gave confidence that the observed injuries were due to the effects of primary blast. Analysis of injuries to the <i>in vivo</i> rabbit eyes is ongoing.					
15. SUBJECT TERMS Ocular Trauma, Primary Blast, Shock Tube Experiments, Trauma Prediction, <i>ex vivo</i> Porcine Model, <i>in vivo</i> Rabbit Model, Numerical Modeling					
16. SECURITY CLASSIFICATION OF:			17. LIMITATION OF ABSTRACT	18. NUMBER OF PAGES	19a. NAME OF RESPONSIBLE PERSON
a. REPORT U	b. ABSTRACT U	c. THIS PAGE U			USAMRMC
			UU	84	19b. TELEPHONE NUMBER (include area code)

TABLE OF CONTENTS

	<u>Page</u>
1. INTRODUCTION.....	1
2. SUMMARY OF RESEARCH.....	6
2.1 Blast Experiments.....	6
2.2 Shock Tube.....	7
2.3 Aluminum Burst Disk.....	9
2.4 Porcine Eye Specimen Preparation.....	11
2.5 Porcine Eye Pathology.....	13
2.6 Statistical Analysis of Porcine Eye Blast Data.....	19
2.6.1 Statistical Methods.....	19
2.6.2 Injury Grades.....	20
2.6.3 Statistical Results.....	21
2.6.4 Effect of Porcine Eye Preparation.....	26
2.7 Porcine Trauma Data Analysis and Modeling.....	28
2.7.1 Univariate Logistical Regression.....	28
2.7.2 Ordinal Multinomial Regression.....	32
2.8 <i>In Vivo</i> Rabbit Blast Experiments.....	32
2.9 Biomarker Study.....	38
2.9.1 Biomarkers in Aqueous Humor and Blood Serum.....	38
2.9.2 Tissue Biomarkers of Trauma.....	39

2.9.3 Characterization of Trauma-related Proteins in a Model of Optic Nerve Trauma.....	40
2.10 Numerical Models & Simulation.....	44
2.10.1 LS-DYNA Model of the Porcine Eye.....	45
2.10.1.1 Model Validation.....	51
2.10.1.2 Model Predictions Compared to Experimental Data	52
2.10.1.3 Limitations of the FEA Model.....	56
2.10.2 CTH.....	56
3. KEY RESEARCH ACCOMPLISHMENTS.....	60
4. REPORTABLE OUTCOMES.....	61
5. CONCLUSIONS.....	63
6. REFERENCES.....	66
APPENDIX I Summary of Porcine Blast Experiments	70

1. INTRODUCTION

Blast-related injuries are commonly classified as primary (shock and air pressure effects), secondary (penetration from blast-driven fragments and debris), tertiary (blunt impact after blast acceleration), and quaternary (primarily heat and explosive gas toxicity). Penetration, contusion, and laceration by fragments and blast-driven debris (secondary) accounts for over 82% of all combat ocular injuries (Mader et al., 2004; Thach et al., 2008). Penetration-type injuries are readily observable so the trauma mechanisms are well documented and understood. However, a significant number of injuries may also result from explosive overpressure alone (primary blast) resulting in internal injuries that may not be easily recognized. Although blast injury and effects to major body organs have been reasonably well characterized (Bowen et al., 1968; Stewart, 2006; Stuhmiller, 2008a), primary blast-related trauma to the eye has not been extensively studied. The high incidence of ocular injuries relative to its small areal exposure suggests that the eye may be especially vulnerable to blast injury. It has been estimated that in the Iraq and Afghanistan conflicts eye injuries account for more than 13% of all combat injuries; the highest rate since World War I and the fourth most common injury among deployed personnel (Weichel et al., 2010). High energy blast weapons such as improvised explosive devices (IEDs) will become an ever increasing threat to U.S. military personnel in future conflicts, thus knowledge of primary blast effects on the eye takes on increased importance. Currently, protective eyewear available through the Military Combat Eye Protection Program (MCEP) provides ballistic or fragment protection, but not protection from the potentially harmful effects of blast overpressure. Thus, a large gap exists in our understanding of physical mechanisms and progression of blast-induced ocular trauma. This gap hampers our ability to extend the design of effective protective devices, and may contribute to ineffective treatment and rehabilitation due to inadequate awareness of potentially vision-threatening injury.

A non-penetrating blunt impact study conducted at Southwest Research Institute (SwRI) demonstrated that progression of ocular trauma is well correlated with impact energy (Gray, et al., 2008a; Gray et al., 2008b; Sponsel et al., 2011). The research showed that significant internal damage could occur without obvious external evidence. The study used porcine specimens as surrogates for the human eye and highly deformable paintballs to ensure that the impact energy was imparted to the eye without penetration. Until globe rupture occurred (~10 J) internal damage was not typically evident from external examination. However, detailed post-impact pathology revealed that, at significantly lower energies (2-7 J), internal trauma could be severe, including cyclodialysis, iridodialysis, angle recession, lens displacement, as well as retinal and choroid detachment. Using paintball mass (m_p) and velocity, an approximate correlation between impact energy ($E = \frac{1}{2}m_p V^2$) and trauma severity can be shown (Figure 1). The previous blunt impact study (Gray et al., 2008a; Sponsel et al., 2011) treated injury in a qualitative way, as there were insufficient test repetitions (at each injury level) to allow for estimation of ocular injury and incapacitation probabilities (at a given energy of impact).

Paintball Impact Ocular Trauma Thresholds (Porcine)

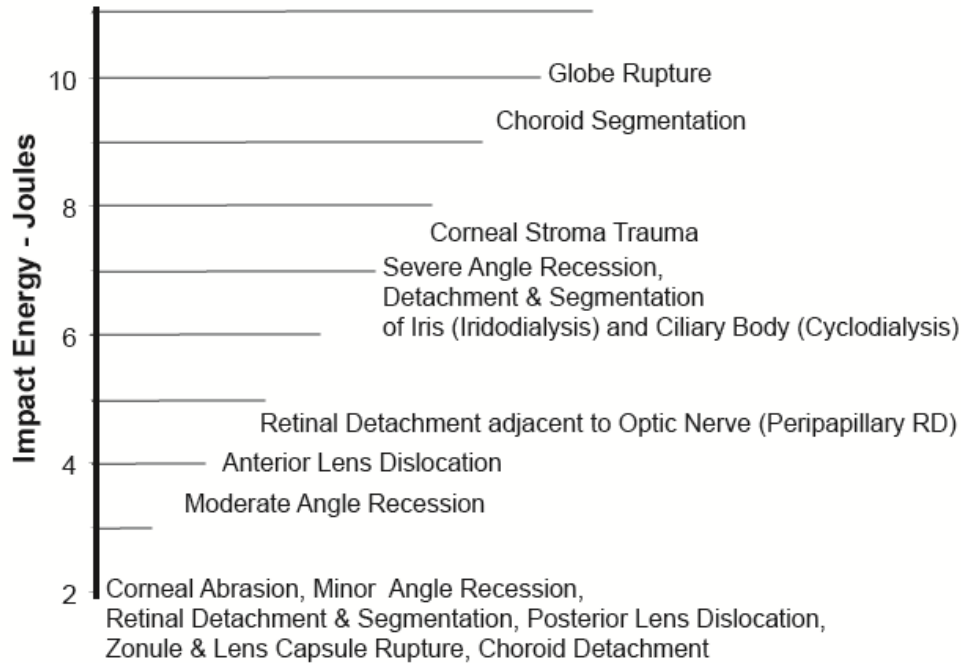


Figure 1. Qualitative trauma thresholds showing lowest energy level for which pathologic entities were observed. Trauma entities were obtained from results of a paintball blunt impact study on porcine eyes (Gray et al., 2008a; Sponsel et al., 2011). The plot illustrates the correlation between impact energy and trauma severity.

Similarly, it is expected that blast-induced ocular trauma should be equally well correlated with blast wave impulse (peak pressure and duration) producing the same types or categories of injury. This hypothesis is supported by results from previous whole-body blast trauma studies that generated the so-called Bowen Curves (Bowen et al., 1968). However, impulse can be roughly equated to incident energy (energy transmitted by the blast wave to the eye) through the relationship:

$$E = \frac{(iA)^2}{2m} \quad (1)$$

where i is the specific impulse (Pa-s) on the exposed area of the eye (A), and m is the mass of the eye specimen. In theory, characterization in terms of incident energy should allow for correlation of injury thresholds observed in primary blast studies with those previously observed in blunt impact studies (Figure 2).

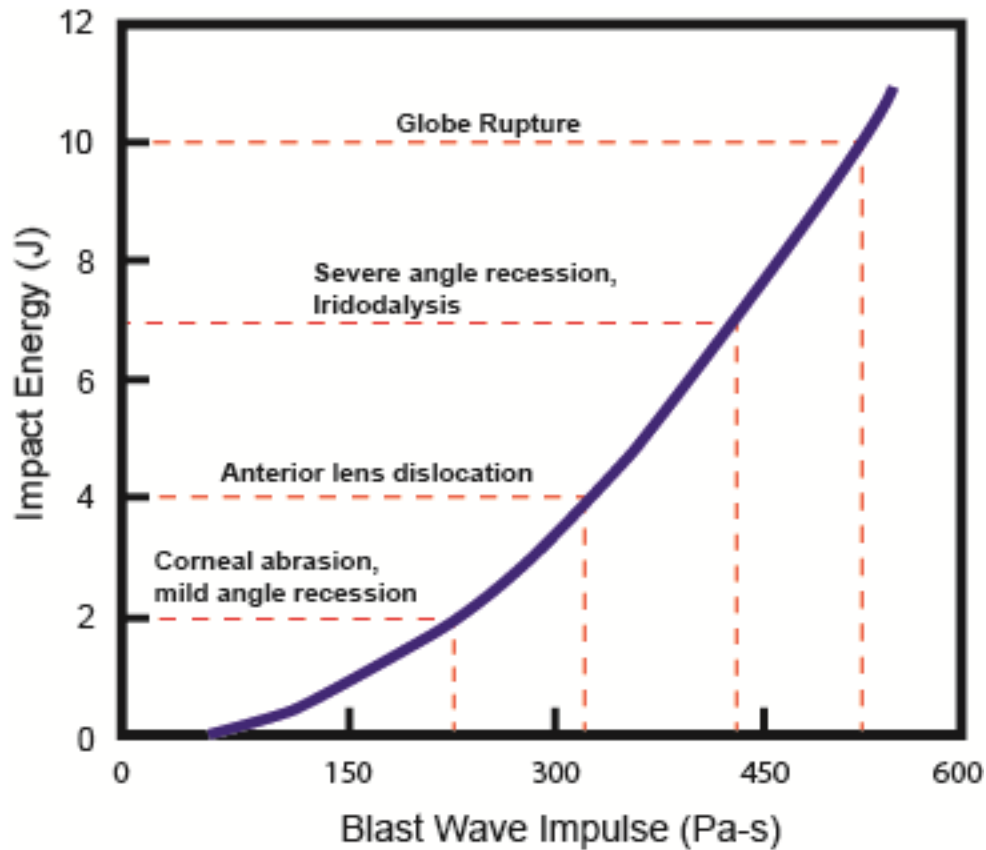


Figure 2. Plot showing hypothesized correlation between impact energy and blast wave impulse. Superimposed on the plot are the observed trauma thresholds from Figure 1 (paintball blunt impact study).

Although globe rupture has been used as the injury criterion in a number of previous blunt impact studies (Kennedy et al., 2004; Duma et al., 2005; Kennedy et al., 2006) the energy required to rupture the sclera is large (~ 9 to 10 J) compared to energy thresholds for less catastrophic but potentially serious injuries to the eye's soft inner tissues (Thach et al., 1999; Sponsel et al., 2011). These injuries typically require immediate surgery and numerous follow-up surgeries to prevent immediate or eventual loss of vision. Thach et al. (2008) estimated that approximately 45% of recent combat eye injuries are closed-globe-type injuries. Recent studies by Duma and Kennedy (2011) and Gray et al. (2008a) characterized closed globe injuries to eyes subjected to projectile blunt impact, but to date no such study has been conducted for primary blast. Thus there exists a significant gap in our knowledge of primary blast effects on the eye, especially internal injuries that occur in the non-lethal or sub-globe-rupture pressure regime.

The primary objective of this research effort is to address this knowledge gap by experimentally identifying sub-globe rupture injury mechanisms and their progression with increasing blast energy and impulse. Blast experiments are being conducted using

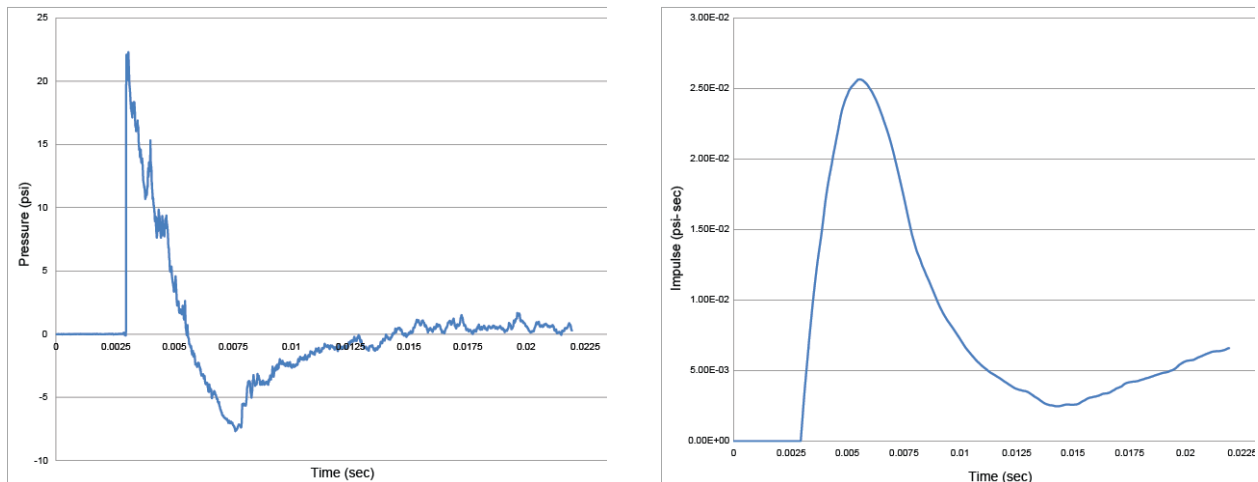


Figure 3. Typical Friedlander waveform (left) and specific impulse (right) for ISR shock tube apparatus. Specific impulse is calculated by time integration of the waveform.

the U.S. Army Institute of Surgical Research (ISR) large diameter shock tube. This device has the capability to reliably produce blast overpressure with the characteristic Friedlander waveform typical of explosive detonation (Figure 3). Integration of the measured pressure-time traces provides the required impulse information. Experiments have increased in complexity from *ex vivo* porcine eyes in Year 1 of the study to *in vivo* rabbit eyes in Year 2. Use of the *in vivo* rabbit model will allow for biochemical marker monitoring and characterization. Although physical trauma is the primary focus, the chemical biomarker assessment in Year 2 will allow correlation of observed physical trauma with more subtle chemical indicators.

In addition to ocular trauma, it is anticipated that results of the biomarker study will provide fruitful pathways and directions for future research aimed at understanding blast-induced traumatic brain injury, its recognition, and early treatment. The general approach being taken is a systematic investigation to determine if biomarkers associated with TBI are also present in the experimental animals with blast-induced ocular trauma. The presence of the biomarkers will be probed in samples of aqueous fluid and blood. All of the protein biomarkers of interest can be measured using Luminex-based, xMAP multiplexed assay panels. Typically 30 microliters or less (sometimes as little as 10 microliters) of sample are required for each multiplexed assay, so this method is very well suited for the limited sample volumes available of ocular fluids. Ocular fluids can be sampled with minimal disturbance to the eye, enabling serial sampling over the course of the study. If the selected biomarkers are present in the ocular and/or serum samples, their amounts will be measured by xMAP assay in eyes subjected to increasing levels of standardized impact severity (as established in the other aims of this research program) to determine if a correlation between biomarker amounts and injury severity exists. The time course of biomarker appearance after injury onset will be characterized. The correlation of the biomarker in the ocular samples with the circulating (serum) levels will also be determined.

In addition to the use of the commercial xMAP bead-based assays, we are exploring the use of Matrix Assisted Laser Desorption Ionization (MALDI), an “imaging” technique for direct detection of protein *in situ*, particularly in optic nerve specimens. This methodology not only determines the sequence of proteins or protein fragments, but also identifies the spatial localization of proteins in a tissue sample. A section of the tissue is prepared for the laser assisted matrix desorption process, then the activating laser is stepped across the tissue in a raster pattern. The intensity of the ejected ions (specifically, the mass/charge or m/z ratio) is plotted as a function of the position of the laser beam on the tissue. The map of ion location produces an “image”, thus mapping the location of the protein being analyzed. This approach may be particularly productive in analyzing biomarkers in optic nerve sections taken from traumatized eyes.

Experiments are accompanied by computational analysis using physics-based codes CTH and LS-DYNA. One of the invaluable lessons learned in previous blunt impact studies was that numerical simulations have the potential to identify physical mechanisms responsible for otherwise unobservable and unexplained phenomena (Gray et al., 2008a, 2011). Realistic geometrical and tissue constitutive models of external and internal eye structures are being developed for implementation into CTH and LS-DYNA. Co-development of models for both codes allows us to avoid limitations presented by each code. The objective here is to use CTH in the initial stages of the shock interaction (i.e., the first few μ sec), where it can produce the initial boundary condition inputs for LS-DYNA. LS-DYNA will then be used to simulate long-term deformation (msec to sec). The simulations carefully mimic the experiments with the goal of fully reproducing the trauma observed in the experiments. The validated models will allow for analytical extension into impulse regions unattainable with the shock tube experiments. The models will be invaluable in characterizing the physics of tissue response, design of protective eyewear, and virtual measurement of physical parameters not measurable in the experiments.

Extensive use of *in situ* imaging technologies is being employed for pre- and post-blast assessments. In-house studies of impact trauma have shown that pre- and post-impact B-scan and UBM ultrasound imaging help differentiate blast-induced trauma from fixative artifact. Scanning abattoir eyes from a posterior approach allows cilio-lenticular imaging with B-scan, and peripapillary/macular assessment with UBM, greatly increasing the diagnostic specificity of the histopathology studies. Gross globe deformation that occurs during the blast will be documented using bidirectional high-speed digital video.

The project will culminate in Year 3 with development of trauma predictive models. The data generated during the experiments will be used to formulate empirical models useful in predicting the probability of observing a number of sub-globe-rupture injuries under various blast pressure-impulse or energy environments. We envision that the model will consist of a series of curves in peak pressure-impulse space, similar in form to those used to predict whole-body response to blast (Richmond and White, 1962; Richmond et al., 1966; Bowen et al., 1968; Richmond, et al., 1985; Proud et al., 2009). The utility of such models has been adequately demonstrated by the wide use of

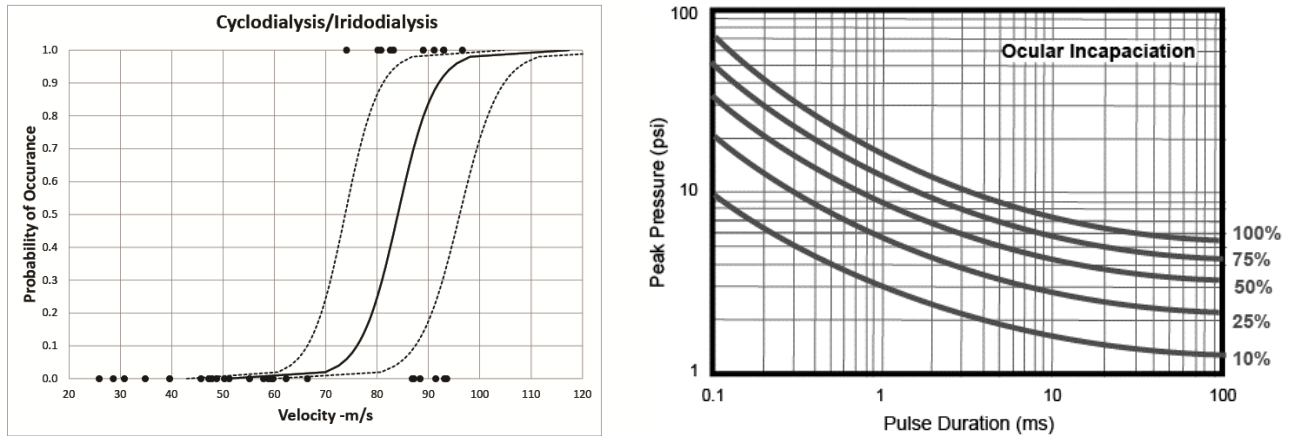


Figure 4. Probability of injury curve (risk function curve) for projectile blunt impact (left). Example of proposed ocular incapacitation chart based on medical assessment of the overall impact of cumulative ocular injuries on the warfighters ability to carry out his mission (right).

Bowen-type curves (whole body response to blast) in a number of warfighter survivability, lethality, and vulnerability (SLV) models. Individual curves will reflect the probabilities of observing such injuries as angle recession, iridodialysis/cyclodialysis, scleral rupture, etc (Figure 4). In addition to physical injury curves, medical assessments will be performed on the individual injuries and combinations of injuries to develop qualitative curves detailing level of soldier ocular incapacitation (as a function of the blast pressure-impulse condition), typically a more useful tool for first responders and warfighters (Figure 4).

2. SUMMARY OF RESEARCH

2.1 Blast Experiments

A total of 85 blast experiments on enucleated porcine eye specimens, and 13 blast experiments on *in vivo* rabbits have been conducted to date. All blast experiments were conducted at the ISR Shock Tube Laboratory (STL) located at Joint Base San Antonio, San Antonio, TX. Porcine eyes were exposed to 6 peak blast overpressure levels of approximately 35, 85, 115, 135, 155, and 230 kPa. The rabbits were exposed to 3 peak blast overpressure levels of approximately 55 kPa, 85 kPa, and 130 kPa.

All 85 porcine eyes were examined for damage, but 43 were excluded from the subsequent statistical analysis for a variety of reasons including avulsion from the orbit mimic during blast, placement of the orbit-mimic at a different depth within the shock tube's expansion cone (resulting in an unknown blast pressure value), improper maintenance of pre-blast IOP, and lack of pre-blast screening. The remaining 42 blast-exposed eyes, plus 13 controls, constituted the set of 55 eyes assigned grades of trauma. Commonly observed injuries included angle recession, internal scleral

delamination, cyclodialysis, peripheral chorioretinal detachments and radial peripapillary retinal detachments. The most frequently observed injuries in all grades were angle recession and chorioretinal detachments. The most common tissues experiencing severe damage were the sclera (delaminations) and retina (detachments). Some control eyes also exhibited damage, usually involving the angle, choroid, and retina.

Corneal epithelial disruption was observed ubiquitously in exposed and control porcine eyes, and, thus, was not included in our analysis. Macroscopic injury of the iris occurred infrequently and no obvious examples of pupillary sphincter rupture were observed in eyes lacking pupillary sphincter tone. Anterior segment uveal damage generally was restricted to the angle, where it was common. Anterior lens capsular damage also was not observed, but zonular dehiscence was noted along with some posterior capsular ectasia in multiple instances. Scleral ruptures were not observed.

Although preliminary, post-blast examination of 18 *in vivo* rabbit eyes (13 exposed to blast, and 5 controls) has revealed minimal trauma at the relatively low blast levels used in the experiments (55-130 kPa). Some retinal edema has been observed in fundus images and OCT measurements of the retinal thickness are being examined to confirm this qualitative finding. No sphincter ruptures or retinal detachment have been observed.

2.2 Shock Tube

Blast exposure testing at the STL was accomplished using a 17-inch diameter compressed air driven shock tube (Figure 5). The eye specimen and acrylic holder (orbit mimic) were placed within the expansion cone of the shock tube and isolated from the driver section by a series of thin (.016 inch thick) aluminum disks. Pressurization of the driver section causes the disks to rupture, sending a Friedlander-style pressure wave down the tube toward the eye specimen. The peak pressure of the shock wave is controlled by the number of disks. Experiments have been performed using from 1 to 6 aluminum disks resulting in peak pressures from approximately 48 kPa (7 psi) to 152 kPa (22 psi). In addition, experiments have been conducted at a pressure levels lower than 48 kPa by using a 0.007-inch thick mylar disk. Peak pressures up to 241 kPa (35 psi) were achieved by moving the eye-orbit mimic further axially into the expansion cone, while peak pressures as low as 21 kPa (3 psi) were achieved using a single 0.010-inch thick mylar disk.

Each blast experiment was documented using high-speed videography at 15,000 frames/second using a Fastcam Ultima APX (Photron USA, Inc; San Diego, California). Blast overpressure (static or side-on pressure) was recorded using piezoelectric pressure transducers (Model 137A23; PCB Piezotronics, Inc; Depew, New York). Stagnation pressure (reflected or total pressure) was recorded with a Kulite pressure transducer (Model XTL-190; Kulite Semiconductor Products; Leonia, New Jersey) as shown in Figure 6. Both pressure probes were factory calibrated with appropriate

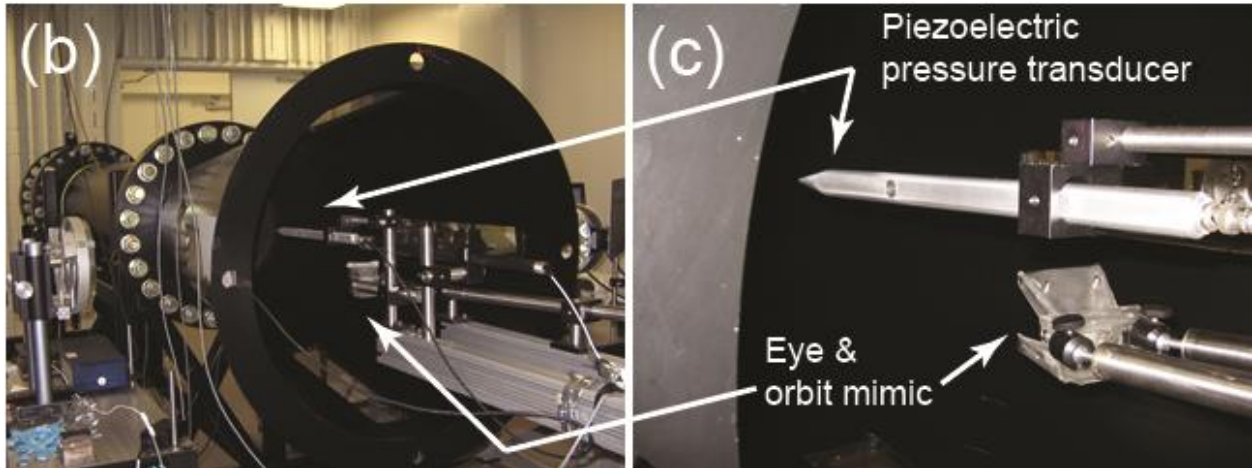
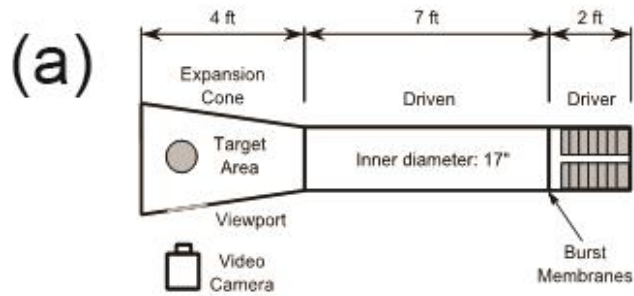


Figure 5. US Army Institute of Surgical Research shock tube showing location and orientation of eye and holder (orbit mimic) along with piezoelectric pressure transducer. A shock wave is created by pressurizing the driver section until the burst membranes ruptures. The target area lies within the expansion cone. Exposures of the pig eyes were recorded using an ultra-high speed video camera looking through an open viewport on the side of the expansion cone.

certificates of conformance provided by the manufacturer. Pressure signals were recorded at 200,000 samples per second using a Synergy P Data Acquisition System (Hi-Techniques, Inc.; Madison, Wisconsin). The pulse duration of each experiment was taken as the point where the initially positive phase of the wave form reaches zero pressure, i.e., the negative phase of the waveform is ignored (Figure 3). The specific impulse is calculated by time-wise integration of the entire waveform.

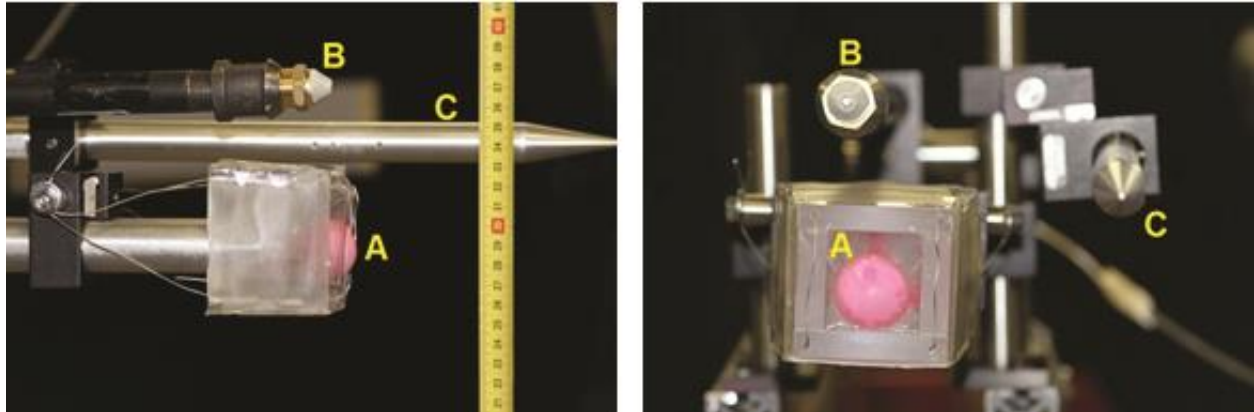


Figure 6. Arrangement of target and pressure sensors used to investigate physical effects of primary blast waves on the eye. A) Water-filled balloon (as substitute for eye) embedded in gelatin, and mounted in acrylic eye socket mimic. B) Pressure sensor to measure total pressure. (Kulite XTL-190 pressure transducer) C) Pressure sensor to measure overpressure (PCB Piezoelectronics Model 137A23 ICP Blast Pressure Sensor).

2.3 Aluminum Burst Disk

Initial experiments were conducted using burst disk made from 0.016 inch thick 3003-H14 aluminum sheet supplied by McMaster-Carr of Chicago, Illinois. The material was purchased as rolls from which disks of approx. 20" diameter were cut for use in the shock tube. The 3003 alloy is not heat treatable but is supplied in a strain hardened condition achieved by cold working. The H14 designation indicates that the material received a $\frac{1}{2}$ temper, i.e., reduction in hardness of approximately 50%. Reduction of hardness is undertaken to increase the alloys ductility and toughness. Single sheets burst at a pressure of 60 psig forming a series of roughly symmetric petals separating from the center of the disk (Figure 7a). This behavior created blast pressure time profiles that were consistent with the expected Friedlander waveform. Approximately 70 successful experiments were conducted with this batch of material.

However a later batch of material failed by tearing in a very nonsymmetrical pattern at approximately 20 psig, less than half the expected pressure (Figure 7b). This behavior produced a nonsymmetrical pressure-time profile that did not achieve the steep initial pressure rise associated with Friedlander waveforms. As this type of waveform was deemed unacceptable for blast testing, shock tube experiments were suspended pending resolution of the issue. In response to inquiries from ISR personnel, McMaster-Carr indicated that the aluminum supplier changed the processing procedure for the aluminum sheet in order to be in compliance with a recent change in material standards. However, they were unable to provide any insight as to why this affected the aluminum's burst behavior.

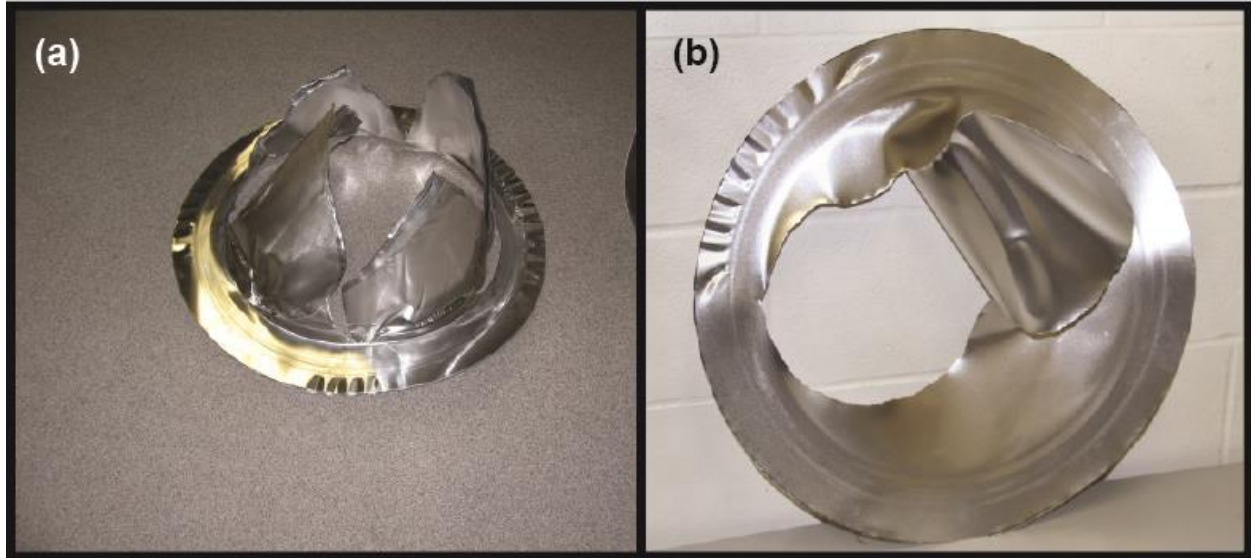


Figure 7. (a) The initial batch of 3003-H14 aluminum sheet burst at a pressure of 60 psig forming a series of roughly symmetric petals separating from the center of the disk. (b) The latest batch of aluminum sheet failed by tearing in a very nonsymmetrical pattern and at approximately 20 psig.

Further inquiries to metallurgist at Southwest Research Institute (SwRI) revealed that changes in cold working procedures can greatly affect material failure characteristics, especially if rolling directions and associated grain boundary orientations are altered. They indicated that failure behavior in cold worked materials is difficult to predict and control, and consistency difficult to maintain. Their recommendation was to pick a heat treatable alloy and experimentally recalibrate for the desired pressure and burst characteristics.

In support of the alternate aluminum alloy search, a series of LS-DYNA numerical simulations were undertaken. Based on recommendations from SwRI, our efforts focused on two alloys, 2024-T4 and 6061-T6. Each alloy was simulated in LS-DYNA using a preexisting non-linear material model (Material 24-piecewise linear plasticity), and a stress-strain curve to define the behavior of the material. Stress strain curves for the alloys were obtained from various internet sources (Figure 8a). Each simulation assumed that the burst disk was 20 inches in diameter, 0.016 inches thick and constrained all around its periphery. The disk was then loaded uniformly with by a slowly rising pressure (consistent with pressurization in the shock tube driver section) until failure occurred. Failure of the material is modeled by input of the alloys maximum plastic strain (Figure 8b). The LS-DYNA results suggested that alloy 6061-T6 would fail at driver pressures similar to those observed in previous successful tests.

Based on recommendations from SwRI, Applied Research Associates (ARA), and LS-DYNA simulation results, we procured sheets of 6061-T6 aluminum for further investigation. Preliminary testing revealed that scoring the aluminum disk (scratching a shallow groove in the metal) prior to pressure loading was an effective technique to

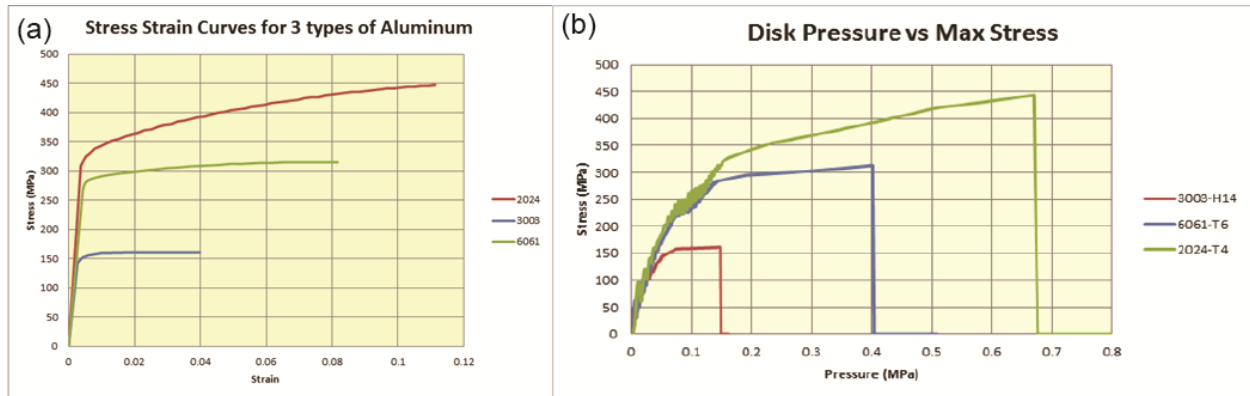


Figure 8. (a) Typical stress vs. strain curves for 3003, 2024, and 6061 aluminum alloys. (b) LS-DYNA predictions as to the failure stress and burst pressure for 3003-H14, 6061-T6, and 2024-T4 aluminum disks.

control the initial failure mode and location when the disks burst. During experiments in the shock tube, we were able to consistently force the aluminum disks to split into two large clam-shell-like pieces, thus eliminating the fragmentation hazard. The initial burst pressure was reasonably consistent, allowing us to effectively control the test conditions. Further testing revealed that the new burst disk configuration produced consistent and acceptable Friedlander waveforms. As an added precaution, a clam-shell catcher was fabrication and installation inside the shock tube just upstream of the driver section.

2.4 Porcine Eye Specimen Preparation

Enucleated porcine eyes, including eyelids and extraocular muscles, were purchased from Animal Technologies, Inc. (Tyler, Texas) and shipped overnight on wet ice. All animal tissues were handled in accordance with the ARVO Statement for the Use of Animals in Ophthalmic and Visual Research and protocols approved at each institution. The superior sclera was first marked using a surgical marker based on eyelid position to allow repeatable identification of locations on each eye. Skin, muscles, eyelids, and fatty tissues were removed to expose the surface of the globe, then placed in Hanks Balanced Salt Solution (HBSS; Fisher Scientific; Hampton, New Hampshire) and transported to the pathology laboratory.

Despite transfer on ice, the hydraulic conductivity of the scleral membrane and the necrotic state of the tissue, rendered the initial the intraocular pressure (IOP) of the porcine eyes low. Evidence for this was the observed flaccid cornea, soft eyewall, and failed readings from our Tono-Pen VET (Dan Scott & Associates; Westerville, Ohio). It was often necessary to re-inflate the porcine eyes to a normal level (10-20 mmHg) with HBSS before scanning and blast testing. We found that injections at the pars plana increased the fluid content of the posterior chamber, allowing subsequent anterior chamber injections to maintain a normal IOP. At the pathology laboratory, each eye

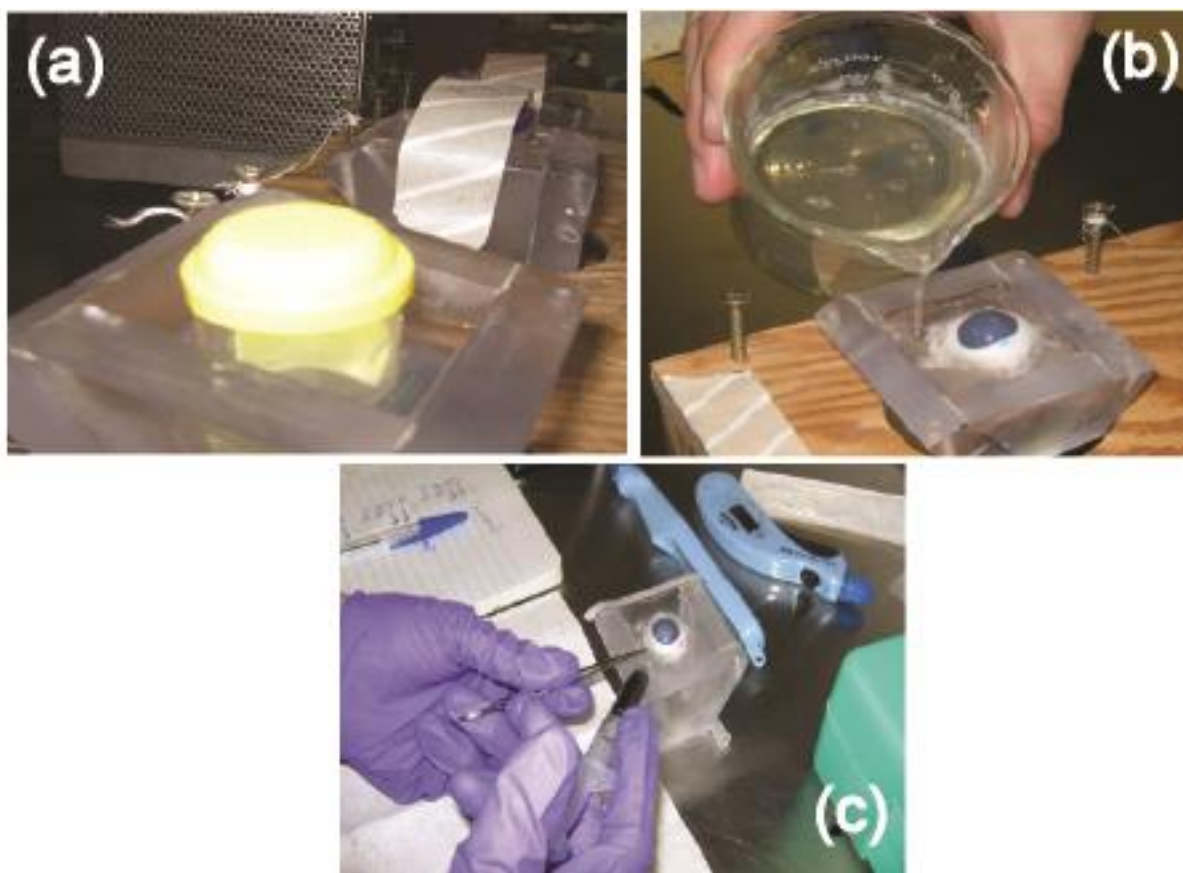


Figure 9. (a) Gelatin is preformed into acrylic holders that simulate the interior dimensions of the orbit. (b) Eyes are oriented and set within the preformed gelatin and sealed in place. (c) Just prior to blast testing, HBSS is injected in to the anterior chamber at the pars plana. The needle is inserted nearly parallel to the corneal surface in an attempt to provide for some degree of self-sealing once the intraocular pressure is raised.

was re-inflated via pars plana injection of HBSS using a 30 gauge needle until the IOP was between 10-20 mmHg as determined by the Tono-Pen. B-scan (Compact Touch; Quantel Medical; Bozeman, Montana) and ultrasound biomicroscopy (UBM; OIS-100; i-Science Interventional; Menlo Park, CA) were used to assess the condition of each pressurized eye prior to blast exposure. B-scans were taken from 3 to 9 o'clock, 6 to 12 o'clock, and 9 to 3 o'clock axially and posterior near the optic nerve to visualize the anterior chamber. UBM was used to image each eye from pars plana, equator, and peripapillary regions from clock hours 12, 3, 6, and 9. Eyes were rejected from the study if pre-exposure pathology was observed during this pre-screening process. After screening, eyes were stored refrigerated (4°C) overnight in HBSS then transported to the shock tube laboratory. Several acrylic orbital mimics were fabricated with internal dimensions and geometry similar to the orbital structure (Sponsel et al., 2011; Kennedy et al., 2007; Weaver et al., 2010). A plastic cup with spherical bottom (diameter roughly equivalent to the porcine globe) was placed in the center of the orbital mimic and the remaining internal volume filled with a 3.6 % liquid gelatin mixture (Knox Gelatin; Kraft Foods; New York, New York) which was cooled overnight prior to delivery of the eyes

(Figure 9a). This 3.6% gelatin has been shown to provide nearly equivalent mechanical strength as the periorbital fat and surrounding tissues (Yoo et al., 2011).

Each eye was re-inflated via pars plana injection with HBSS and set in place of the plastic cup within the gelatin. Additional liquid gelatin was then poured around the eye filling the holder to the top (Figure 9b). The eye and orbit mimic was then refrigerated for approximately 30 minutes to fully set the gelatin. During refrigeration, each eye was covered with parafilm to prevent dehydration of the specimen.

Just prior to blast exposure HBSS was injected into the anterior chamber via a shallow angle through a 30-gauge needleport paracentesis tangential to the limbus in the peripheral cornea (Figure 9c). The eye-orbit mimic assembly was then photographed and placed into a rigid mount inside the shock tube. Once secured, the IOP was measured again and recorded. The eye-orbit mimic was tilted 20 degrees laterally to simulate the convergence of the human eye and placed 25 cm into the expansion cone of the shock tube. The test chamber was cleared, the driver section of the shock tube pressurized, and the blast test conducted.

For each day of testing, this procedure was repeated for several exposed eyes and one control eye. The control eye was treated in an identical fashion to the test eyes, i.e., placed into the expansion cone for several minutes but never subjected to an actual overpressure. After the test, IOP was measured and recorded; the eye-holder assembly was removed from the rigid mount, and another series of photographs taken. The eye specimen was then removed from the gelatin and placed into a HBSS-filled container. The containers were then transported in small plastic containers on ice to the pathology laboratory for blind post-test damage assessment.

Upon arrival at the pathology laboratory, another corneal HBSS injection was used to raise the IOP to between 10-20 mmHg through a 30-gauge needleport paracentesis tangential to the limbus. Trauma damage to each eye was then evaluated and documented using a combination of B-Scan and UBM ultrasound imaging along the meridians and directions examined previously. The specimens were then placed in formalin in preparation for detailed examination via manual dissection (in which the anterior surface was removed with a diamond knife) or histological analysis. Anterior chamber and optic nerve status were further assessed via stained paraffin sections of a subset of specimen eyes representing controls and blast-exposed eyes. Additional eyes were used in preliminary testing to develop the methods described above. Approximately 10% of eyes received for study were excluded because the B-scan and UBM ultrasonic pre-screening demonstrated the presence of pre-existing damage to the eye.

2.5 Porcine Eye Pathology

Using terminology consistent with the Ocular Trauma Classification Score (OTCS, Pieramici et al., 1997), the majority of ocular injuries resulting from blast exposure were found to be lamellar injuries. Probability of injury was found to increase with peak

overpressure in Zone 1 (external surface; $p=0.024$) and Zone 3 (internal posterior segment; $p=0.023$) while no significant correlation was found in Zone 2 (interior anterior segment $p=0.6242$). Injuries included angle recession, cyclodialysis, peripheral chorioretinal detachments, radial peripapillary retinal detachments, and internal scleral delamination. No full-thickness openings of the eyewall (scleral rupture) were observed in any of the eyes tested. A summary of preparation and exposure information for the 60 eyes is provided in Appendix I. The peak pressure was not independent of the duration of the positive phase: as the peak pressure increased, the duration increased as well (Figure 10). Any type or level of trauma observed in the subject area (i.e., angle, choroid, etc.) is reported in that category regardless of the severity. Corneal abrasion was ubiquitously observed in exposed eyes and so was not counted in the linear regression analysis. Macroscopic injury of the iris and anterior chamber occurred infrequently and was generally restricted to the angle. The increase in severity and occurrence of injury did not appear to be a deterministic event, but the results support the idea that certain ocular tissues are more sensitive to increases in blast energy than others. The retina appears to be the very sensitive to increasing blast energy. The sclera demonstrated the strongest associative tendency for increasing injury with increased overpressure (Figure 11). Remarkably, at very high levels of overpressure (>300 Pa-s) the injury quotient for the sclera and the various other ocular tissues tested returned to control eye values. Angle injuries also showed a bell-curve response, with injuries beginning to appear at the 50 Pa-s level and tapering back to baseline at 200 Pa-s. There was no obvious impulse threshold value for the appearance of lower-grade injury to any ocular structure, but there were such thresholds in evidence for more extreme damage levels readily apparent for the optic nerve (~ 125 Pa-s), anterior chamber (~ 100 Pa-s), and sclera (~ 90 Pa-s; Figure 12).

Pathology– Zone 1: Scleral delamination and multiple chorioretinal detachments were observed before fixation using B-scan and UBM, and were confirmed through dissection and histopathology. Figure 11a shows a chorioretinal delamination following exposure to 138 kPa (20 psi) blast. Figure 11b shows a detachment in an eye that was exposed to 113 kPa (16 psi) blast. These lamellar lacerations occurred in multiple meridians. UBM scans also showed significant chorioretinal disruption with the probe oriented equatorially (Figure 13a) and with probe oriented postero-anteriorly (Figure 13b) following exposure to 38 kPa (5.5 psi) blast. One of the strengths of using UBM was the ability to place the probe in the same location before and after blast testing. Figure 14 shows three eyes exposed to three different peak pressures. Figure 14b shows an eye exposed to a peak pressure of 152 kPa, which caused significant delamination of the chorioretina. Figure 14c shows an eye that was exposed to a peak pressure of 134 kPa. Figure 14f shows an eye that was exposed to a peak pressure of 126 kPa, which caused the retina to detach and crumple.

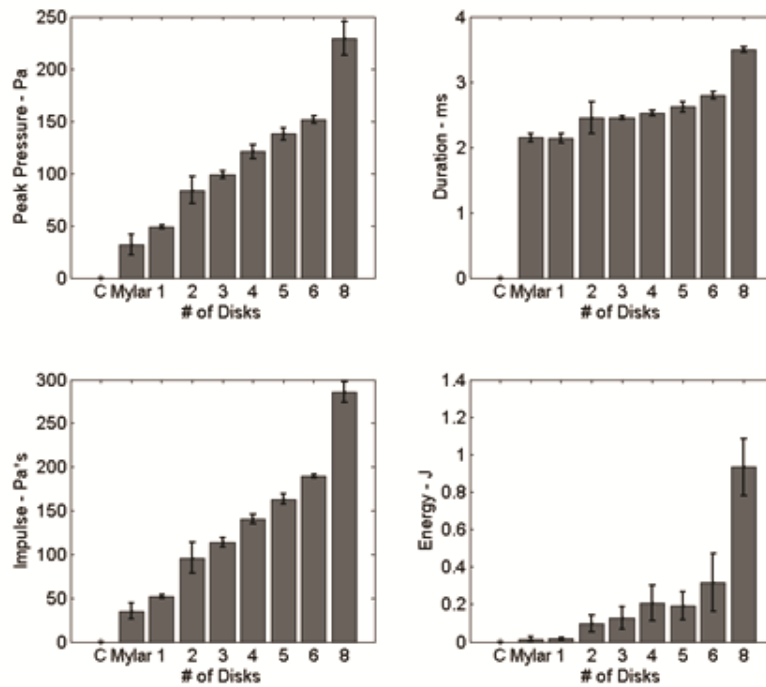


Figure 10. Histogrammic representation of the association of the number of mylar or aluminum disks secured between the pressure chamber and shock tube and peak pressure (upper left), duration (upper right), impulse (lower left), and energy (lower right)

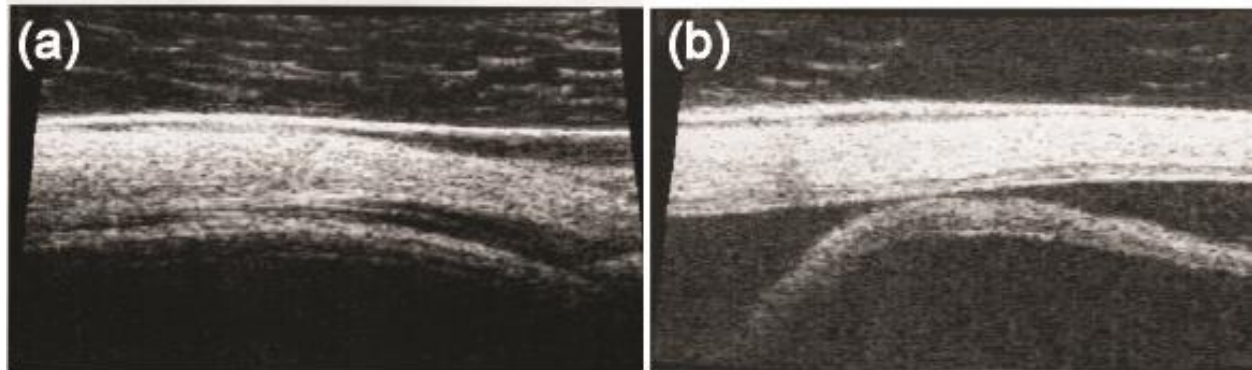


Figure 11. Scleral delamination and multiple chorioretinal detachments were observed before fixation using B-scan and UBM, and were confirmed through dissection and histopathology. Scleral delamination (a) following exposure to a 138 kPa (20 psi) blast, and extensive chorioretinal detachment and, (b) in eye exposed to a 113 kPa (16 psi) blast.

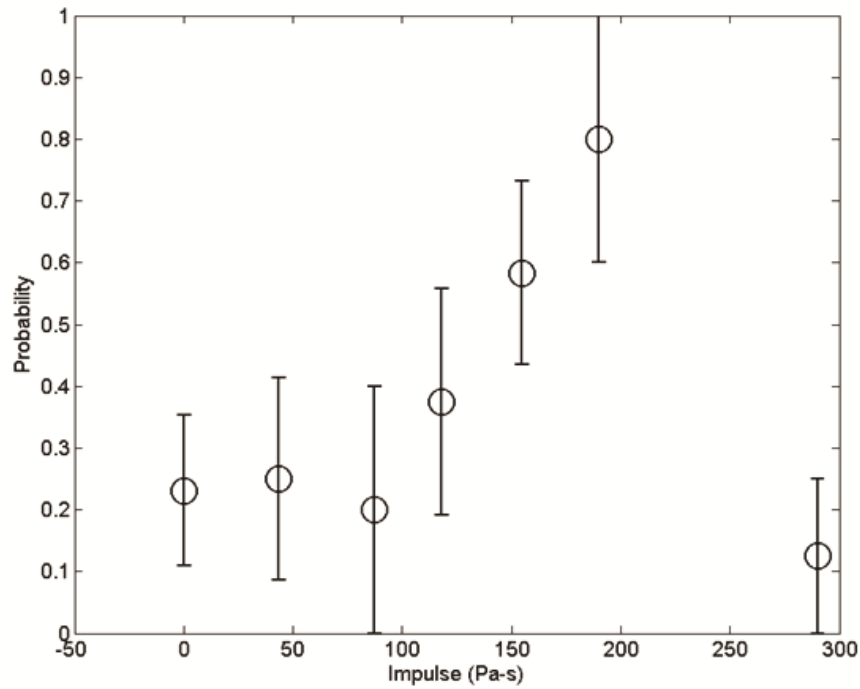


Figure 12. Histogram showing the probability of scleral injury for a given impulse level. Delamination accounted for nearly all observed scleral trauma. Note that the likelihood of injury increased to around 200 kPa (29 psi) above which the probability returned to that of the controls. While the exact mechanism underlying this observation is unknown, similar probability peaks have been observed in other ocular tissues within the present study. A numerical model of the blast may elucidate the underlying cause of this counterintuitive finding.

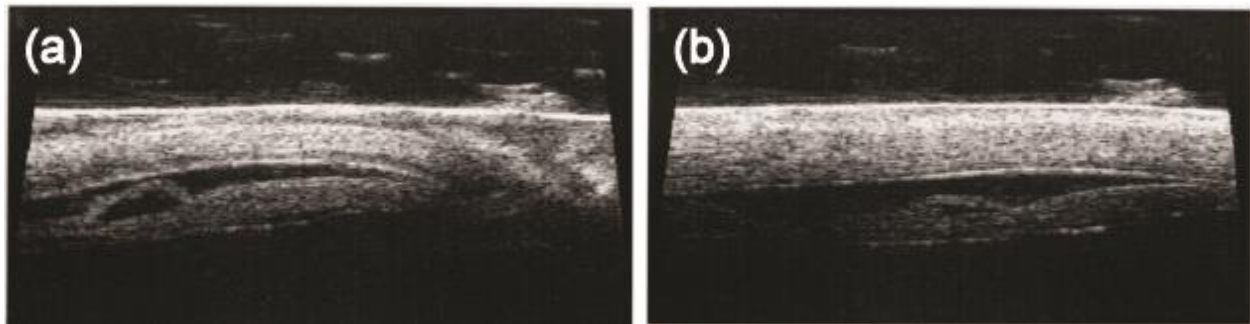


Figure 13. UBM shows significant chorioretinal disruption with probe oriented equatorially (a) and postero-anteriorly (b) following exposure to a 38 kPa (5.5 psi) blast.

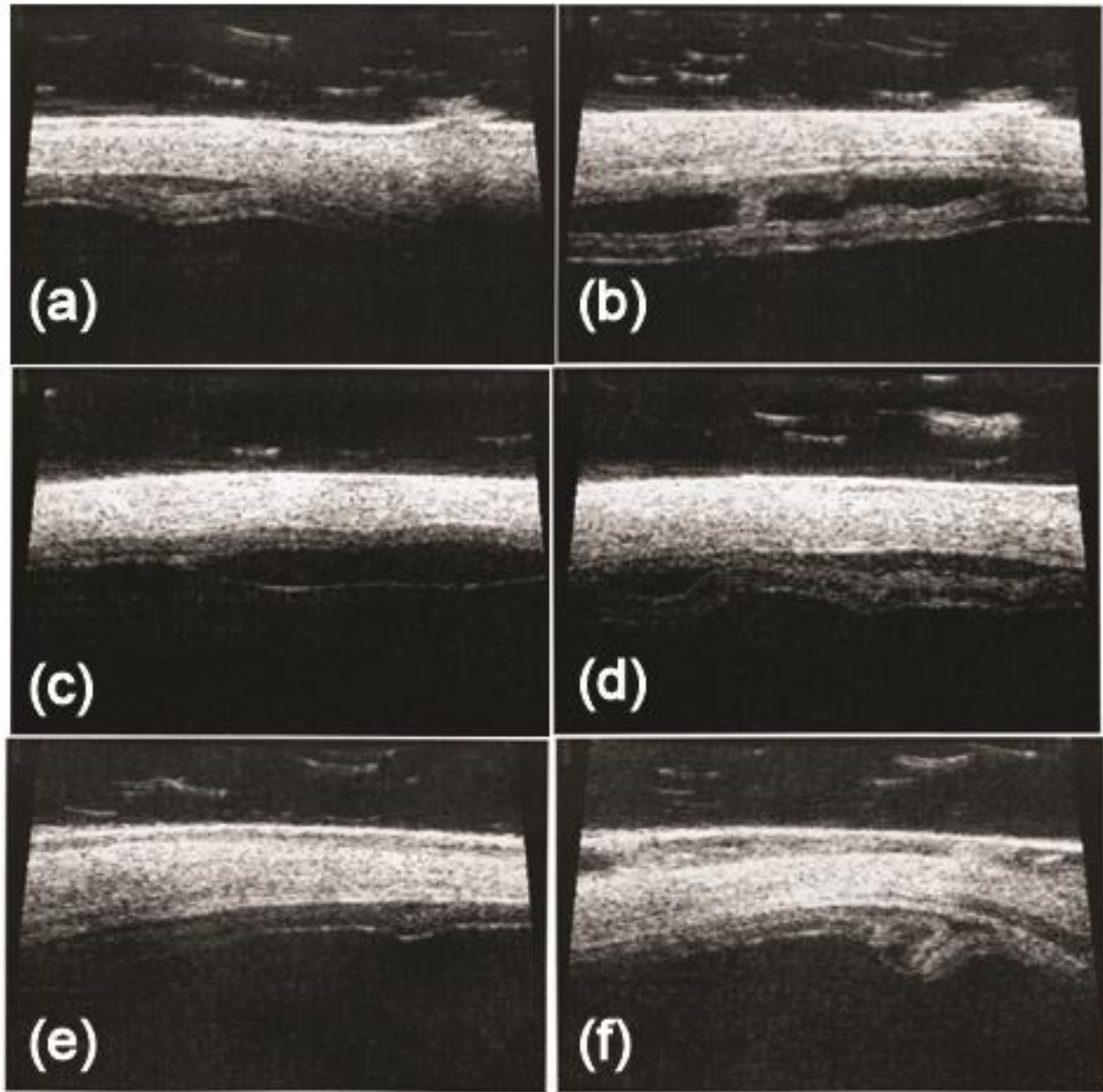


Figure 14. UBM scans of eyes exposed to three different peak pressures showing typical delamination injuries observed after blast exposure. (a, b) severe delamination of the chorioretina after exposure to a peak pressure of 152 kPa, (c, d) similar but less severe injury after exposure to a peak pressure of 134 kPa, and (e, f) detachment and crumpling of retina after exposure to peak pressure of 126 kPa.

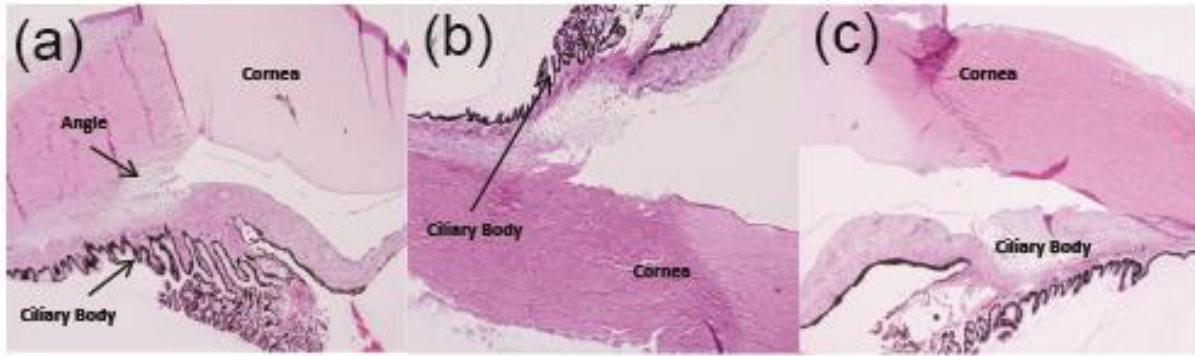


Figure 15. Histopathology of the porcine eye angle in (a) a control eye, and (b, c) eyes exposed to 113 kPa (16 psi) blasts. Both angle recession (b) and cyclodialysis (c) were observed. Significant damage to the angle was commonly observed even after low peak overpressure exposures.

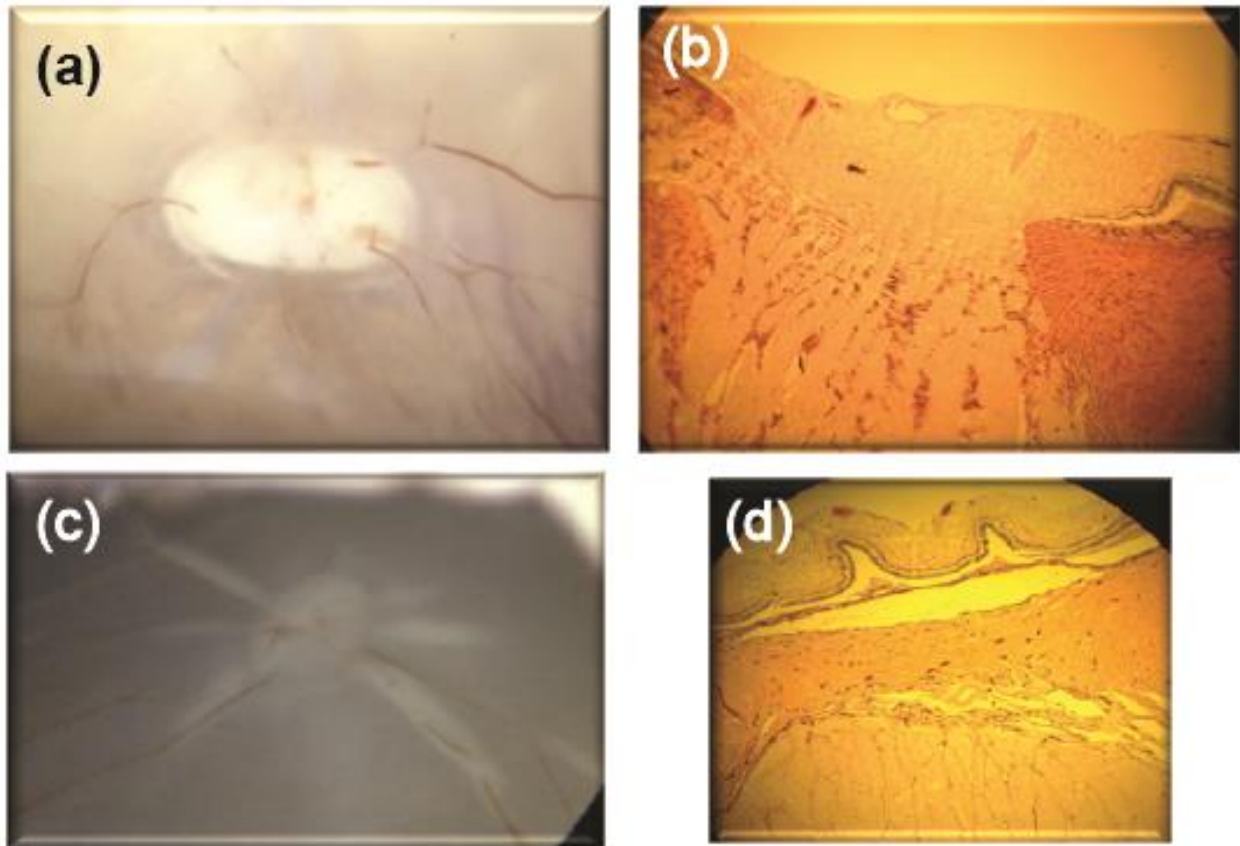


Figure 16. Images of the optic nerve head (ONH) taken during manual dissection (above) and from histopathology (below). (a) Control eye showing clear ONH as viewed through the vitreous after removal of the anterior chamber. (b) Eye exposed to 207 kPa (30 psi) blast shows retinal elevations coinciding with the location of blood vessels originating from ONH as viewed through the vitreous after removal of the anterior chamber. (c) Control eye section shows normal ONH and surrounding tissues. (d) Eye exposed to 126 kPa (18 psi) blast shows retinal folding in the immediate vicinity of blood vessels. Such injuries may be due to rapid oscillations in the tissue following blast exposure and may induce large strains in the region of density gradients such as at the blood vessel-retina interface.

Pathology– Zone 2: Angle obliteration was observed via histopathology after the eye was exposed to peak overpressure of 113 kPa (16 psi; Figure 15). UBM was generally unable to resolve this injury. However, histopathology revealed the angle as a common location for injury, even for porcine eyes exposed to low peak overpressures.

Pathology– Zone 3: Images of the optic nerve head (ONH) were taken during manual dissection and from histopathology (Figure 16). The ONH of the control eye was normal when viewed through the vitreous after removal of the anterior chamber. The ONH of an eye exposed to a 207 kPa (30 psi) blast showed retinal elevations coinciding with the location of blood vessels originating from ONH as viewed through the vitreous after removal of the anterior chamber. Examples of such injuries may be due to rapid oscillations in the tissue following blast exposure. Such oscillations could induce large strains in regions with density gradients such as at the blood vessel-retina interface.

2.6 Statistical Analysis of Porcine Eye Blast Data

While the data provided clear evidence of damage due to primary blast (with increased damage as pressure and impulse increased) statistically relevant damage was also observed in some control eyes. This finding leads us to question whether the specimen preparation methodologies may have had some effect on the observed post-test damage. Thus, in order to more clearly identify specimen preparation effects, as well as place the blast trauma results in a clearer context, a detailed statistical analysis of the results was undertaken.

2.6.1 Statistical Methods

Ordinal Logistic Regression – Because the injury grade takes on values 0-4 (see Section 2.6.2) the injury categories are *ordinal* data, as each category contains the previous categories. Common practice for injury risk assessment is to apply the log cumulative odds model. This model assumes that all slopes of the different response levels are equal and thus estimates the individual intercepts for each response level with a common estimated slope. The odds model is:

$$\text{logit}[P(Y \leq j)] = \ln\left(\frac{P(Y \leq j)}{P(Y > j)}\right) = a_j + \beta x \quad \text{for } j = 1, \dots, J - 1$$

where P is the probability, j is the individual injury grade (0-4), J is the number of injury grades (5), Y is the response, a_j is the respective intercept, and β is the respective slope. The slope (β) is also designated as the odds ratio. The odds ratio gives the percent chance of moving from one injury grade to the next with each additional unit of a given predictor.

Multinomial Logistic Regression- When it is inappropriate to apply the ordinal logistic regression, it is necessary to use multinomial logistic regression. Here the log odds are

not cumulative. Instead evaluation with respect to a baseline or reference category, for example:

$$\text{logit}[P(Y = j)] = \ln\left(\frac{P(Y = j)}{P(Y = J)}\right) = a_j + \beta x \quad \text{for } j = 1, \dots, J - 1$$

These models were run in JMP Pro 10[®] with the most relevant predictors selected using the stepwise ordinal logistic regression and the p-threshold option. The stepwise algorithm explicitly tests whether the selected model offers improved correlation relative to a reduced model with no effects (Whole Model test). Once the algorithm ceases to enter or remove predictors, simple ordinal logistic regression was performed on only the relevant predictors. Lack of fit (of the relevant predictors) was then evaluated using both the Wald Effects Test and Likelihood Ratio Test. These tests determine which relevant predictors in the model were statistically significant, i.e., β is different from zero. The test statistic for the Wald Test is simply:

$$Z^* = \frac{b_k}{s\{b_k\}}$$

Where b_k is the estimated slope and $s\{b_k\}$ is the standard deviation. The test statistic for the Likelihood Ratio Test G is:

$$G = \sqrt{-2 \ln \left[\frac{L(R)}{L(F)} \right]}$$

where $L(R)$ is the likelihood function for the reduced model and $L(F)$ is the likelihood function for the fitted model. Small ratios of $L(R)/L(F)$ (i.e. large values of G^2) lead to rejection of the null hypothesis.

2.6.2 Injury Grades

Based on results of post-blast ultrasound, UBM, and histopathology, a surgical ophthalmologist from William E. Sponsel Associates evaluated each porcine eye (regardless of whether it was treated with overpressure or used as a control) for signs of trauma. The ophthalmologist noted the existence, type, and severity of internal or external damage. To ensure accuracy, the ophthalmologist was blind to the eye's exposure status and pre-blast condition. Levels of trauma were designated as none, mild, moderate, or severe for the ultrasound and histopathology data separately, then combined into injury grades on a scale of 0-4 (Table 1, Figure 17). Note that the assigned grade also contains injuries indicative of previous or lower grades. Thus the grading scale is cumulative in nature.

Table 1. Injury Severity Grade

Injury Severity	Observation
Grade 0	No injury observed
Grade 1	One to two significant but mild pathologic defect(s) not present in the pre-impact images for the anatomic tissue/entity being scored
Grade 2	One moderate <u>or</u> One moderate and one mild <u>or</u> Three mild pathologic defects
Grade 3	One severe defect <u>or</u> Two to three moderate defects <u>or</u> Two moderate and any mild defects <u>or</u> Four or more mild pathologic defects
Grade 4	Two or more severe defects <u>or</u> One severe and any number of moderate defects <u>or</u> Four or more moderate defects <u>or</u> Three moderate and any number of additional mild defects

Mild defect is defined as one affecting less than $1/16^{\text{th}}$ of the maximal available area for injury of the tissue on the two-dimensional viewing plane. The moderate defect is one affecting from $1/16^{\text{th}}$ to $1/8^{\text{th}}$ of the available area for injury of the tissue on the two-dimensional viewing plane. Lastly, severe defect is one affecting more than $1/8^{\text{th}}$ of the available maximal area for injury of the tissue on the two-dimensional viewing plane. Although the pathology was classified according to OTCS zones, some zones had fewer or greater kinds and severities of injury making it more appropriate to describe injury in terms of the tissue type or ocular structure. Thus the injury categories used for this study were (1) Angle, (2) Choroid (3) Optic Nerve Head, (4) Retina, and (5) Sclera.

2.6.3 Statistical Results

Logistic regression was performed on pathology and injury grade data associated with the injury categories choroid, retina, optic nerve head, angle, and sclera. The predictors selected for correlation analysis came from two distinct groups; (1) blast parameters, and (2) preparation parameters. The blast parameters were defined by the

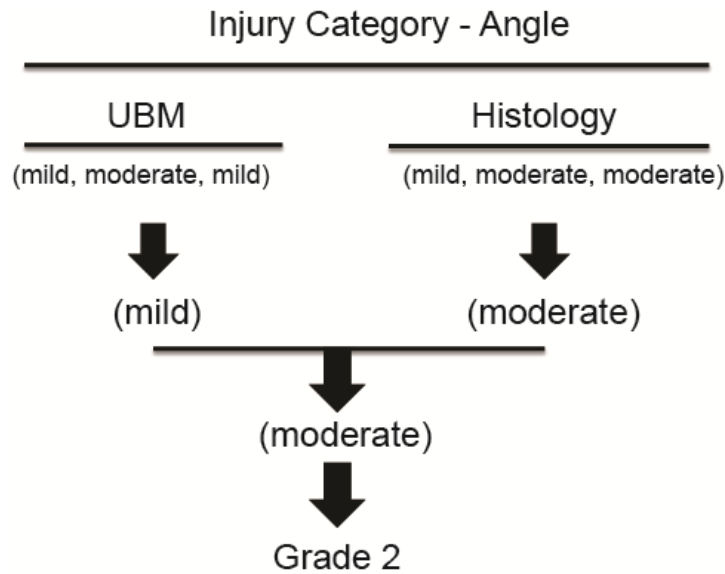


Figure 17. Illustration of combined injury grades from UBM and Histology Observations

Friedlander waveform and include positive impulse, positive phase duration, negative phase duration, peak positive pressure, minimum pressure in the negative phase, and pressure difference, i.e., difference between peak positive pressure and minimum pressure (see Figure 18 for explanation). Preparation parameters included mass of the eye, induced IOP, and pre-IOP. Induced IOP is the pressure recorded after HBSS injection and just prior to setting the eye in the orbit mimic and gelatin. Mass of the eye is the as-received porcine eye mass plus the injected HBSS. Lastly, the pre-IOP is the pressure recorded after loading into the shock and just prior to the blast event. Stepwise ordinal regression with a p-value threshold stopping rule and parallel/proportional odds assumption was performed using JMP Pro 10[®] to identify the most relevant predictors (blast or preparation parameters) for each injury category. To appropriately measure the level of significance for the implicated predictors, the Bonferroni Correction was applied. Thus, the nominal significance threshold ($\alpha=0.05$) was divided by the total number of predictors to give an adjusted threshold ($\alpha = 0.0125$). This new alpha was used as the threshold for significance. The predictors selected as relevant were then subjected to simple ordinal logistic regression with Wald and Likelihood Ratio tests used to assess significance of correlations through calculated p-values.

Retina - Only positive phase duration was identified as being significant. The measure of lack of fit returned a large chi-squared value (5.735) and the whole model is significant ($p=0.0166$). Simple ordinal logistic regression for this single parameter showed $p=0.0197$ for the Wald Test and $p= 0.0166$ for the Likelihood Ratio Test, revealing that positive pulse duration is correlated with damage incidence in the retina. The p-values for the intercepts cumulative Grades 2 & 3 is significant, but not for cumulative Grades 0 & 1. As the positive duration of the shock-wave increases, the probability of incurring a Grade 3 reaches a maximal value and then attenuates. The

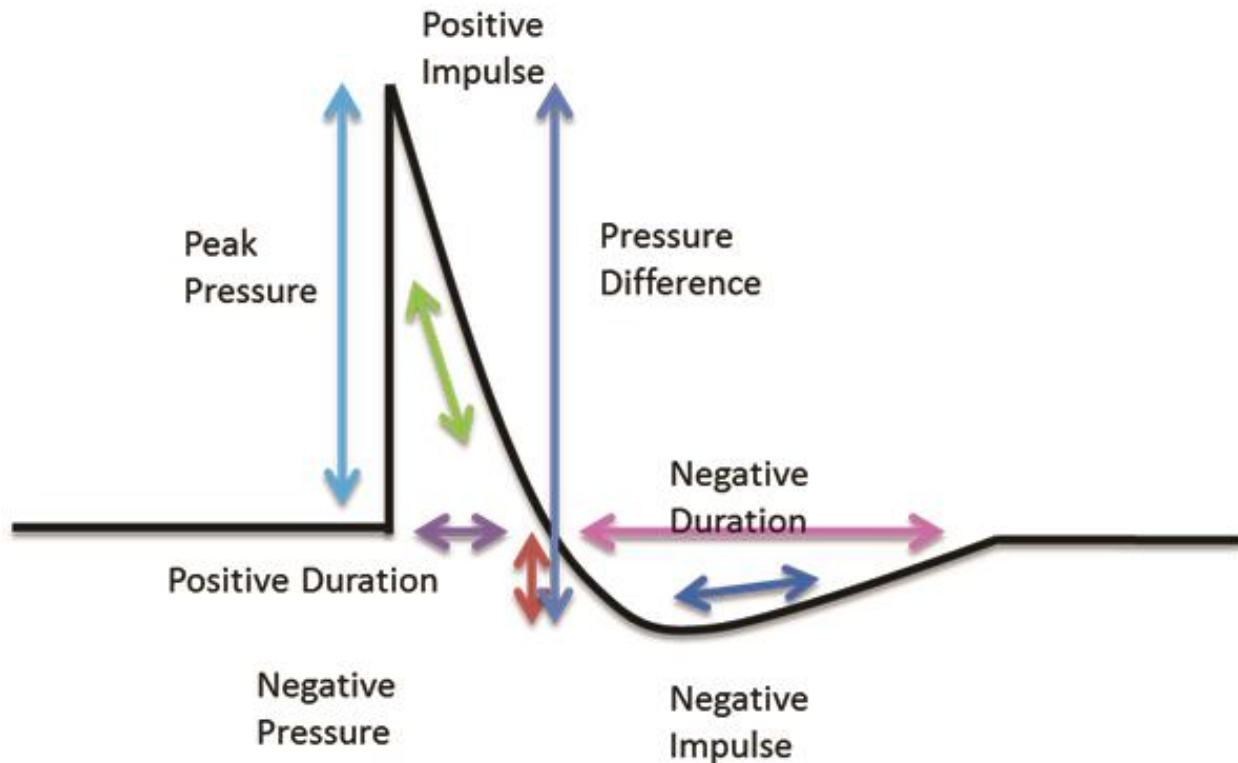


Figure 18. Blast parameters defined by the Friedlander waveform.

probability of incurring a Grade 4 injury approaches 1, and the probability of incurring a Grade 2 or less approaches zero as the duration increases (Figure 19).

Optic Nerve Head – Again only positive phase duration was identified as being significant. The measure of Lack of Fit has a large chi-squared value (3.183) and the whole model is nearly significant ($p=0.0744$). Simple ordinal logistic regression was then performed for this parameter with the Wald and Likelihood Ratio Tests returning p values of 0.0834, and 0.0744, respectively. The result suggests that positive phase duration is only weakly correlated with damage incidence in the optic nerve head. The p -values indicated that the intercept for the collapsed Grades 1 & 2 is significant, but Grade 0 is not. As the duration of the positive phase of the shock increases, the probability of incurring a “Grade 3 & 4” injury approaches “1” and the probability of incurring no injury approaches zero (Figure 20).

Choroid- Four blast parameters were identified as relevant, positive phase duration, positive impulse, negative phase duration, and pressure difference. The measured of lack of fit has a large chi-squared value (9.614) and the whole model is significant ($p=0.0475$). Simple ordinal logistic regression was then performed for these four parameters. The Wald Test results indicate that only the pressure difference is correlated with damage incidence ($p=.0449$), but the Likelihood Ratio Test indicates pressure difference, positive impulse, and negative duration as being significant

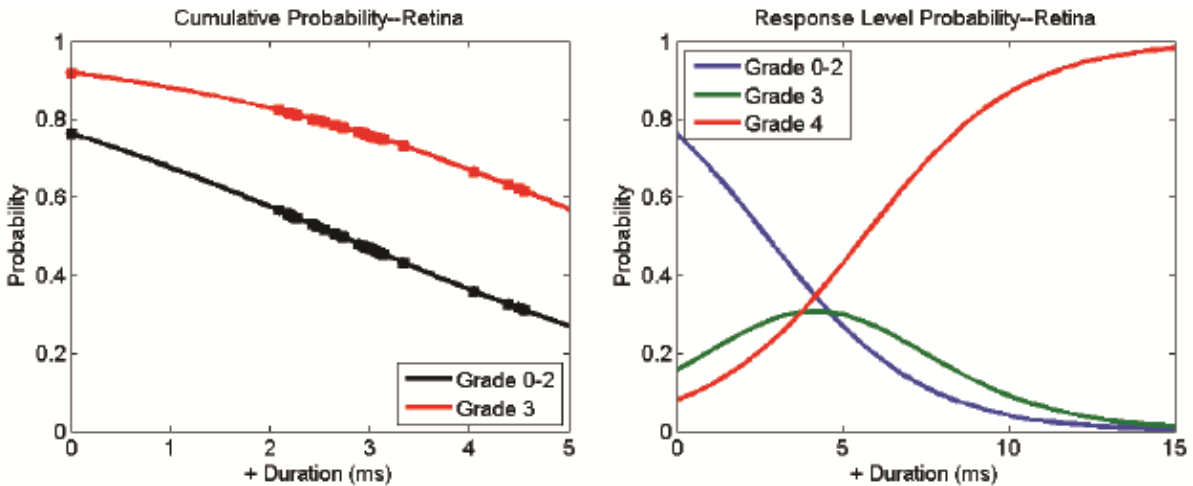


Figure 19. Cumulative probability and response level probability for the retina.

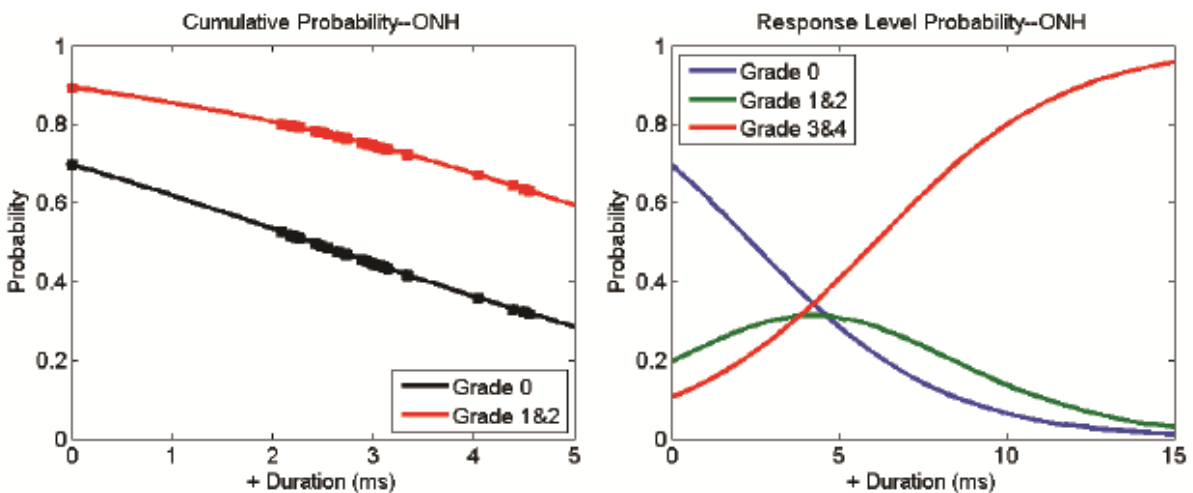


Figure 20. Cumulative probability and response level probability for the optic nerve head.

($p=0.0285$; $p=0.0371$; $p=0.0371$, respectively). The p -values for the cumulative grades 2 & 3 are significant, but not grades 0 and 1.

Angle – JMP Pro 10[®] identified mass of the eye, induced IOP, pre-IOP, and negative pulse duration as relevant, but additional analysis using SAS[®] revealed that the parallel odds assumption required for ordinal logistic regression was violated. Thus, multinomial logistic regression was applied, followed by simple ordinal logistic regression. The Likelihood Ratio Test returned the following p -values; negative pulse duration $p=0.1667$, pre-IOP $p=0.2542$, eye mass $p=0.0782$, and induced IOP $p=0.0299$. Thus, for the angle only induced IOP is significant.

Table 2. Grade Frequencies for both Blast-exposed and Control Porcine Eyes

Injury Category	Blast-exposed Eyes Grade Frequencies %					Control Eyes Grade Frequencies %				
	4	3	2	1	0	4	3	2	1	0
Choroid	14.3	31	28.6	11.9	14.3	7.7	15.4	23.1	15.4	38.5
Retina	23.8	28.6	16.7	14.3	16.7	7.7	15.4	23.1	7.7	46.2
Angle	40.5		45.2		16.2	23.1		38.5		38.5
Optic Nerve Head	23.8		30.9		48.6	15.4		15.4		69.2
Sclera	23.8		21.4		51.4	23.1		7.7		69.2

Note: It was necessary to collapse grades 3&4, and grades 1&2 for angle, optic nerve head, and retina because several frequencies were less than one.

Sclera - JMP Pro 10[®] identified mass of the eye, induced IOP, positive phase duration, and negative phase pressure as relevant, but again SAS[®] revealed that the parallel odds assumption was violated. Thus, multinomial logistic regression was applied, followed by simple ordinal logistic regression. The Likelihood Ratio Test revealed that only the mass of the eye is significant ($p=0.0275$)

Results of the statistical analysis support the conclusions of Sherwood et al. (2014) that primary blast overpressure can cause damage to *ex vivo* porcine eyes exposed 48 hours post mortem. The small p-values for the chi-square test indicate that the observed frequencies for blast-treated eyes are significantly different from control eyes not subjected to the blast environment (Table 2). The results further suggest that different ocular tissues and structures are sensitive to different aspects of the primary blast wave. For example, the choroid appears to be sensitive only to the pressure difference, positive impulse, and negative duration of the blast wave, whereas the retina and optic nerve head only show sensitivity to the positive phase duration. In contrast, the angle and sclera appear to be sensitive only to preparation parameters, i.e., the induced IOP and mass of the eye, respectively. In all cases, however, the individual tissue p-values were larger than the adjusted significance level of 0.0125. Thus one may conclude that the correlations at present are imprecise, and will require additional testing to obtain a large enough data set to clearly define the exact tissue response-blast wave relationships.

Nonetheless, all of the injury categories were associated with a blast parameter to some degree. The most significant was the positive phase of the blast in association with the retina. The predicted probabilities (Figure 19) show that the probability of observing Grade 4 damage reaches 100% at approximately 15 ms of blast duration.

Although not as significant, the positive impulse, positive duration, negative duration, and pressure difference of the primary blast were associated with the severity of injury for the choroid. The presence of minimum negative phase pressure and pressure difference is intriguing, because minimal pressure and overall pressure difference are generally discounted in the literature as a source of significant injury. Previously, only Duke-Elder (1954) speculated that the negative phase may be associated with ocular injuries.

2.6.4 Effect of Porcine Specimen Preparation

As data accumulated over the duration of the project, it has become increasingly evident that some factors other than blast were inducing injury artifacts, as evidenced by a number of false positive injuries in control eyes. For example, internal scleral delamination and mild angle recession was observed in approximately 20% of control eyes. It was hypothesized that such false positives may be due to several factors, namely (1) handling of the eyes during harvesting at the abattoir or during shipment, (2) preparation factors such as repeated saline injections as the eye is cyclically re-inflated prior to imaging, placement in gelatin (induced IOP), and blast testing (pre-IOP), (3) osmotic-induced damage due to exposing the eye to gelatin and refrigeration, and (4) natural decay of the eye due to biological processes post mortem. Our concern was that significant changes in the eye may occur due to any one of these factors.

As outlined above, the statistical results suggest that the angle and sclera are sensitive to preparation, namely induced IOP for the angle and mass of the eye for the sclera. However, these two parameters are not truly independent, as injection of HBSS to maintain proper IOP elevates the eye's mass. Because of periodic readjustment of the IOP, it is likely that incidental over-inflation contributed to some of the angle recession and scleral delamination damage observed (in the absence of blast exposure).

Adjustment of the IOP (induced IOP and pre-IOP) was often necessary because of its relatively quick decrease to a minimum value. Although the exact cause was unknown, we hypothesized that it was not a blast accelerated phenomena, but due to post-mortem elevated hydraulic conductivity, allowing rapid seepage of internal fluid through the scleral wall into the gelatin. To estimate the hydraulic conductivity K of the porcine eyes, the time (t) between pre- and post-blast IOP measurements was averaged for each test day and a MATLAB[®] script written to find the coefficients of a linear hydraulic conductivity model. The decay of pressure with time was taken as:

$$P(t) = P_0 e^{-(t/u)}$$

then a least squares approach used to estimate values for the parameters P_0 and u . The values of the measured IOP of both the control and blast-exposed eyes were compared using a two-sample, homoscedastic t-test assuming that the measurements were normally distributed and that the variances were equal.

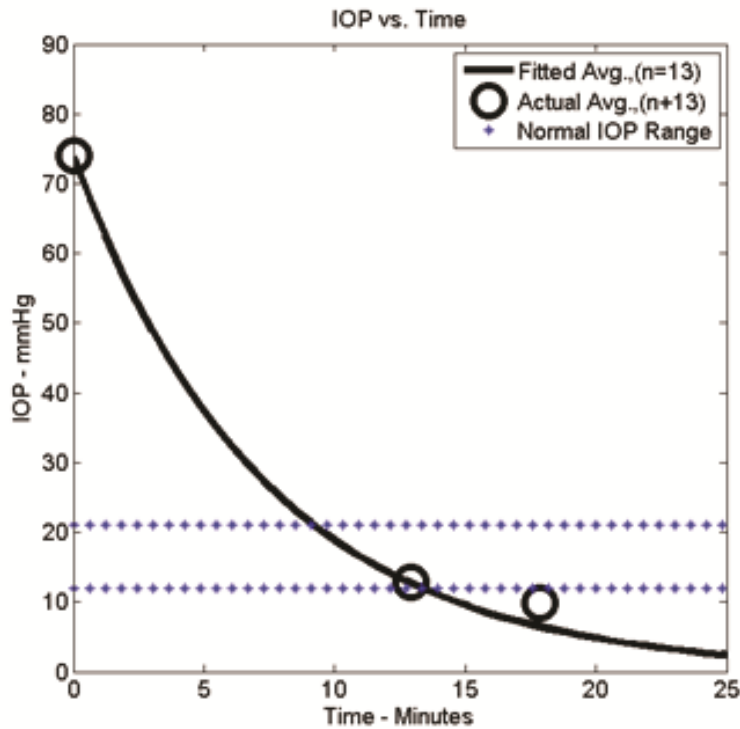


Figure 21. Plot showing IOP decline with time.

The times and the IOP were recorded for 11 eyes exposed to blast and 2 eyes not exposed to blast. The t-test indicated that the null-hypothesis could not be rejected, thus there was no difference between the decline in IOP over time between the blasted and non-blasted eyes for P_0 ($p=0.4248$) or u ($p=0.5909$). The fitted line of the average of all 13 runs (solid black line) and the average of the actual data values (solid black circles) is shown in Figure 21. The curve illustrates that in approximately 4 minutes the porcine eye lost 63% of its IOP, independent of blast exposure. This elevated hydraulic conductivity is probably indicative of the state of decay. Unfortunately for proper mechanical response, IOP levels must be maintained at a physiologically relevant state at time of blast exposure. We also found during preliminary testing that failing to re-inflate the eye prior to blasting resulted in much more extensive damage than that observed in eyes with physiological IOP values.

In a second control study, six enucleated porcine eyes were delivered, prepared, and pre-screened as normal, but not exposed to blast. Two eyes each were treated as follows:

1. Refrigerated in HBSS to detect natural degradation of the tissue with time and whether the handling of the eye while removing the muscles/eyelids might induce artifacts,

2. Mounted in gelatin as normal to determine whether any temperature/osmotic interactions between the gelatin and coats of the eye might be inducing artifacts, and
3. Injected several times with BSS to determine whether we were causing damage to the eye during the injection process.

After treatment, each eye was again subjected to B-scan ultrasound and UBM scans, and any change from its pre-treatment condition noted. Only exposure to gelatin (method 2) resulted in observed changes to the eye; primarily delamination-type injuries consistent with what might be observed due to thermal strain or osmotic shock. This suggests that exposure to gelatin might also contribute to scleral delamination injuries.

Unfortunately, due to limited funds, a study of the effect of age and post-mortem decay was not possible. The exact age of each eye was not available, but Animal Technologies typically harvests eyes from pigs whose ages vary from 6 months to two years. Eyes are enucleated and shipped overnight on wet ice. All blast testing and ultrasound screenings were completed with 48 hours of enucleation. Although our testing times were well within those quoted by previous researchers, it is hard to imagine that post-mortem decay was not a factor, as evidenced by the suggested elevated hydraulic conductivity. Even post-mortem decay in control eyes was problematic. Effects of decay could potentially be mitigated by fixatives, but we found that placing control eyes in formalin prior to the post-ultrasound examination introduced artifacts in nearly every control eye.

2.7 Porcine Trauma Data Analysis and Modeling

2.7.1 Univariate Logistic Regression

Although the development of predictive ocular trauma models will constitute the majority of our work in Year 3 of the project, preliminary work was undertaken this year in the development of trauma risk functions. Trauma risk functions estimate the probability of injury occurrence given some value of predictor variable, in this case the impulse of the positive blast phase. To determine the probability of achieving a damage level of 2 or higher on the Cumulative Injury Scale (CIS; Sherwood et al., 2014), a logistic regression was performed for each tissue using the experimental and pathology data shown in Appendix I. A binary data set was generated whereby a positive pathology observation (CIS score of 2 or higher) is taken to indicate a probability of 1 for the specific tissue and a negative pathology observation (CIS of 0 or 1) is taken to indicate a probability of 0 (Collett, 2003). The threshold of CIS score 2 or higher was selected on the basis that these injuries would require medical intervention while those below 2 would not.

A logistic transformation and regression was then performed and the resulting coefficients input to the general form of the logistic risk function (Proud et al., 2009):

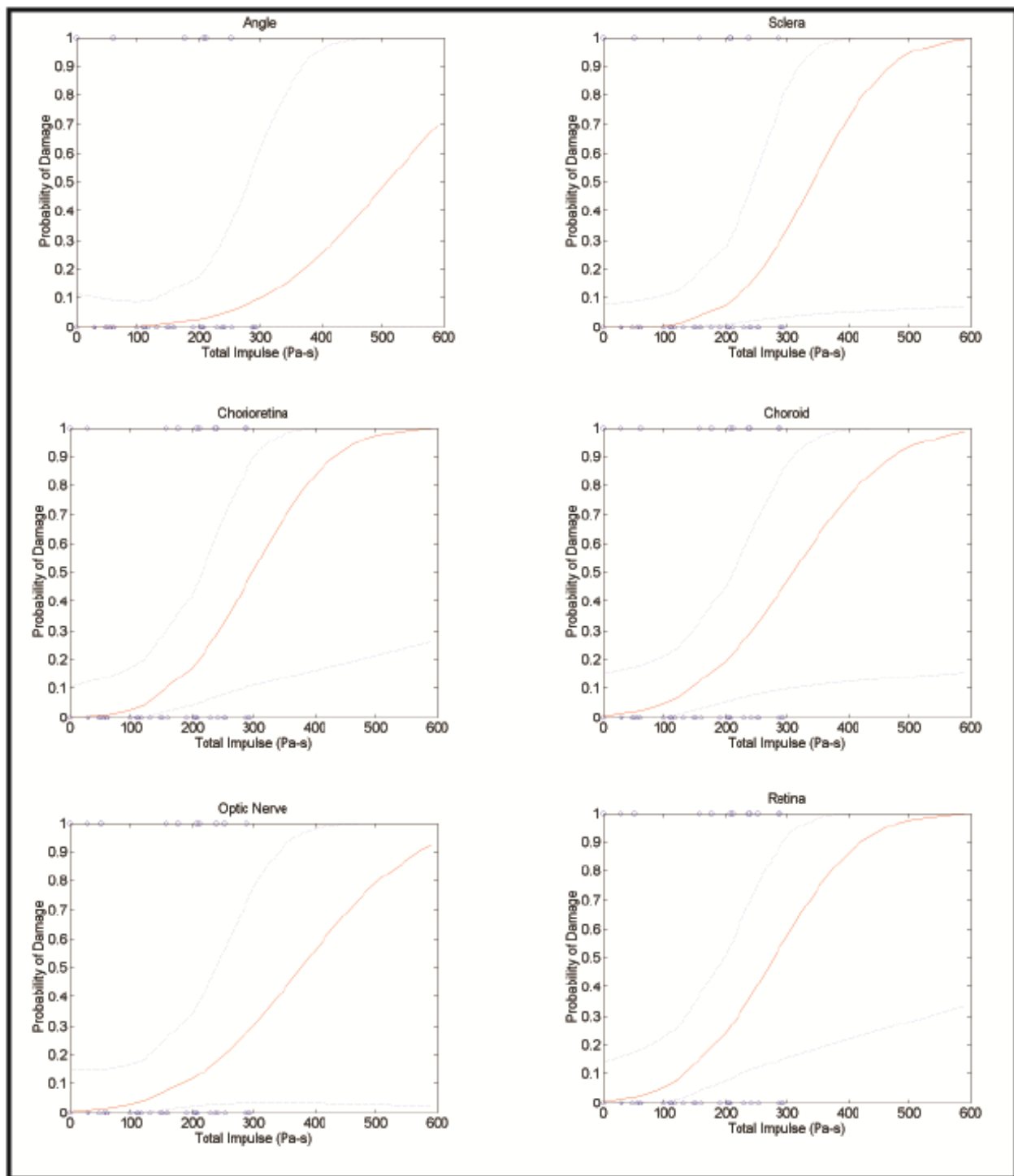


Figure 22. Preliminary ocular trauma risk functions vs. specific impulse. Trauma risk functions estimate the probability of injury occurrence given some value of predictor variable, in this case peak blast pressure. Retinal detachments were observed in 54% of control eyes and 83% of exposed eyes, suggesting that post mortem degradation and handling may render these eyes more susceptible to or even cause detachments. Still the mean CIS score for the retina was 1.3 for control eyes and 2.3 for exposed eyes ($p=0.034$) indicating that eyes exposed to primary blast had elevated likelihood and severity of retinal detachments relative to controls.

$$p = \frac{1}{1 + e^{-(ax+b)}}$$

where p is the probability of occurrence of the particular injury or trauma category, x is the blast impulse, and a and b are the regression parameters. Following this method, probabilities of occurrence were calculated for each of 12 ocular tissues considered in the study (Figure 22). Individual response was plotted versus peak pressure and observations (positive observations in x -direction at a probability of 1, and negative observations in x -direction at probability of 0) are indicated by open circles. Probability of injury data could also be plotted versus other blast wave parameters characterizing the positive and/or negative phases. In future efforts we will explore these variations and determine which provide the best fit to data.

As noted above corneal abrasion, angle recession, and retinal detachment were observed upon histopathological assessment in the vast majority of post-test specimens and a significant number of control specimens, suggesting that these may be artifacts of the handling or pathology procedures. Therefore, when possible, UBM was used to evaluate these injuries prior to introduction of fixative artifacts. The logistic regression accounts for such artifacts as an offset in the probability (i.e. the probability of incurring a retinal detachment is non-zero even in the absence of blast exposure). We are continuing to utilize statistical methods to ascertain whether these injuries may be induced by blast exposure, whether post mortem eyes are more susceptible to these injuries, and whether the characterization methods (specifically, fixation and histopathological analysis) contribute unduly to these artifacts.

Development of trauma risk functions has also been hampered by the generally infrequent tissue damage observed in the shock tube experiments. The maximum peak pressure achievable in the shock tube's current configuration is approximately 221 kPa (32 psi) and ~2 ms pulse width. At this shock condition, ocular tissue damage has been less frequent than anticipated. This may be due to the use of porcine, rather than human eyes, as porcine eyes are known to have a higher mechanical toughness than their human counterparts. Thus, uncertainty in the risk curves is due to several factors:

1. Potential presence of artifacts leading to false positives,
2. Non-zero incidence of tissue damage at null blast exposure (owing to #1), and
3. Non-unity incidence of tissue damage at the highest levels of blast exposure.

The ideal case for logistic regression is a dataset with a level of the independent variable at which all responses are negative and a higher level at which all responses are positive. Due to artifacts and the limited blast parameter space available during these experiments, neither of these conditions are met and we are left with quantifiable uncertainty in the predictions (indicated in the curves using 95% confidence intervals).

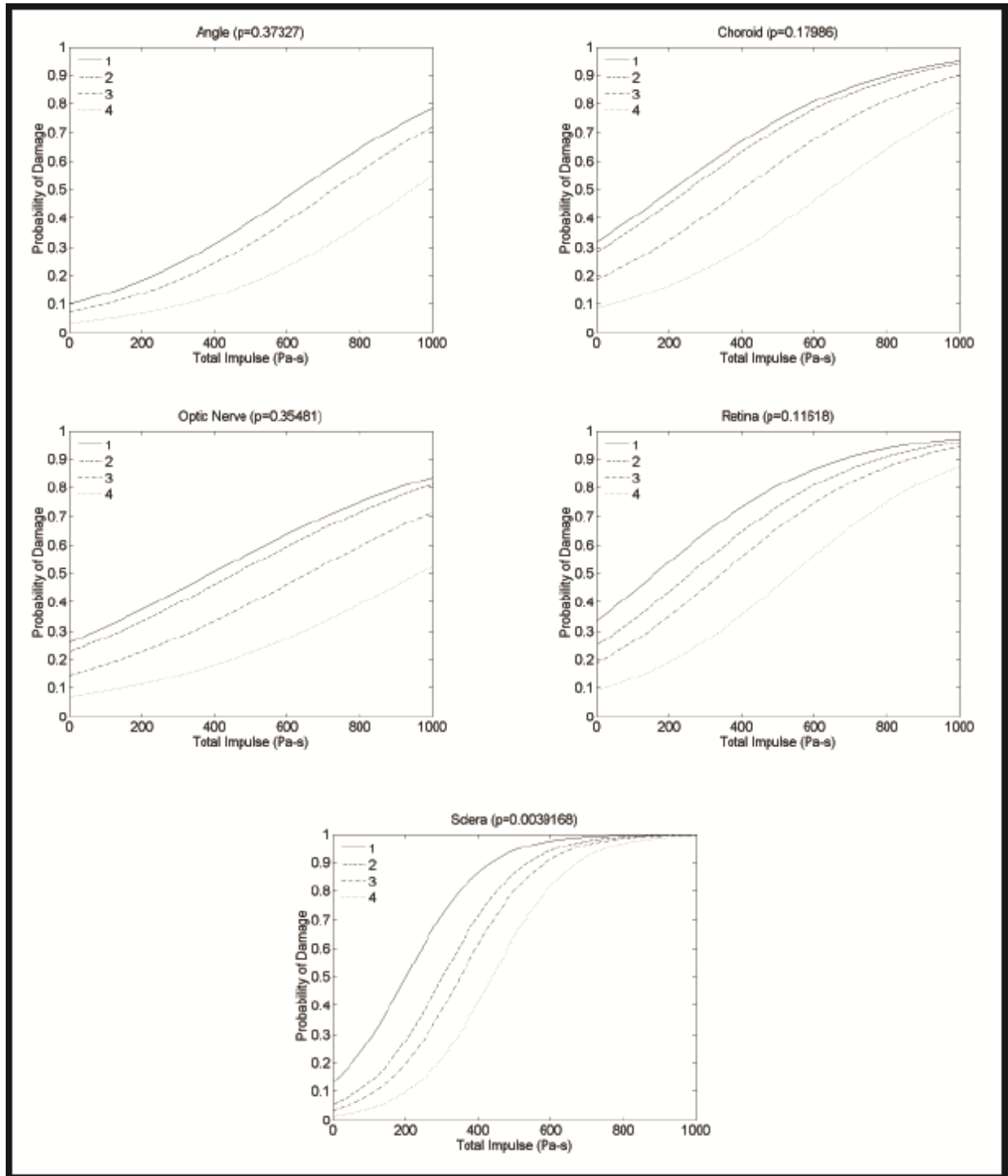


Figure 23. Injury risk probability as a function of injury severity or grade for the angle, choroid, optic nerve, retina and sclera categories.

2.7.2 Ordinal Multinomial Regression

In the previous section, we attempted to predict the probability of a given tissue requiring surgical intervention to reverse a primary blast-induced injury. Here, we undertake another preliminary analysis attempting to predict the likelihood of achieving a given CIS score in each tissue for a given blast using ordinal multinomial regression.

This statistical method allows the construction of a predictive injury model using the blast wave measurements and CIS scores for each tissue as inputs. Multiple blast wave characteristics may then be used to predict whether a given tissue will be damaged to the extent corresponding to a given CIS score rather than simply a binary response. The proportional odds model without interaction between blast parameters is given by:

$$\text{logit}[P(Y = j)] = \ln \left[\frac{P(Y \leq j)}{P(Y > j)} \right] = a_j + \sum_i b_i x_i,$$

where $P(Y > j)$ is the probability of achieving a CIS injury score Y greater than j ; a_j is the offset probability for CIS score j ; b_i is the slope corresponding to a unit change in the logit due to an increase in the blast parameter x_i . Both a_j and b_i are regression coefficients which determine the model's predictions. For example, the Bowen Curves are an example of multinomial regression with a binary response. In the case of the Bowen Curves, x_1 was the duration of the positive blast phase and x_2 was the peak overpressure. Thus far, we have performed ordinal multinomial regression using only a single predictive blast parameter (the impulse of the positive phase; Fig. 23).

2.8 *In Vivo* Rabbit Blast Experiments

The *in vivo* rabbit blast experiments were conducted in accordance with Animal Use Protocol A-14-007, approved by ISR IUCAC and the USAMRMC Animal Care and Use Review Office (ACURO). The objectives of this series of experiments were to (1) identify and characterize *in vivo* blast-induced trauma using a series of standard imaging techniques, and (2) to collect blood and aqueous samples for use in the biomarker study. Validation of the procedures was accomplished by SLOT team members and the ISR Staff Veterinarian by trial experiments on 3 Dutch-belted rabbits procured from RSI Robinson Services, Inc. (Mocksville, NC) for that purpose. During the trials minor modifications to the protocol were required (again approved by ISR IUCAC and ACURO) to facilitate ease and repeatability of sampling and post-test ophthalmic examination. The validated procedure consisted of the following essential elements (Table 3):

- Anesthesia- the Ketamine/Xylazine injectable anesthetic cocktail and buprenorphine, supplemented with Iso-fluorane gas, was used for restraint and pain relief for the subjects. Iso-fluorane will be used for short procedures,

Table 3. In-Vivo Rabbit Blast Test Procedural Sequence

Day	Procedural Sequence
1	<u>Baseline characterization</u> Anesthetize Analgesic Imaging: Direct ophthalmoscope, Slit Lamp, Fundus photography, OCT (retinal), HRT Corneal Conformal, Ultrasound (UBM, B-scan) Aqueous Draw Blood Draw Recovery
2	<u>Blast exposure</u> Anesthetize Analgesic Ear plug installation Place rabbit in holder IOP Blast exposure IOP Imaging: Direct ophthalmoscope, Slit Lamp, Fundus photography, OCT (retinal), HRT Corneal Conformal, Ultrasound (UBM, B-scan) Anesthetize with isoflurane if required Aqueous Draw Blood Draw Recovery
3	<u>24 hours post-blast exposure</u> Anesthetize Aqueous Draw Blood Draw Recovery
4	<u>48 hours post-blast exposure</u> Anesthetize Imaging: HRT Corneal Conformal, Other imaging as required Aqueous Draw Blood Draw Euthanize: Harvest eyes, optic nerve, and brain

- (specifically the 24 hour post-blast blood and aqueous draw) and a Ketamine/Xylazine cocktail (IM injection) used for longer procedures such as the blast exposure.
- Intraocular pressure (IOP) measurement – performed immediately before blast exposure (after rabbit placed in holder inside shock tube) and immediately after blast exposure. In each case IOP was measured using icare® TONOLAB and TONOVET devices (Icare Finland Oy, Helsinki, Finland).

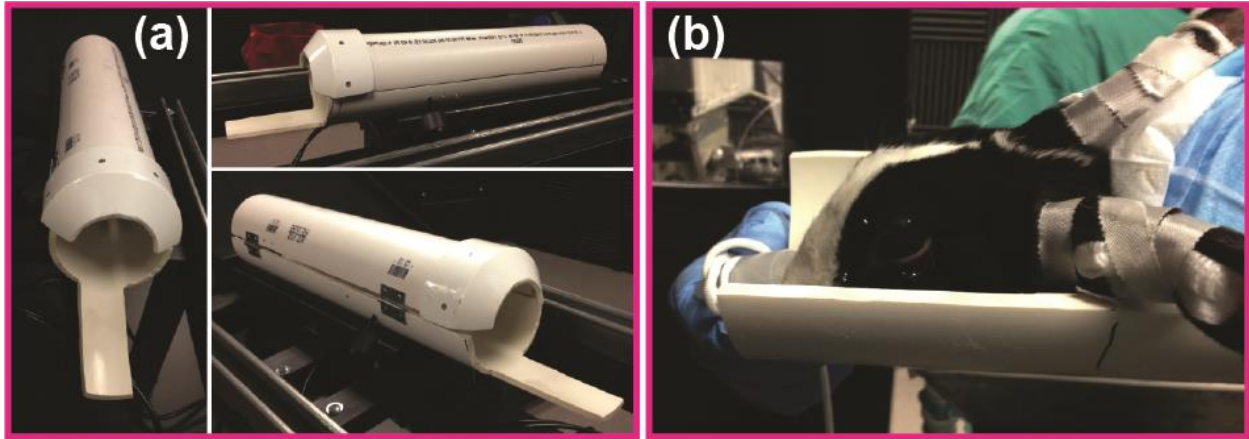


Figure 24. (a) Three views of the custom PVC holder. The holder provides body protection (exposing only the face and eyes) during blast exposure. (b) Ear protection consisting of standard earplugs taped into place with 4x4 gauze.

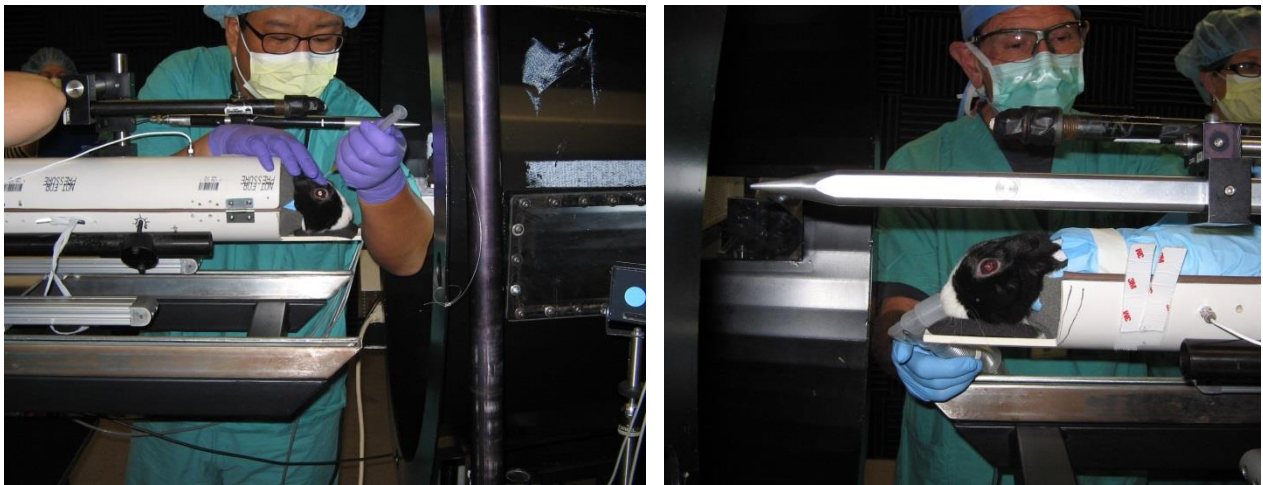


Figure 25. Two views of the Dutch-Belted rabbit secured inside the custom PVC holder. The head of each rabbit faced the open end of the shock tube and extended beyond the holder. The PVC holder firmly held the body of the rabbit in place during the blast.

- Imaging- performed 1 day before blast exposure and then immediately after blast exposure. Imaging consisted of Direct Ophthalmoscopy, Slit Lamp and Fundus photos, OCT, HRT corneal confocal imaging (producing images from which cell counts can be obtained in the corneal endothelium), and Ultrasound (UBM and B-scan).
- Blood and aqueous collection – performed 1 day before blast exposure, and at intervals of 4, 24, and 48 hours after blast exposure. Blood was taken from the central ear artery with a 23 gage butterfly needle and a 3cc syringe. Aqueous humor was collected using gentle aspiration with a syringe and plunger.

Table 4. Summary of *In Vivo* Rabbit Blast Experiments

Test No.	Peak Pressure (kPa)	Pulse Duration (ms)	Specific Impulse (Pa-s)
1	53.8	2.70	59.3
2	54.0	2.69	58.6
3	52.9	2.73	58.2
4	52.6	2.71	58.4
5	52.7	2.69	57.2
6	54.4	2.75	60.6
7	91.1	2.80	102.7
8	87.3	2.83	106.6
9	80.9	2.87	98.6
10	81.8	2.88	99.2
11	84.2	2.76	100.1
12	123.7	2.99	160.0
13	135.7	3.18	160.4

- Euthanasia and tissue harvest- To increase research program impact, collaboration, and efficiency, it was further decided to share harvested tissues between the SLOT program and researchers at ISR interested in traumatic brain injury (TBI). Thus samples of the eyes, optic nerves, and brains were sent to SLOT team member Dr. Randolph Glickman for identification and characterization of the biomarker proteins, and to Dr. Huey-Ching Wang at ISR for TBI research.

Following procedure validation, *in vivo* blast tests were completed on 13 Dutch-belted rabbits (also procured from RSI Robinson Services, Inc.). Each rabbit was secured at the open end of the ISR shock tube using a custom holder fabricated from two halves of hinged PVC pipe (Figure 24). Ear protection consisting of standard earplugs was taped into place with 4x4 gauze pads (Figure 24). During anesthesia trials it was observed that the eye lids remain open, thus there was no need for tape or sutures to hold the lids open during blast testing. The rabbit was then placed inside the holder with its head oriented toward the shock tube and extending beyond the end of the holder (Figure 25). The pipe halves were then closed and latched to firmly secure the body of the rabbit inside the holder. The rabbits were subjected to low level blast exposures ranging from 54 kPa to 135 kPa with durations varying from 2.7 ms to 3.2 ms

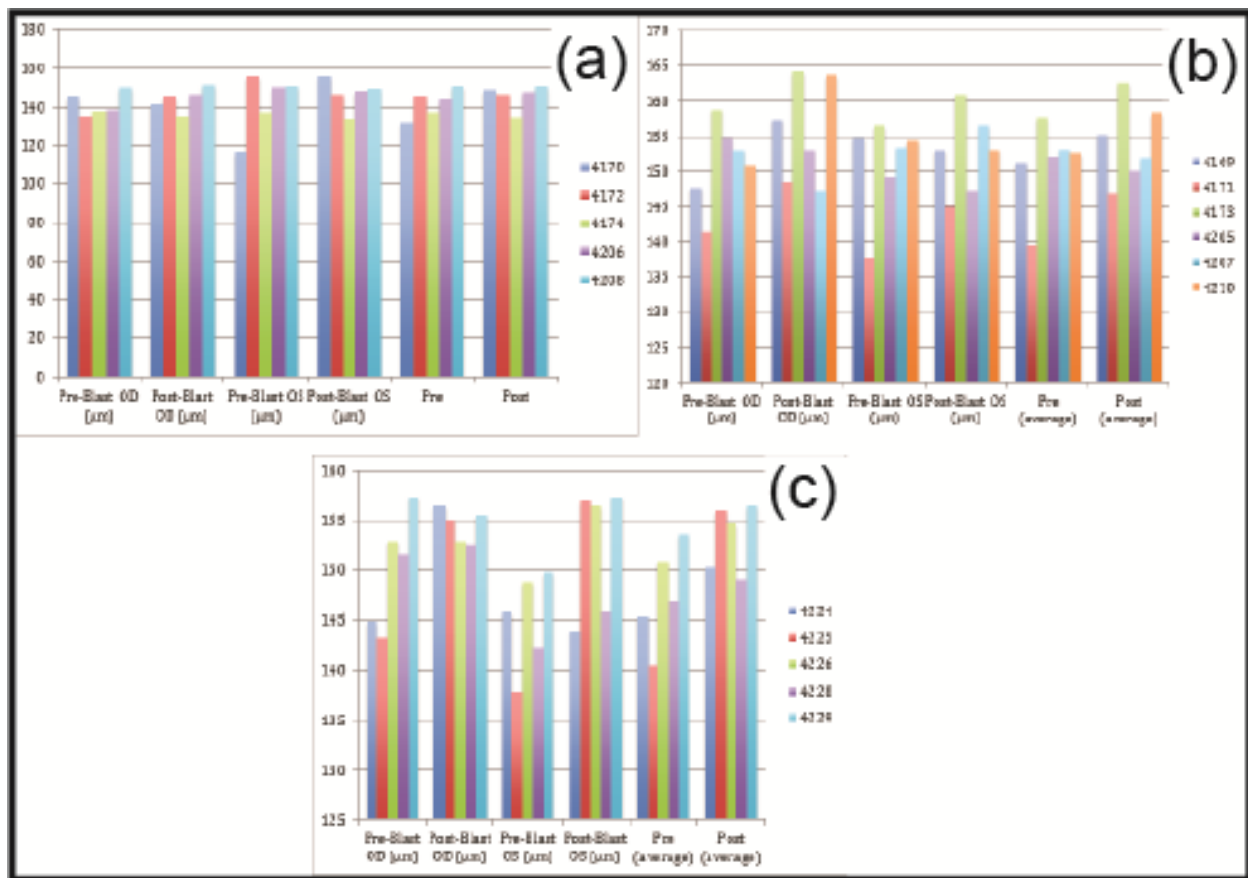


Figure 26. Preliminary results of OCT measured retinal thickness (μm) after blast exposures of (a) 0 kPa (pre-blast), (b) 54 kPa, and (c) 85 kPa.

(Table 4). At intervals of 4 hours, 24 hours, and 48 hours, samples of aqueous fluid and blood were extracted for the biomarker study. After the 48 hour blood draw, each rabbit was euthanized followed by extraction of the eyes, optic nerves, and brain. Five control rabbits were subjected to the exact same procedures, except that they were not exposed to an actual blast.

An extensive imaging series was conducted on each rabbit before and after blast exposure to identify and characterize any blast-induced ocular trauma. The imaging included (1) Direct Ophthalmoscope, (2) Slit Lamp, (3) Fundus photography, (4) OCT (retinal), (5) HRT Corneal Conformal, and (7) Ultrasound (UBM, B-scan). All imaging analysis was performed on both OD & OS eyes. Slit lamp images were used to observe any surface corneal damage as well as sphincter ruptures that could be present post-blast. Fundus photos were observed for hemorrhaging and/or edema. Optical coherence tomography (OCT) images measured the retinal nerve fiber layer (NFL) thickness using five images pre-blast and five images post-blast and taking one measurement from each image within 5 mm of the optic cup from the ganglion cell layer to the outer nuclear layer (photoreceptors). This measurement was made at a point in each image where the two layers were tangential to the horizontal OCT axis by

measuring the length of a vertical (axial) line to ensure maximum spatial resolution. Corneal confocal microscopy images measured the focus, which estimates corneal thickness as well as the density of the endothelial cells. An area of approximately 0.03 mm² was obtained and each cell in the specified area was counted and then an estimate of the endothelial cells in the total area was estimated. Ultrasound biomicroscopy (UBM) was used to measure the anterior chamber angle pre- and post-blast. Lastly, B-scan ultrasound was used to detect retinal detachment.

Statistical Analysis was performed on the OCT retinal thickness data using JMP Pro 10[®] and a mixed model repeated measures ANOVA to take advantage of the repeated measures across both pre- and post-blast data for both the left and right eye on each rabbit. Blast intensity as well as pre- vs. post-blast conditions were considered as treatment effects in the model. A Tukey adjustment for multiple test comparisons was used to compare the treatment groups. Statistical significance was established if the p-value was below 0.05.

The repeated measures ANOVA results reveal an overall increase in the nerve fiber layer (um) after blast (p-value = 0.008). The control group was slightly lower than the 54 kPa (8 psi) group (Tukey adjusted p-value = 0.026), however no interaction effect was observed between time and treatment groups.

An interesting finding from our preliminary analysis is that corneal thickness appears to increase over time with no statistically significant difference between the blast pressures (Figure 26). The pre-blast thickness was significantly lower than both the post (Tukey adjusted p-value=0.003) and 48-hour post blast (Tukey adjusted p-value <0.0001). Endothelial cell density shows some extreme differences between the blast forces, even pre-blast with 0 (control) and 54 kPa having significantly lower density than 85 and 135 kPa. The change in density over time however, is relatively minor. Each blast has no significant change in density over time when comparing pre-blast vs. post-blast and pre-blast vs. 48 hour post-blast. The fact that the densities are different upon initial observation on casts doubt on whether this is a useful metric for quantifying or diagnosing blast injury.

Some retinal edema was observed in fundus images but must be confirmed with OCT measurements. B-scan images have all appeared normal with no indication of retinal detachment. UBM data has not yet been analyzed. No iris sphincter ruptures have been observed in slit lamp images. We are currently exploring the possibility of dust and dirt embedded into the cornea as a result of the blast. This would constitute a secondary blast effect with important clinical implications.

2.9 Biomarker Study

2.9.1 Biomarkers in Aqueous Humor and Blood Serum

In order to evaluate the release of trauma-related biomarkers into the injured eye, as well as into the circulatory system, samples of aqueous humor and blood from control and shock-tube exposed rabbits are being probed using multiplexed, magnetic-bead based Luminex xMAP assays. Using magnetic beads individually targeted to specific analytes and assessing the binding of the beads to their targets using technology similar to that used in flow cytometers, multiple analytes can be measured in each sample. The magnetic beads are more easily manipulated during sample washing and transfer procedures.

One technical challenge being addressed currently is that most of the commercial xMAP kits use antibodies prepared against human or rodent species; relatively few are prepared against rabbit targets. Fortunately, many of these detection antibodies show sufficient cross-species reactivity to allow reagent use with rabbit samples. Currently, we are determining cross-reactivity in several commercial xMAP kits for the analytes of interest; once this is determined, the analysis of the aqueous and blood samples taken from the rabbits in the shock tube experiments will be carried out.

Three xMAP test kits are being evaluated for cross-reactivity. Two human and one rat “Milliplex” evaluation kits were obtained from EMD Millipore at no charge for testing cross-reactivity. The assays are being carried out in the Center for Advanced Translational Technologies (the CATT Core), located at the University of Texas Health Science Center, directed by Dr. Doug Williamson. The panels being tested are the following:

1. *Human Neurological Disorders Magnetic Bead Panel, Milliplex*

Analytes:

- Total tau
- Tau (Thr231) phosphorylated neurofibrillary tangle protein
- α -Synuclein
- NGF- β (nerve growth factor)
- NSE (neuron specific enolase)
- PARK5/UCHL1 (Parkinson Disease Protein 5)
- PARK7/DJ-1 (Parkinson Disease Protein 7)

2. *Human TH17 Magnetic Bead Panel, Milliplex*

Analytes:

- TNF β , GM-CSF, IFN- γ , IL-1 β , IL-2, IL-4, IL-5, IL-6, IL-9, IL-10, IL-12 (p70), IL-13, IL-15, IL-17A, IL-17F, IL-17E/IL-25, IL-21, IL-22, IL-23, IL-27, IL-28A, IL-31, IL-33, MIP-3 α /CCL20, TNF- α
- (This panel probes for cytokines involved in adaptive immunity, which are activated in response to a range of inflammatory, degenerative, and

trauma-related conditions. The antibodies are nominally reactive to human antigens.)

3. *Rat Cytokine/Chemokine Magnetic Bead Panel, Milliplex*

Analytes:

VEGF, EGF, Eotaxin, Fractalkine, G-CSF, GM-CSF, GRO/KC, IFN- γ , IL-1 α , IL-1 β , IL-2, IL-4, IL-5, IL-6, IL-10, IL-12 (p70), IL-13, IL-17A, IL-18, IP-10, Leptin, LIX, MCP-1, MIP-1 α , MIP-2, RANTES, TNF- α

(This broad panel probes for cytokine and immune system modulators involved in systemic responses to inflammation, cancer, trauma, and cancer. The antibodies are nominally reactive to rat antigens).

2.9.2 Tissue Biomarkers of Trauma

In order to complement the fluid-borne biomarkers, a different analytical technique is being used to detect tissue-based biomarkers. This is being accomplished using Matrix Assisted Laser Desorption Ionization (MALDI) imaging, a mass spectrometric based method that not only enables identification of specific proteins in tissue, but also the spatial location of those biomarkers *in situ*. A section of the tissue of interest is prepared for the laser assisted matrix desorption process, and then the activating laser is stepped across the tissue in a raster pattern. The intensity of the ejected ions (specifically, the relative abundance of the protein ions) is plotted as a function of the position of the laser beam on the tissue. The map of ion location produces an “image”, thus mapping the location of the protein being analyzed. This approach is being used to analyze biomarkers in the retina and optic nerves traumatized eyes. This work is a collaboration with Dr. Stephan Bach and his lab group in the Department of Chemistry at the University of Texas at San Antonio.

To prepare tissue for the MALDI technique, sections were cut from whole eyes from animals subjected to several ocular trauma models. Control and traumatized whole eyes were excised from the anesthetized animals, just before euthanasia, and then immediately frozen. The frozen tissue block was mounted with TFM (a cryo mounting medium) on the cutting plate of a cryostat. With the cryostat working temperature set to -24 to -27° C, 10 to 12- μ m thick frozen sections were cut from the eye with the blade set at a 6° cutting angle. Ribbons of three to four sections were mounted on indium titanium oxide (ITO)-coated slides used for MALDI analysis following the procedure described by Grey et al. (2009). Briefly, the sections were floated on to the ITO slides from a methanol layer, and attached well to the slides after evaporation of the methanol. The slides were stored at -75 °C until MALDI imaging analysis was carried out.

The matrix used for MALDI consists of an organic compound that facilitates the transfer of laser energy into the tissue and the ejection of protein or peptide fragments from the tissue and into the mass detector. Selecting the optimal matrix compound is an empirical process, beyond the general considerations of using a hydrophilic matrix compound for hydrophilic samples, and hydrophobic compounds for hydrophobic



Figure 27. Post-wash images (prior to matrix sublimation/recrystallization) of the sections analyzed by MALDI imaging. Left-hand panel: section from a control eye. Right-hand panel: section from a traumatized eye.

compounds. Several compounds were screened in preparation for the ocular trauma study. To date, we have obtained the best results with 2,5-dihydroxybenzoic acid (DHBA). Using a protocol described by Yang & Caprioli (2011) the sections were washed with a series of ethanol and ethanol-chloroform-acetic acid solutions, then coated with DHBA by sublimation followed by recrystallization. MALDI was carried out over a raster width of 100 μm using 500 laser shots per spot, and the laser intensity set to 25%. Protein signatures were collected over a range of 10,000 to 30,000 m/z (mass to charge ratio) using a Bruker Daltonics Ultraflextreme MALDI/TOF. The instrument software supplied by Bruker was used for the proteomic identification, as well as to create the graphic representation of the protein ion abundance and location in the tissue specimens.

2.9.3 Characterization of Trauma-related Proteins in a Model of Optic Nerve Trauma.

Protein spectra were obtained from sections cut from control and traumatized eyes. In order to develop and validate the MALDI imaging technique, tissue from rat eyes subjected to torsional trauma was used for this phase of the work, as the tissue from the *in vivo* rabbit experiments was not yet available for these experiments. We anticipate that the methods illustrated here will be directly applicable to the rabbit material. In the following figures, the relative abundance of specific size classes, i.e. m/z ratios, are represented as pseudocolor maps overlaying the image of the actual tissue section. Below the pseudocolor abundance map, the graph of the specific protein families found in the tissue is shown in a line graph. The graphs obtained from the control eyes and the trauma eyes can be compared directly to determine differences in protein expression. The appearance of the tissue sections, immediately following the washes in the organic solvent series as shown above (Figure 27): the control eye is shown in the left in Figure 27, and the image of the traumatized eye is in the right panel of Figure 27. A representative average protein mass spectrum obtained from a control eye is

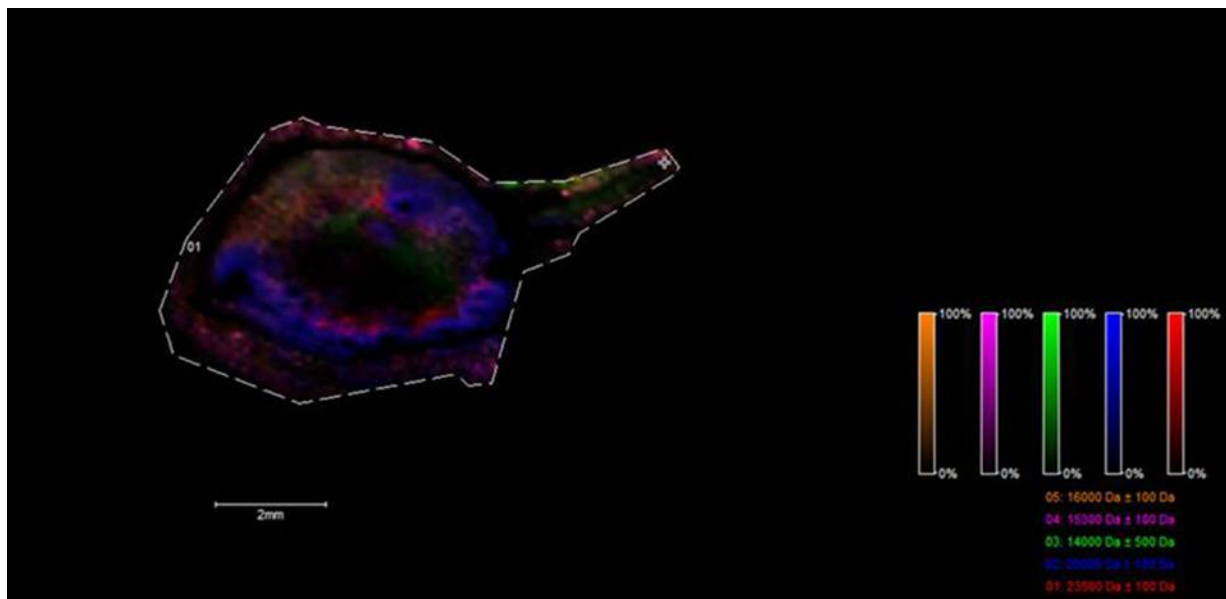


Figure 28. A pseudocolor image of a section from a control eye showing the spatial distribution of proteins. The outline of the section shown in the left-hand panel in Figure 1 has been traced over the pseudocolor maps of the protein size distributions in the tissue section. Each color indicates a separate m/z range, as indicated in the legend at the right-hand side of the figure.

shown in Figures 28 and 29, while an average spectrum obtained from an eye subjected to torsional injury is shown in in Figures 30 and 31.

While differences in the protein expression can be observed in the averaged spectra shown in Figures 28-31, e.g. in the m/z range from 14,000 to 16,000, the differences in specific locations can be much more pronounced. Querying the protein spectra in particular locations can be accomplished in the instrument software, as shown in Figures 32 and 33, in which the protein spectra from corresponding locations in the optic nerve of the control and traumatized eyes are pulled out of the averaged MALDI dataset. A pronounced difference in the distribution of proteins between the control and traumatized eyes was found at this location in the optic nerve, where the injury was expected to be most severe. The traumatized eye expresses protein(s) in the 15 to 16 kDa range in the optic nerve, while the control eye expresses protein(s) in the 14 KDa range in the same location of the optic nerve. This difference has now been observed in several samples from animals in this series, which supports the conclusion that trauma-related protein biomarkers are being expressed in this size range. Current work is being directed at identifying the specific proteins shown in these spectra, and the applying these methods to the eyes from the rabbits from the shock tube experiments. The identification of the proteins will help to elaborate the nature of the molecular response of the eye to blast injury. These results in general support the use of MALDI imaging for discovery of trauma-related biomarkers.

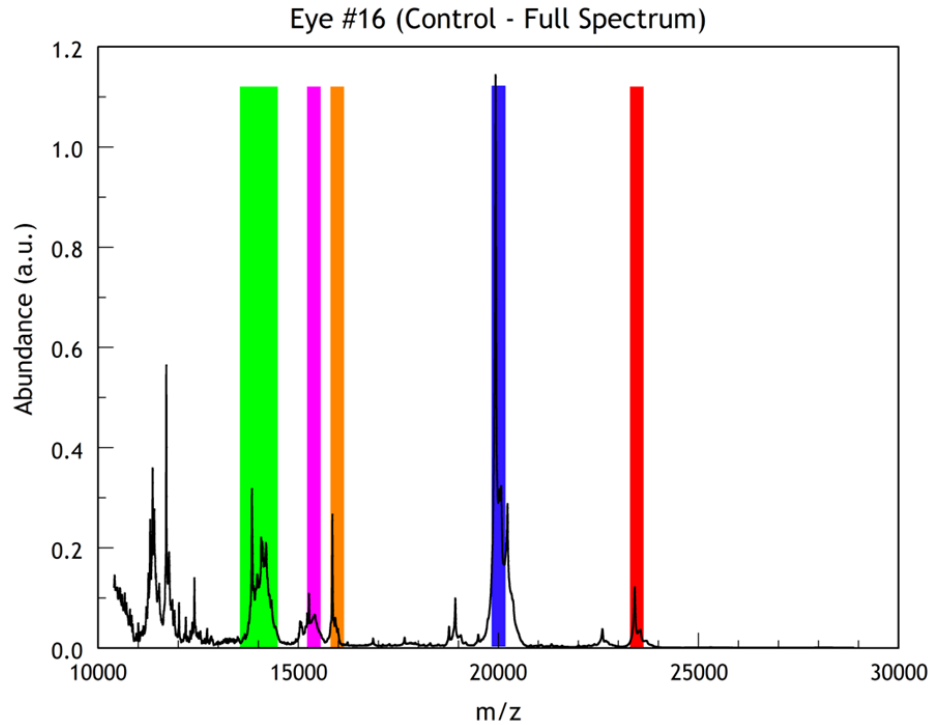


Figure 29. The average protein mass spectrum (abundance vs m/z). The color boxes indicate the m/z values of the proteins in the corresponding color-coded areas of Figure 28. Mass scan range was 10,000 to 30,000 amu.

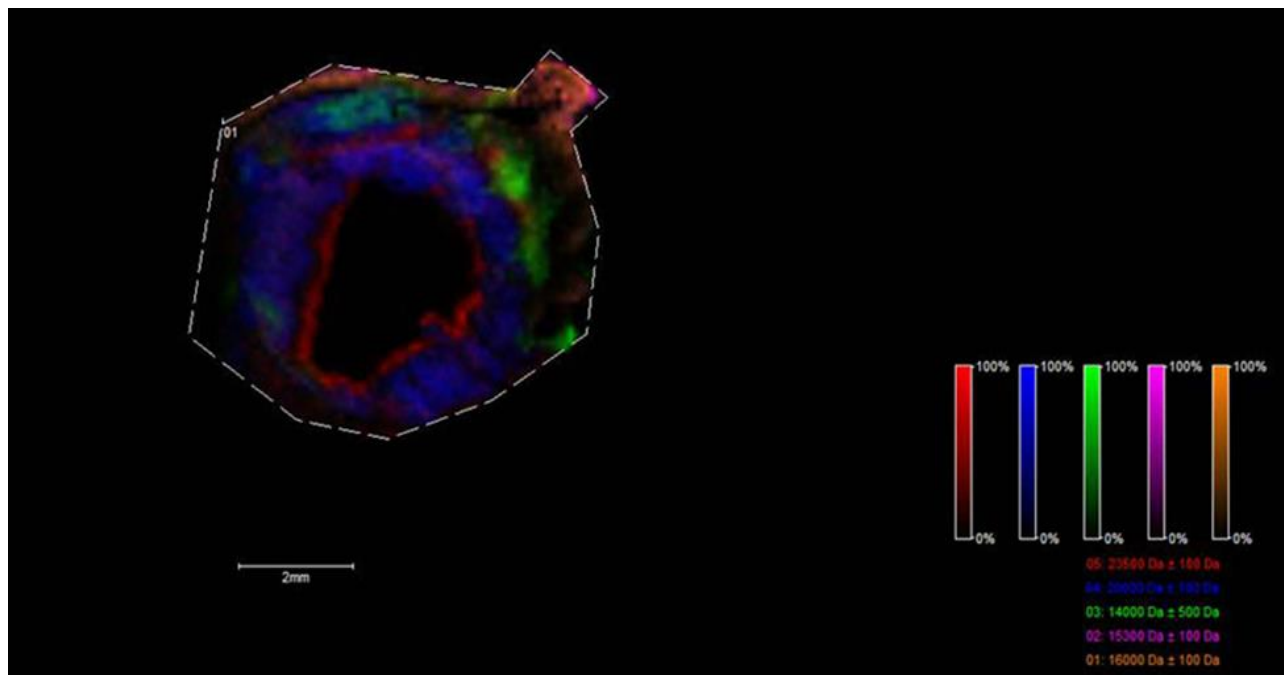


Figure 30. MALDI analysis of an eye subjected to torsional optic nerve trauma. The outline of the section shown in the right-hand panel of Figure 27 has been traced around the pseudocolor map of the protein size distributions in the tissue. Data format as in Figure 28.

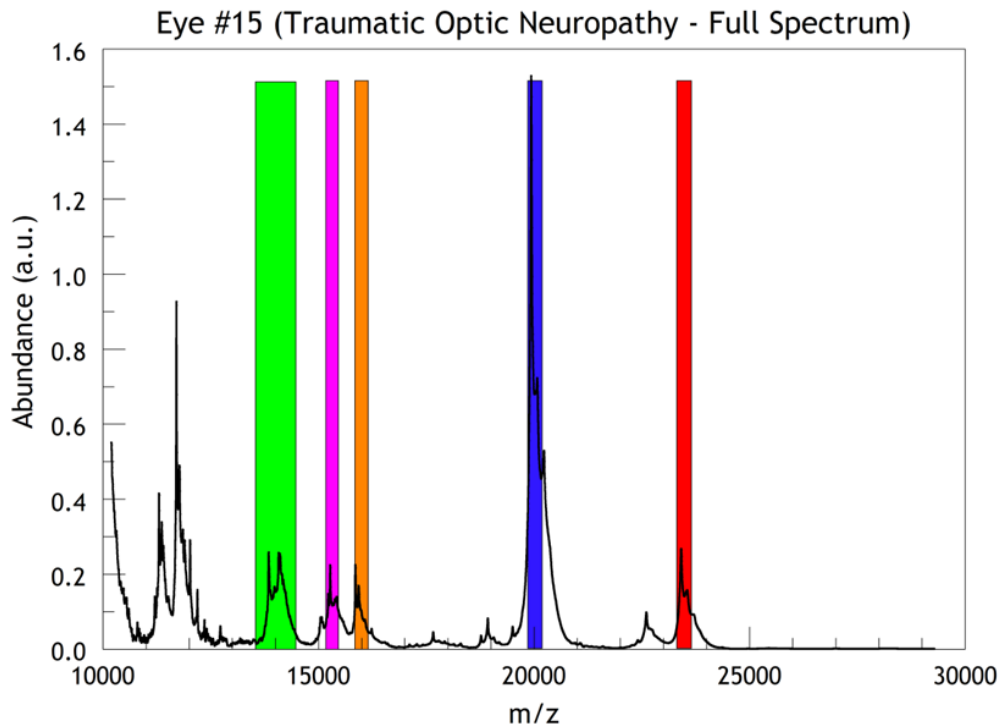


Figure 31. Average protein spectrum obtained from the tissue section shown in Figure 30. Color boxes indicate m/z ratios of corresponding protein spatial distributions in Figure 30.

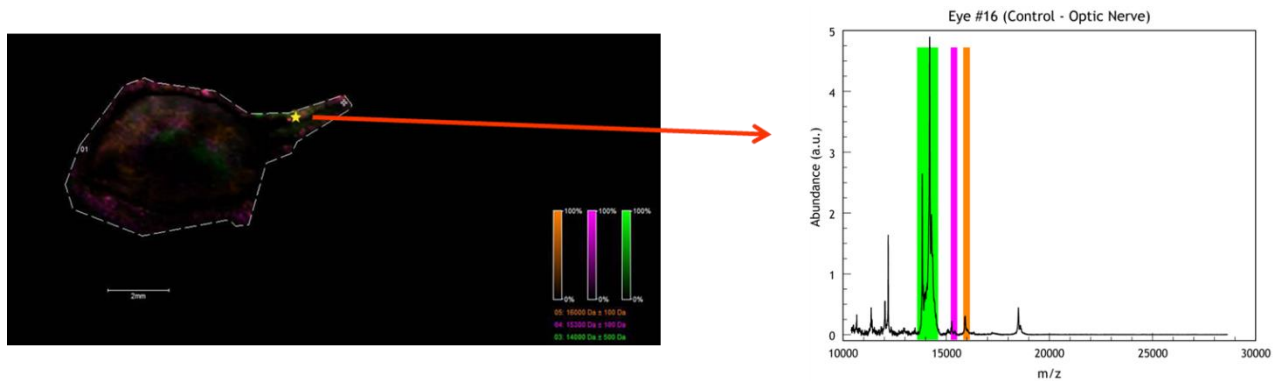


Figure 32. MALDI imaging analysis of the location indicated by the gold star in the optic nerve of a control eye. Left panel: the distribution of the indicated protein sizes over the outline of the tissue section. Right panel: Mass spectrum of the proteins expressed at the study location. Note the high abundance of proteins of 14,000 m/z (green box) and low abundance of proteins at 15,000 m/z (pink box) and 16,000 m/z (brown box).

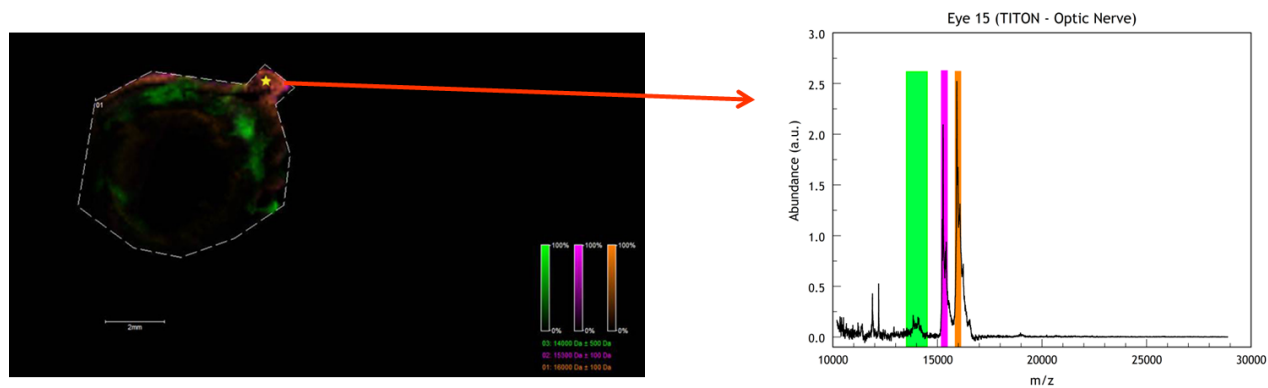


Figure 33. MALDI imaging analysis of the location indicated by the gold star in the optic nerve of a traumatized eye. Data format as in Figure 4. Note the relatively high abundance of the proteins at m/z 15,000-16,000 (pink and brown boxes, respectively), while the abundance of proteins at 14,000 m/z (green box) is much lower than in the control eye.

2.10 Numerical Models & Simulations

Two computational software packages have been utilized to date to simulate the response of eyes to blast, LS-DYNA and CTH. CTH is a three-dimensional Eulerian wave propagation code (hydrocode) developed and distributed by Sandia National Laboratories. It has a second order material advection algorithm and an advanced high-resolution interface tracker making it ideally suited for problems involving large distortions caused by blast or impact. In the Eulerian formulation the computational grid is fixed and materials are allowed to flow through the grid. After each time step, the materials and interfaces are re-projected back into the Eulerian grid avoiding many severe distortion problems commonly encountered in finite element codes such as LS-DYNA.

LS-DYNA is a commercially available Lagrangian finite element program distributed by Livermore Software Technology Corporation (LSTC) of Livermore, California. It is generally considered the industry standard for simulation of vehicle crash and associated biomechanics. In the Lagrangian formulation, the computational grid remains fixed to the materials as they undergo distortion. Thus, large distortions often result in instabilities and early termination of the calculation. In LS-DYNA, the problem is partially solved by incorporation of Eulerian fluid dynamics components. We are using CTH to study the short-term effects of wave and shock propagation through the eye, and LS-DYNA to study the longer term effects of acceleration and applied forces on the ocular tissues.

Two types of CTH computations have been undertaken to date, (1) simulations of the shock tube, and (2) simulations of the shock tube and eye. One disadvantage of CTH is that the blast wave must be generated within CTH from an initial static pressure. Thus to achieve the correct blast wave exposure, the entire shock tube must be modeled. In LS-DYNA however, the blast wave can be input as an initial loading condition (For our simulations we can directly input the Friedlander wave forms

Table 5. Dimensions and Sources for Porcine Eye Model

Geometry	Dimensional Value	Source
Scleral outer radius	11.12 mm (calculated to match area value)	Olsen 2002
Scleral inner radii	various	Olsen 2002
Corneal outer radius	9.01 mm	Reilly 2009
Corneal thickness	0.98 mm (at apex)	Reilly 2009
Lens anterior radius	6.63 mm	Reilly 2009
Lens posterior radius	5.08 mm	Reilly 2009
Lens position	2.5 mm posterior to posterior surface of cornea	Reilly 2009
Zonules	Simplified for simulation purposes.	Burd 2002, Bron et al 1997
Ciliary body	Simplified for simulation purposes.	Asejczyk-Widlicka 2008
Iris root thickness	n/a	Bron et al 1997
Iris collarette thickness	n/a	Bron et al 1997
Pupil diameter	n/a	Bron et al 1997
Chorioretina thickness	0.2 - 0.86 mm	Bron et al 1997, Sanchez 2011

measured in the shock tube experiments.), so only the eye need be modeled. In addition, CTH requires at least 4 elements across the 1 mm thick sclera. Thus, high fidelity CTH modeling of the shock tube and eye requires models with in excess of 1 million computational elements, and very long run times (currently on the order of 1 week of actual time). In LS-DYNA, a fewer number of solid elements are required to define the tissue thickness, thus size and computational times are greatly reduced.

2.10.1 LS-DYNA Model of the Porcine Eye

A validated computational finite element analysis (FEA) model of the porcine eye was developed to provide insight as to the physical trauma mechanisms observed in blast experiments conducted during this program, as well as blunt impact experiments conducted in previous research efforts. The porcine eye is considered a good surrogate for the human eye and used extensively in experiments, but to our knowledge this is the first computer model of the porcine eye. Geometry for the FEA model was created in 3D using the SolidWorks CAD software (Dassault Systèmes SOLIDWORKS Corp., Waltham, MA). Dimensional data for the model came from a variety of sources (Table 5). Because of its rotational symmetry, the eye was modeled in quarter symmetry. The sclera was modeled with continuously variable thickness ranging from 0.43 mm to 0.89 mm. The overall diameter of the globe in the coronal plane was 22.2 mm. The length of the eye in the transverse/sagittal planes was 22.9 mm. Dimensions of the cornea and lens and their positional relationship were taken from a study that determined optically

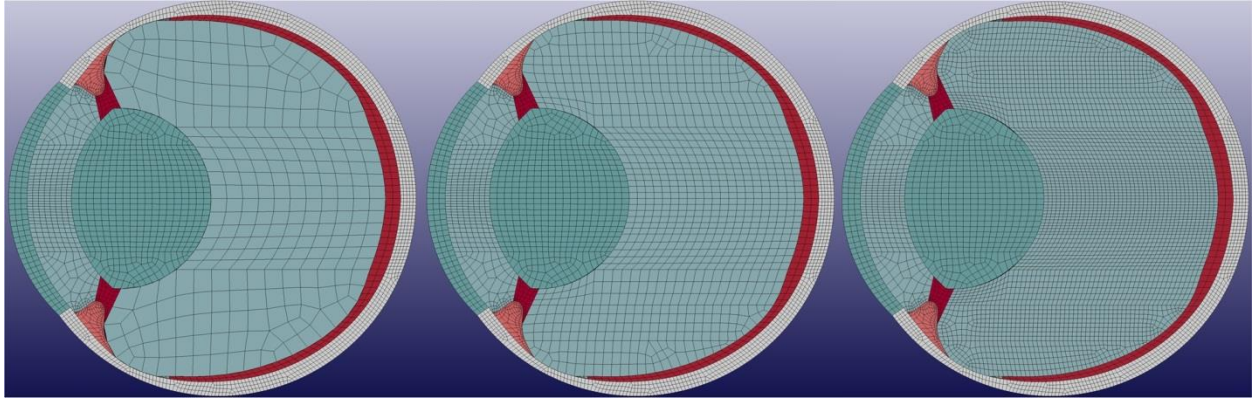


Figure 34. Eye model showing included components and 1 mm, 0.5 mm, and 0.25 mm mesh

correct geometry (Reilly et al, 2009). The zonules were simplified for computational purposes into a continuous band of material connecting the lens equator to the ciliary body. The ciliary body was also simplified, combining all the ciliary muscles and connective tissues into one contiguous material. The geometry of these constructs was based on imagery from various sources in the literature (Bron et al., 1997; Sanchez et al., 2011). The iris was not modeled as its relatively thin section would have required the use of many extremely small elements. No damage to the iris was observed in physical experiments and so it was postulated that the contribution of the iris to the overall dynamics of the model would be relatively small and not worth the computational expense. The retina and choroid were modeled as a single layer with thickness equal to that of both tissue layers combined. This was done to avoid the computational expense of the very small elements required for the thin cross sections of the retina and choroid. The optic nerve head and optic nerve were not modeled for the same reason. The aqueous and vitreous geometry resulted from the anterior and posterior chamber geometry defined by the previously described components.

Once constructed, parts were exported from SolidWorks in the ACIS SAT file format. The SAT part files were individually imported into the CUBIT (Sandia National Laboratories, Albuquerque, NM) meshing software. Within CUBIT, the parts were cut into meshable volumes and imprinted to ensure mesh coherence at the cut junctions. Hexahedral meshes were generated for each part. Maximum element size was kept near or below 1 mm in the interest of accurately propagating shock waves (Panzer et al., 2013). The meshed model is shown in Figure 34.

Meshed parts were exported from CUBIT in the LS-DYNA (LSTC, Livermore, CA) keyword file format. The individual parts were imported and assembled in the LSPREPOST software. Contacts were defined for each part to part contact. The lens to zonules, zonules to ciliary body, ciliary body to sclera, and sclera to cornea were attached sequentially using *CONTACT_TIED_SURFACE_TO_SURFACE. This contact

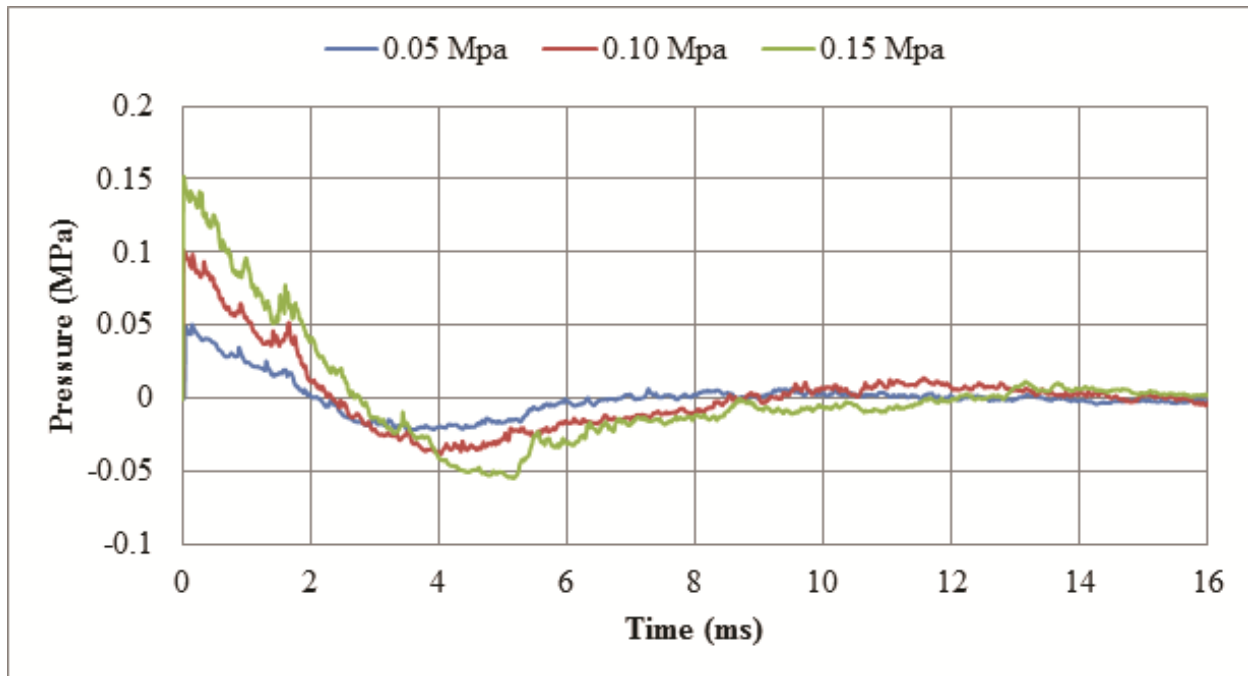


Figure 35. Pressure time histories for three levels of blast used in Porcine Eye FEA model

type ties the nodes and outer segments of the two parts together at the contact interface so that the displacements of adjacent tissues must be equal. Failure of the contact was not modeled at these attachments, as none was expected based on the concurrent physical experiments and previous experiments described in the literature. Contacts between the vitreous and all other structures, retina and all other structures, and aqueous and all other structures were modeled using *CONTACT_AUTOMATIC_SURFACE_TO_SURFACE_TIEBREAK. This contact type allows a failure criterion to be defined specifically for when normal stress or shear stress at the contact junction reaches a user-defined threshold, above which, the contact releases in the area where the stress value was exceeded. Due to a lack of knowledge on the specific failure thresholds for these junctions in the physical eye, the failure values were set to a level believed to be above reported physiological failure levels of the tissues, with the exception of the retina-to-sclera junction. This contact interface was varied experimentally to obtain a failure level that corresponded to retinal detachments observed in the physical experiments. Liu et al. (2013) used a value of 340 ± 78 Pa for the retinal adhesive force. This was used as the initial value in the present model.

The eye was modeled in a rigid holder filled with gelatin, mimicking the experimental setup used in the porcine blast experiments. Rigid boundary conditions and material were used for the holder. The gelatin contact with the holder was tied, as the contacting surfaces of the gelatin and holder did not exhibit relative motion in the physical experiments. Contact between the gelatin and sclera was specified using *CONTACT_AUTOMATIC_SURFACE_TO_SURFACE, with translation allowed

Table 6. Material Properties Used in the Porcine Eye FEA Model

PartName	Density (g/mm³)	Youngs Modulus (Mpa)	Bulk Modulus (Mpa)	Poissons Ratio	Source of Material Properties
Aqueous	0.0010	-	2200	-	Fox 2004
Choroid	0.0010	0.05	-	0.47	Sigal 2004
Ciliary	0.0016	11	-	0.45	Power 2001
Cornea	0.0014	12	-	0.487	Rossi 2011
Gelatin	0.0010	-	2260	-	Power 2001
Lens	0.0011	1.5	-	0.499	Stitzel 2002
Retina	0.0010	0.05	-	0.47	Sigal 2004
Sclera	0.0014	28	-	0.49	Rossi 2011
Vitreous	0.0010	-	2000	-	Fox 2004
Zonules	0.0010	5	-	0.45	Stitzel 2002

between the surfaces. The model including porcine eye structures, ridged holder, and gelatin contained 64,460 elements for a characteristic element size of 1 mm.

Blast loading was applied to the exposed forward facing surfaces of the eye and gelatin using *LOAD_SEGMENT_SET. Static pressure time history recorded in the physical experiments was used. Three cases were represented and defined as peak overpressures of 0.05 MPa, 0.10 MPa, and 0.15 MPa (Figure 35).

Tests of the model with various types of constitutive models for cornea and sclera (linear, viscoelastic, plastic) found little difference in response, with the dominant variable always the stiffness of the tissue. Therefore, linear elastic models were chosen to represent the cornea and sclera. The stiffness of the cornea and sclera was iterated from starting values based on the work of Rossi (2012) and Esposito et al. (2013). Final values were chosen based on matching the experimental BB impact data of the Delori (1969) The aqueous humor was modeled using a linear fluid model available in LS-DYNA. Because of the relatively small deformations of the blast loading and resultant lack of fluid flow, this model was felt to be appropriate and returned acceptable results. The aqueous is compositionally similar to a saline solution and therefore is not expected to exhibit complex rheological behavior. The vitreous humor was modeled with a viscoelastic definition, using properties described by Rossi (2012). The remaining tissues; chorioretina, zonules, ciliary body, and lens were modeled as linear elastic with values taken from various sources in the literature (Table 6). The compressibility of the chorioretina (as indicated by Poisson's ratio) was found to have a significant effect on the model under blast loading. Sigal et al. (2005) reported a range of 0.4 to 0.49 for this property. Using a value of 0.47 (i.e. slightly compressible), the model exhibited more overall deformation and suggested significant compression of the chorioretina. With a Poisson's ratio of 0.49 (i.e. largely incompressible) in the chorioretina the model exhibited a different response than with the 0.47 (largely compressible) and for that

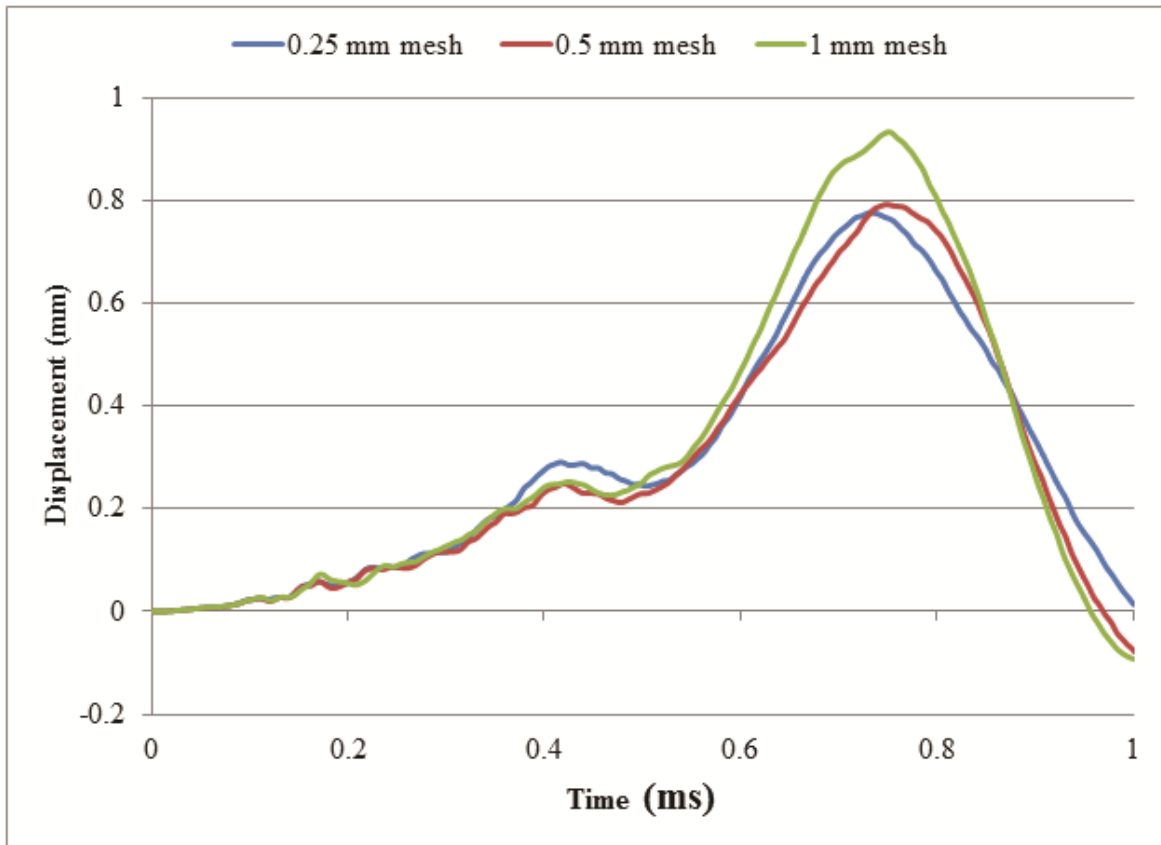


Figure 36. Corneal displacement history of three mesh sizes for peak blast pressure of 0.15 MPa

Table 7. Results of Mesh Sensitivity Study

Metric	0.25 mm mesh	0.5 mm mesh	1 mm mesh	p (rate of converge)	predicted solution	GCI	L ₂ Norm 0.5 mm Mesh*	L ₂ Norm 1.0 mm Mesh*
Corneal Apex Displacement (mm)	0.7762	0.7919	0.9332	1.48	0.7674	0.01417	10.8	19.7
Vitreous Pressure (Mpa)	0.1499	0.1487	0.1453	0.97	0.1511	0.01038	11.5	12.5
Retina Stress (Mpa)	0.0284	0.0276	0.0265	0.66	0.0298	0.06074	10.3	12.0

*Percent change in value relative to L₂ norm for 0.25 mm mesh (smallest mesh size)

reason results are included for models with chorioretina with both values, which will be referred to as compressible and incompressible.

A mesh sensitivity study was performed to determine the ideal balance of mesh size and computational accuracy. Versions of the model were created with 1 mm mesh, 0.5 mm mesh, and 0.25 mm mesh. The 0.15 MPa blast level with 0.47 Poisson's ratio retina was used due to the larger deformation of the mesh in the compressible model. Various measurements, including corneal apex displacement, pressure at the center of the vitreous, and stress at the macula area of the retina, were compared between the three mesh sizes (Figure 36). A Grid Convergence Index (GCI) assessment was performed for peak values of the corneal apex displacement, vitreous pressure, and pressure at the macula (Table 7). The GCI method gives the rate of convergence of the solution as mesh size decreases and predicts the range of error in which the exact solution falls within 95% confidence intervals. This methodology is especially useful for cases such as this where the exact solution is not known. It should be noted that GCI predicts the exact solution of the ideal mesh size of the model; it does not account for material properties, material models, geometry or the many other variables possible in a FEA model. The same three metrics were also evaluated over a time history using the L_2 norm relative error. This method computes the average error between two curves, taken as vectors x and y , by taking the error at each point.

$$L_2 = \sqrt{\frac{\sum(x - y)^2}{\sum(x)^2}}$$

The L_2 norm is sensitive to small fluctuations in the data if they happen to be out of synch. The nature of the data in this experiment includes high frequency noise in some measurements and the relative error between different mesh sizes can be moderate, while the overall shape of the curve is fairly well matched. The 0.25 mm mesh was used as the baseline for this analysis. The results of the L_2 norm analysis showed a slight decrease in the normalized error between the 0.5 mm mesh and 1.0 mm mesh (Table 7). The small amount of error between the 0.5 mm mesh and GCI predicted exact value was acceptable given the shorter run times. Therefore, the 0.5 mm mesh was deemed sufficiently dense to reproduce the key features of both primary blast and blunt impact in the porcine eye model. All subsequent results are reported based on this mesh.

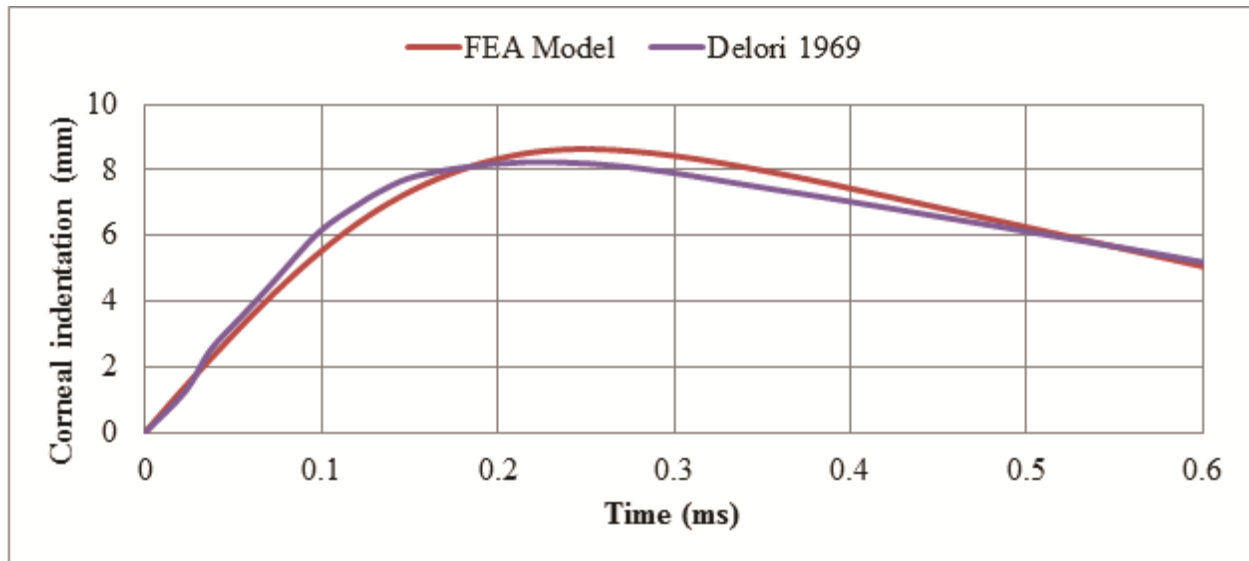


Figure 37. Corneal Indentation for FEA model and Delori (1969) experimental data.

2.10.1.1 Model Validation

Validation of the model was performed against projectile impact studies, namely the 1969 study by Delori in which porcine eyes were impacted with BBs. BB impact subjects the eye to much more extreme deformation with higher stress and strain than the low level blast used in this study. The impact FEA model showed similar rate pressure reflections within the eye, albeit at higher levels than the blast model. This projectile study was used because the data is much more complete than that of existing blast studies, giving time histories of various external deformation parameters. Current blast experiments, including the concurrent SLOT project, offer binary measurements of whether or not an injury occurred. The Delori experimental setup was duplicated as closely as possible within the computational modeling environment. A 4.5 mm diameter, 0.345 gram BB impacted the center of the cornea at a velocity of 62.3 m/s. Indentation of the cornea, equatorial variation, and longitudinal variation of the globe were measured versus time and compared to the data reported by Delori. Model predictions were highly correlated with the experimental data (Figure 37). L_2 norms were 5.5% for corneal displacement, 2.2% for equatorial variation, and 9.7% for longitudinal variation.

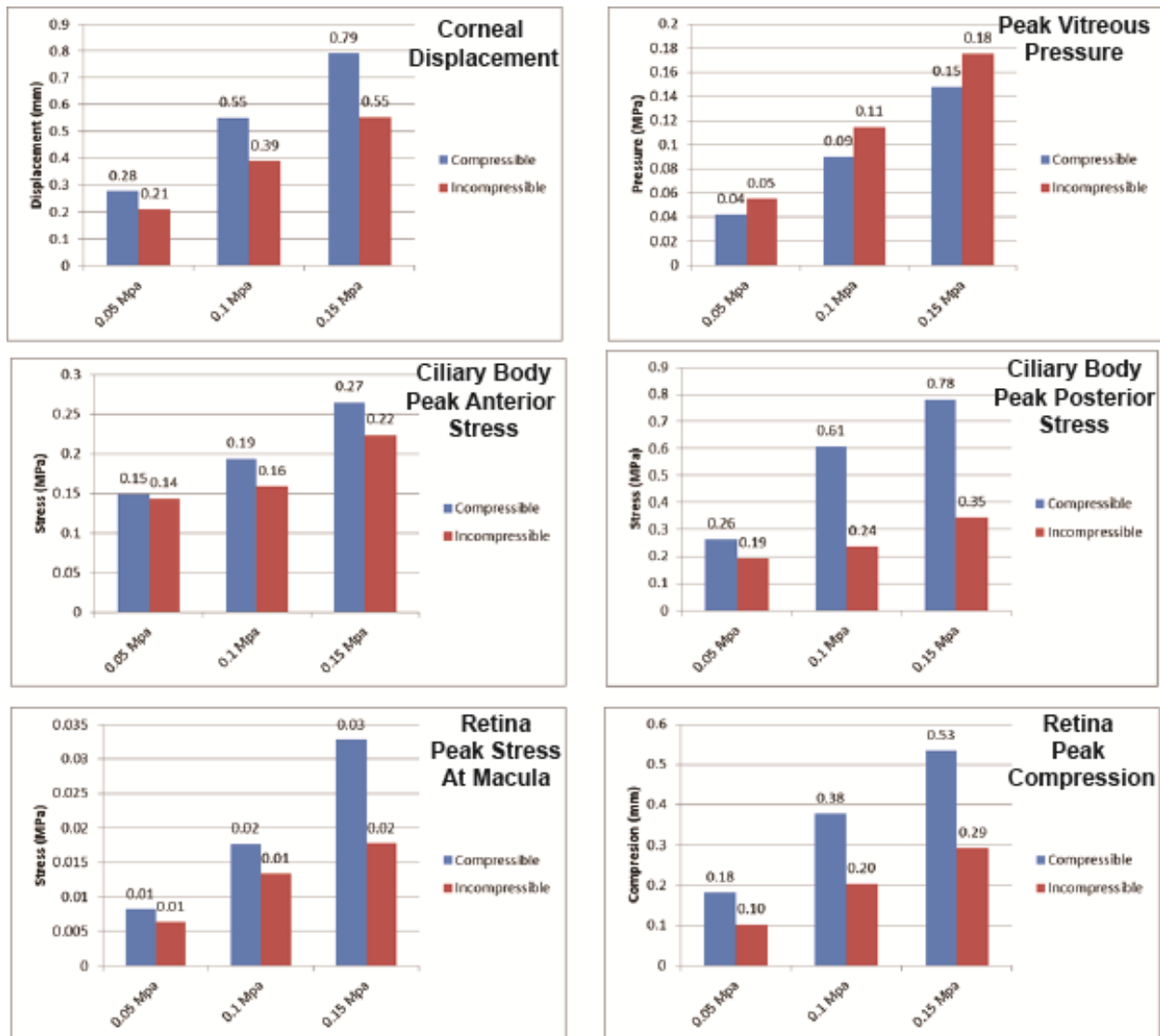


Figure 38. LS-DYNA Porcine Eye Model predictions for peak blast overpressure of 0.05 MPa, 0.10 MPa, and 0.15 MPa.

2.10.1.2 Model Predictions Compared to Experimentally Observed Trauma

For the range of primary blast overpressure used in the porcine eye experiments, the LS-DYNA model predicts that stress, pressure, and displacement will increase with higher levels of blast overpressure. Measurements included corneal apex displacement, pressure near the center of the vitreous, stress at the anterior and posterior surface of the ciliary body, stress and compression at the macula of the retina, and stress in the sclera (Figure 38). These metrics were selected to allow correlation with observable responses in the physical experiments. Corneal apex displacement can be visually observed in the high speed video of the physical tests, with limited capability for

measurement. Stress in the ciliary body was of interest due to the number of angle injuries observed in the physical experiments. Scleral and retinal measurements of stress were also performed due to commonly observed damage in these regions during physical experiments. In the compressible retina model, all stress and displacement measures were lower than those for the incompressible retina model at all levels of blast. For pressure measurements this was reversed, with the less compressible model displaying higher pressure in the vitreous.

The response of the model to the blast was initial longitudinal compression and rearward displacement with equatorial expansion. The compression chiefly involved the anterior chamber, lens, and vitreous moving rearward while the posterior sclera remained largely in place. Following maximum compression, the model rebounded back toward its original shape while undergoing complex oscillations. Using the full positive and negative phase of the blast data, the model would avulse from the gelatin. Complete avulsion of the eye from the gelatin was observed in a number of the physical experiments at the 0.15 MPa blast level. Internally, the individual components of the model oscillated at different frequencies according to mass and stiffness. Overall displacement of the cornea at the highest level of blast, 0.15 MPa, was on the order of 1 mm, in agreement with high speed video of the physical blast experiments.

The model showed increased levels of stress in areas of injury found in the SLOT physical experiments, namely the ciliary body (angle), sclera, and retina (Figure 39a). The highest levels of stress were found in the sclera in the region of the vitreous base. These values ranged up to 1 MPa, and were approximately 75% higher for the compressible retina model than the incompressible model. The peak stress in this area was coincident in time with the initial compression phase of the eyeball over the first 1 ms of the simulation. The areas of maximum stress were found in the thinnest section of the sclera, adjacent to the vitreous base, centered longitudinally at the vitreous base attachment (Figure 39c). This section of the sclera acts as a hinge between the anterior and posterior chambers, which displayed relative differential movement in the model. The attachment of the relatively massive vitreous places additional stress on this area as it resonates out of phase with the movement of the sclera. The stress concentration in this area correlated well with the equatorial location of scleral delamination observed in the physical experiments (Figure 39c).

The next highest levels of stress were found in the ciliary body at its posterior surface, ranging up to 0.8 MPa (Figure 39b). The stress in this region was induced by differential movement with the attached vitreous, occurring later in time compared to the nearby stress in the sclera, coincident with the initial rebound of the anterior chamber following its rearward displacement at the onset of the blast wave. Again, the level of regional stress was decreased in the incompressible retina model. The anterior surface of the ciliary body returned stress levels up to 0.27 MPa when subjected to the most severe blast. The source of this stress appeared to be fluctuating pressure in the aqueous humor.

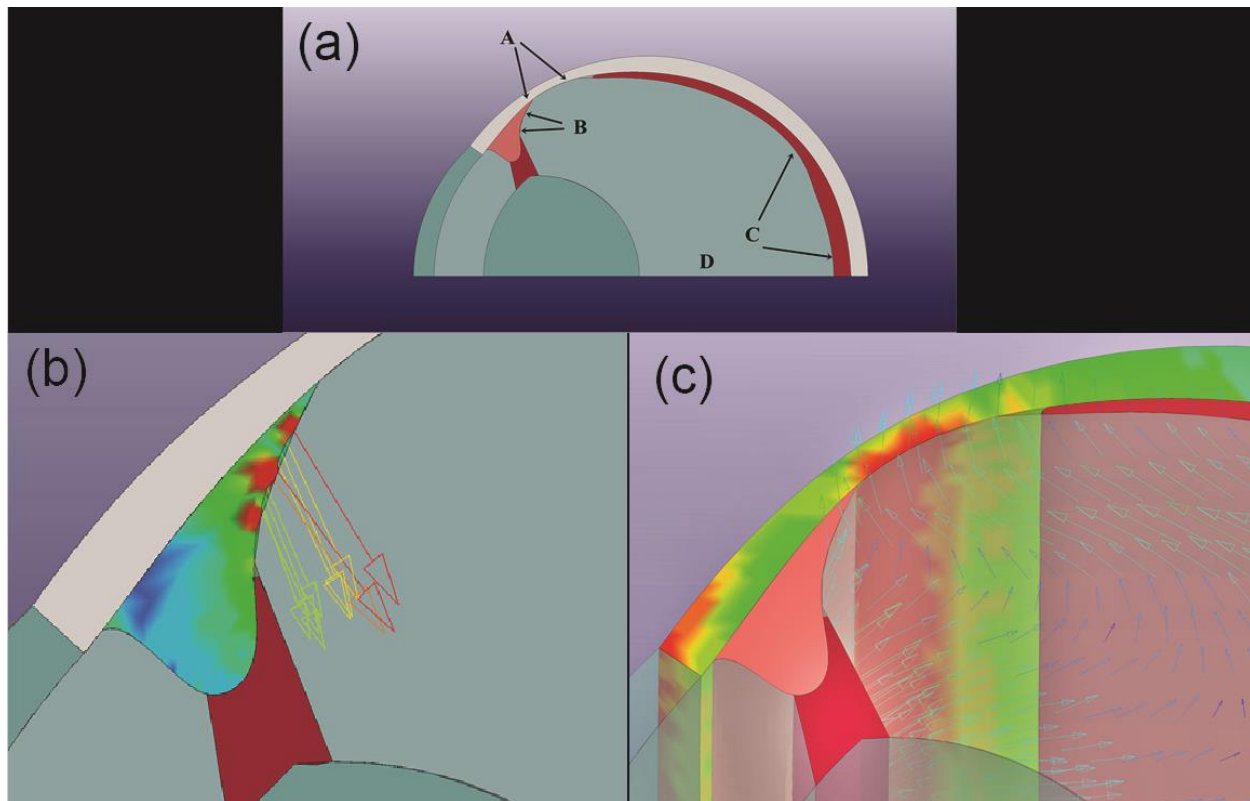


Figure 39. (a) The model showed increased levels of stress in areas of injury found in the SLOT physical experiments, namely the ciliary body (angle), sclera, and retina. Arrows show instantaneous movement of (b) vitreous relative to ciliary body, and (c) vitreous relative to zonules and sclera.

Angle recession and cyclodialysis were the most common findings in the physical experiments. The model suggests a possible mechanism for these injuries as the ciliary muscles are pulled on by the vitreous from behind at the same time the anterior portion of the sclera to which the ciliary muscles are attached rebounds forward. This finding merits follow on work with a more detailed description of the individual ciliary muscles and zonules. Material property testing of the ciliary muscles and their adhesion to the vitreous and sclera would benefit this effort.

Rearward displacement of the vitreous compressed the retina between the vitreous and the sclera. This compression occurred with both the compressible and incompressible retina material properties. The maximum compression of the retina predicted by the compressible model was a 62% decrease in thickness at the retinal apex, with 33% compression in the incompressible retina model. For the highest level of blast, peak pressure on the retina was 0.36 MPa in the incompressible model and 0.30 MPa for the compressible model. Stress levels in the retina were an order of magnitude lower than the pressure, 0.02 to 0.03 MPa. Retinal detachments were among the most serious injuries in the porcine blast experiments. The model indicates a coup-contracoup mechanism of injury to the retina due to the movement of the vitreous. The

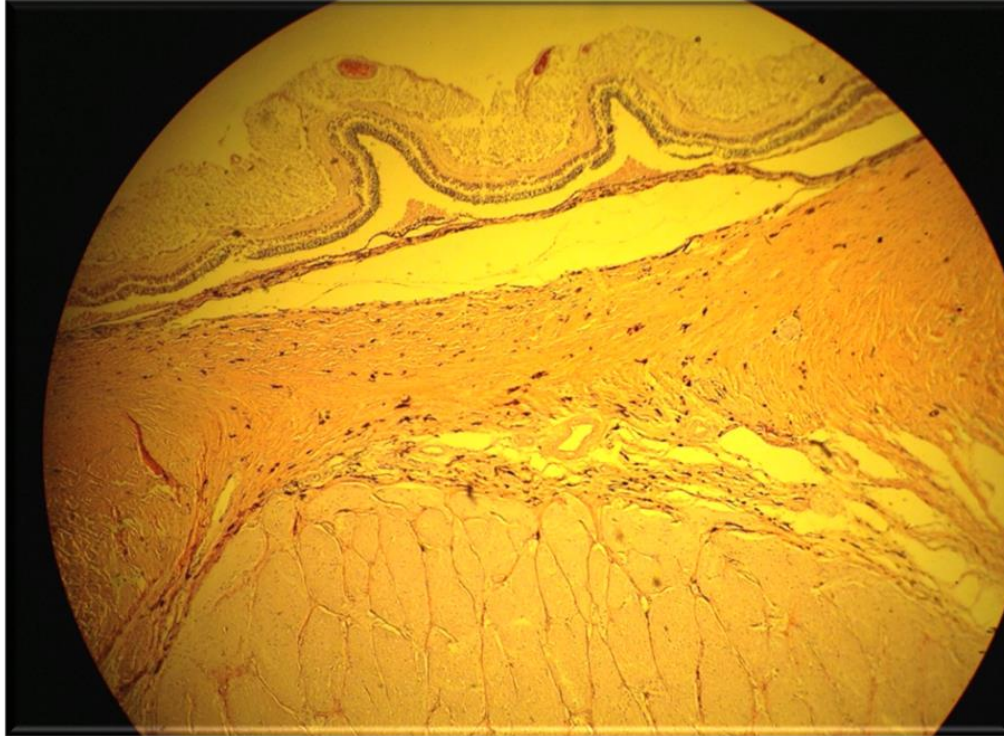


Figure 40. Retinal detachment in region of blood vessel observed during one of the porcine blast experiments

findings on retinal dynamics merit further work with more detail. It is known that the retina is non-homogenous, with blood vessels throughout it. Histopathology suggests that the junction between the different material properties of the retina and blood vessel is susceptible to the initiation of a retinal detachment (Figure 40). The optic nerve head presents the same type of discontinuity, along with the tethering effect of the optic nerve. Though modeling these very thin tissues would be computationally intensive it may be possible to create smaller sub models based on the overall loading conditions determined with the present whole-eye model.

Differential movement of internal structures, particularly the vitreous was shown to be a likely mechanism of injury to the retina, sclera, and ciliary body. The vitreous accounts for more than 50 percent of the mass of the eyeball, is largely incompressible, and is strongly attached to the sclera and ciliary body over a relatively small area. These characteristics contribute to the stresses imposed by the movement of the vitreous on smaller and more delicate structures of the eye. The characteristics of the retina, mainly the compressibility, play a role in determining the magnitude of movement of the vitreous and in turn the amount of stress at the sclera and ciliary body. The model shows that loading by sub lethal levels of blast overpressure is capable of causing internal injury to the eye, warranting careful examination of the eyes of those exposed to survivable blast.

2.10.1.3 Limitations of the FEA Model

Dynamic FEA models of soft tissue structures are subject to certain limitations. The primary limitation is the lack of material properties derived specifically for use in a computational model intended to simulate high loading rates. Though the material models are capable of simulating rate effects and anisotropy, few tissues are characterized this way, particularly for the extremely rapid loading imposed by blast. Though care was taken to ensure the model had a coherent response when compared to physical experiments, the addition of more detailed and specific material properties would significantly improve the model. Secondly, the eye contains many small structures such as the zonules, blood vessels, iris, lamina cribosa, et cetera. These structures are of interest when characterizing certain injuries. However, modeling them with FEA as part of a larger overall model of the eye would require extremely fine mesh, leading to a very computationally expensive model. Finally the internal contacts between tissues in the eye have not been characterized and are therefore not well defined in the FEA model. The connection between the vitreous and retina in particular is not well quantified. The dynamics of the model in this work show that any connection between the vitreous and retina would induce traction force on the retina, contributing to retinal detachments.

2.10.2 CTH

CTH modeling efforts focused on modeling blast wave generation in the shock tube. The objective was to investigate the initial loading conditions required to generate Friedlander waveforms similar to those observed in the porcine eye experiments, i.e., sharp shock front with correct peak pressure and pulse width. Unlike LS-DYNA where the pressure-time history can be directly input to the program, CTH must generate the waveform as part of the computation. In this case, a volume of high pressure air is placed in the upstream end of the shock tube and allowed to propagate toward the open end of the shock tube. This is analogous to pressurizing the shock tube's driver section and allowing the aluminum disk to rupture. As air propagates down the tube, a shock front or Friedlander waveform develops (Figure 41).

Due to symmetry, a 2-D geometrical model was deemed adequate for simulating the performance of the shock tube. Each computational cell was 0.25 x 0.25 cm in size resulting in a total of 164,000 cells. An embedded tabular equation of state model (SESAME table) was used to simulate the air, and the shock tube is modeled as a rigid (impermeable, non-moveable) material. In the initial trials the correct pulse width (~ 2 ms) was consistently achieved for a number of peak pressures, but the negative pressure phase (see Figure 3) was not achieved. However, through trial and error we were able to replicate this by using a sound speed absorbing boundary condition (condition 1 in CTH) at the open end of the tube. The choice of this particular boundary condition was not an obvious choice, as our first inclination was to allow the air to exit the open end (condition 2 in CTH). However, this did not consistently produce the

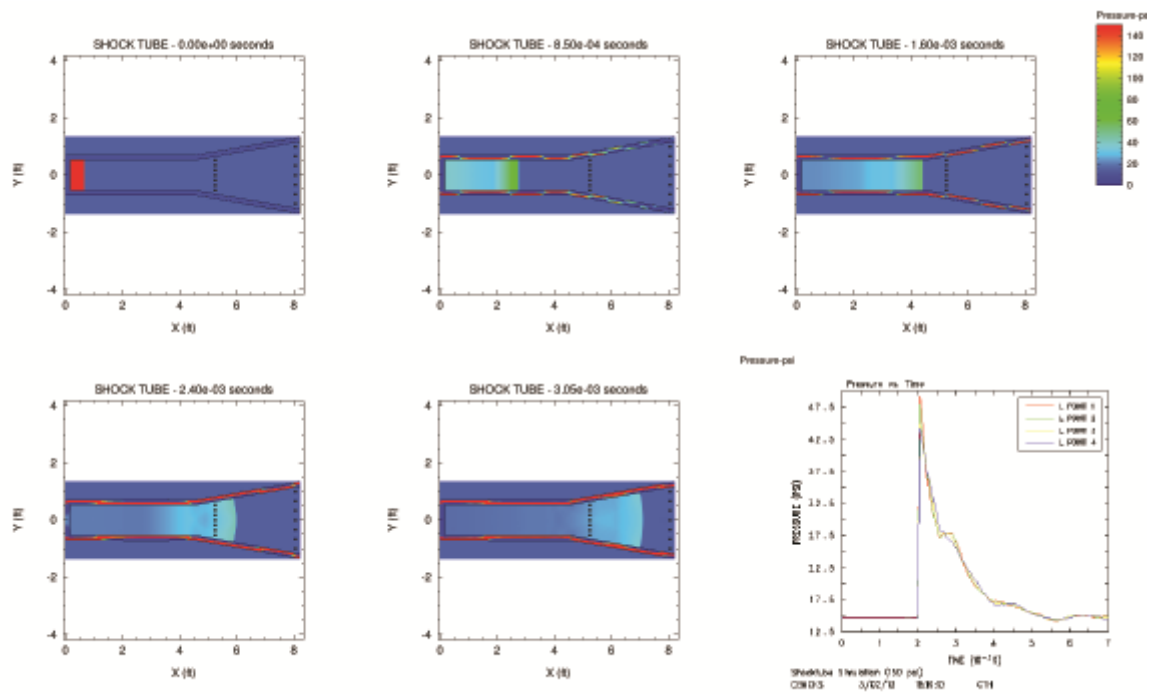


Figure 41. CTH simulation of the shock tube. The simulation is started by placing a volume of high pressure air at the upstream end and allowing it to propagate down the tube. The shock front (Friedlander waveform) develops at the open end.

desired negative pressure phase, and on occasion caused the computation to terminate early due to mass balance errors. CTH assumes mass conservation in the calculations, so letting mass exit the computational grid sometimes results in non-convergence during iteration.

The next series of CTH computations placed an eye-orbit mimic model at the open end of the tube in a configuration similar to that employed in the porcine eye experiments (Figure 42). The eye-orbit mimic assembly was held in place with a rigid tube that was fixed in place (not allowed to move in the computations) and extended out the open end of the tube. Due to the rotational symmetry of the eye, an axisymmetric model was utilized with the eye centerline as the axis of rotation. The small thickness of the ocular tissues (e.g., sclera ~ 1 mm) required a much more refined grid than was used in the shock tube simulations. A grid size of 0.20 x 0.20 cm was chosen to ensure at least 5 computational cells across the scleral thickness. This resulted in approximately 1.4 million computational cells with run times in excess of 1 week.

Dimensional and geometric details of the eye and orbit were taken predominately from a single reference; Wolff's Anatomy of the Eye and Orbit, 8th Edition (Bron et al., 2001). The structures important to modeling dynamic response and trauma were

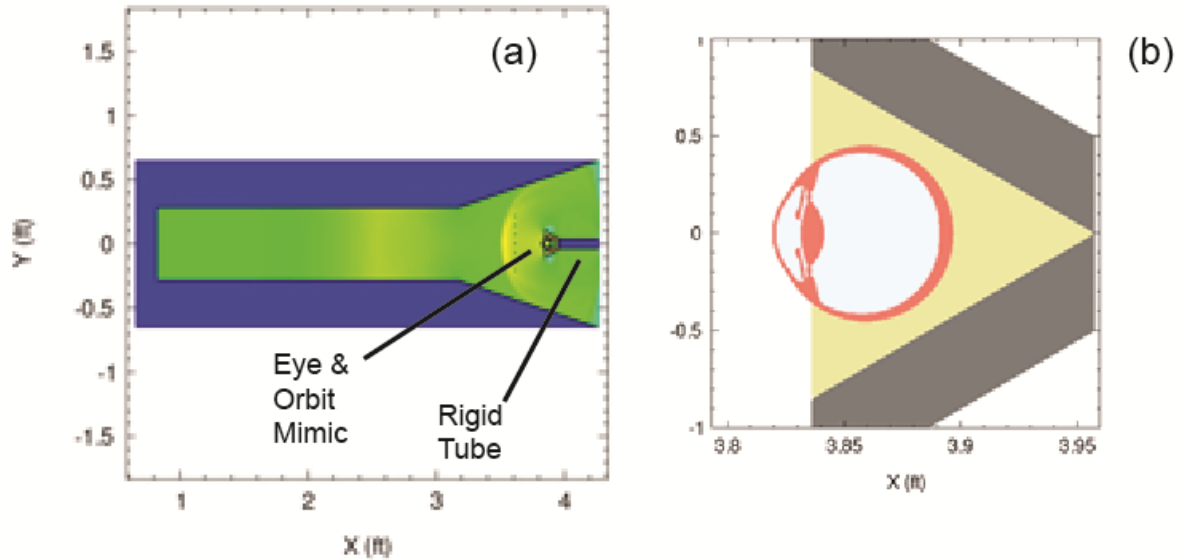


Figure 42. (a) CTH model of the shock tube with eye-orbit mimic included. The eye-orbit assembly is held in place by a rigid tube that is not allowed to move during the computations. (b) Close up of the eye-orbit mimic model. Note that gelatin is placed between the eye and orbit mimic to simulate the extraocular muscles.

identified as the cornea, aqueous humor, iris, zonule, lens, vitreous, sclera, retina, and choroid (Figure 42b). The sclera, retina, and choroid have been combined into a single scleral shell as modeling the individual layers is not practical in CTH (due to their thinness). However, it has been shown in previous work that deformation and strain partitioning can be adequately modeled using a single scleral shell approach.

Representative mechanical properties of the ocular tissues used in the CTH model are presented in Table 8. The heat capacity, Grüneisen Parameter, and Up-Us slope (slope of Hugoniot curve) of all tissues were taken to be those of water. This assumption was considered reasonable as human tissue is thought to contain considerable water either in solution or suspension. In the simple model the retina, choroid, and sclera were modeled as a single membrane using the scleral properties. To simulate material response, a Mie-Grüneisen equation of state and a modified Johnson-Cooke constitutive model were used for each tissue.

A number of CTH calculations at the various blast pressure conditions observed in the porcine experiments are currently underway. Consistent with experimental observations, peak blast pressures in the 48 kPa to 151 kPa range are producing low levels of stress and strain in the eyes, mostly in the corneal and scleral region (Figure 43). In early times (associated with blast wave arrival) stress is concentrated in the cornea, but propagates to the mid- and posterior scleral regions in late times. The propagating stress may be due to a minor flattening of the globe from pressure loading or simply a response to interior pressure wave propagation. In most of the simulations pressure reflections off the posterior can be observed (Figure 44). Our previous

Table 8. Mechanical Properties of the Ocular Tissues

	Density kg/m ³	Young's Modulus (Pa)	Poisson's Ratio	Sound Speed (m/s)	Yield Stress (Pa)	Failure Stress (Pa)	Heat Capacity J/(kg-K)	Guneisen Parameter	Up-Us Slope
Optic nerve	1400	6.56E+06	0.49	1540	1.50E+03		3664	0.1	2
Retina	1400	5.20E+03					3664	0.1	2
Dura	1400	3.58E+08	0.47	1540	9.40E+06	9.49E+06	3664	0.1	2
Lens	1079	6.89E+06	0.49	1540		1.75E+07	3664	0.1	2
Cornea	1400	1.24E+08	0.42	1540	9.40E+06	9.45E+06	3664	0.1	2
Iris	1400	1.24E+08	0.42	1540	9.40E+06	9.45E+06	3664	0.1	2
Ciliary Body	1400	3.58E+08	0.47	1540	9.40E+06	9.49E+06	3664	0.1	2
Zonule	1000	3.58E+08		1540			3664	0.1	2
Sclera	1400	3.58E+08	0.47	1540	9.40E+06	9.49E+06	3664	0.1	2
Choroid	1400	3.58E+08	0.47	1540	9.40E+06	9.49E+06	3664	0.1	2
Aqueous Humor	1003	--	--	1503	--	--	3664	0.1	2
Vitreous	1009	1.54E+05	0.49	1528	1.0E+1	1.57E+05	3664	0.1	2
Orbital Bone	1610	9.81E+10	0.35	2503	1.57E+08	1.57E+08	1256	0.1	2

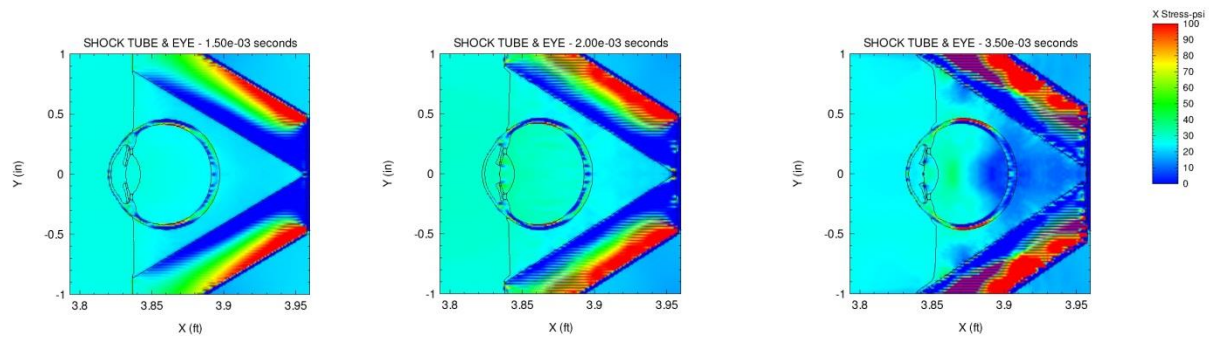


Figure 43. CTH simulation of 151 kPa peak pressure showing development of low level stress (~ 100 psi) in the mid-sclera regions of the eye. CTH simulations have shown that in early times stress is concentrated in the cornea, but propagates to the scleral regions at late times

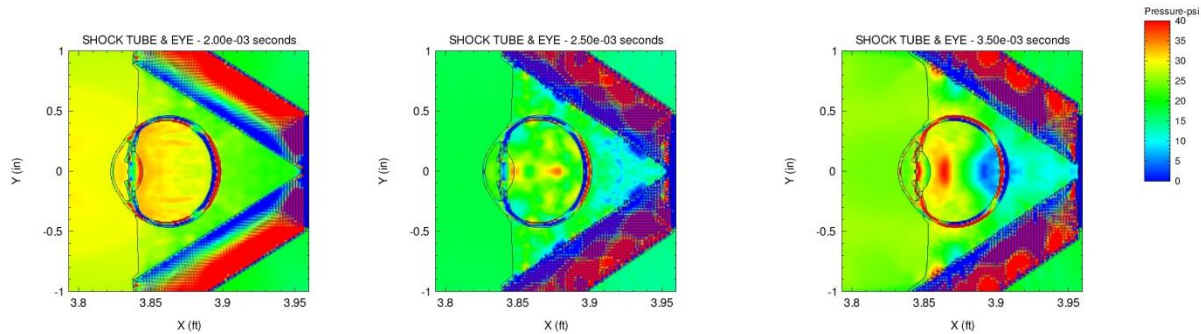


Figure 44. CTH simulation at 151 kPa peak pressure showing pressure reflection off posterior. Our research has suggested that such reflections may be responsible for retinal detachments.

research with blunt impact events suggests that such reflections may contribute to retinal detachments.

3. KEY RESEARCH ACCOMPLISHMENTS

- Completion of 85 shock tube experiments on porcine eye specimens. Detailed procedures for preparation and blast testing of eye specimens have been developed and validated.
- Completion of pathology (including assessment of trauma types and levels) on 55 porcine eye specimens (43 blast exposures and 13 controls). To date the pathology assessment has relied on post-blast screening using ultrasound techniques (UBM and B-scan), supplemented by limited dissection and histopathology. The ultrasound techniques provide clear information about the chorioretina (pre- and post-impact), but are unable to adequately resolve trauma in the angle region. Although dissection and histopathology can resolve trauma in the angle region, the potential for artifact is increased.
- Development of rigorous control procedures that allow an estimation of the relative effects of shipping, handling, mounting, preparation, tissue degradation, and re-pressurization of the globe in development of injuries not related to primary blast. These controls are included in every blast test performed.
- Development of a scoring methodology on a per-tissue basis that allows for interpretation in the framework of the OTCS zone-based scoring system.
- Preliminary development of trauma risk curves for a number of sub-globe-rupture trauma categories.
- Completion of preliminary numerical simulations using software packages CTH and LS-DYNA. The LS-DYNA simulations have been particularly fruitful in

revealing mechanical response that contributes to chorioretinal trauma, namely oscillatory compression and tension on the retina during wave propagation through the eye. Separation of the vitreous and retina, as observed in the simulations, may contribute to retinal detachments.

- Optic nerve specimens have been successfully cut and mounted in preparation for imaging using the Matrix Assisted Laser Desorption Ionization (MALDI) technique. The sections were mounted on the ITO slides from a methanol layer, and appear to have attached well on to the slides after evaporation of the methanol. Trauma-related proteins will be identified by the homology of the measured m/z spectra with protein sequences published in the UniProt database
- Development, submission, and approval of animal use protocol for *in vivo* rabbit blast exposures (A-14-007, approved by ISR IUCAC and the USAMRMC Animal Care and Use Review Office).
- Completion of 13 *in vivo* rabbit blast experiments with collection of blood and aqueous fluid sample for biomarker study, along with eyes and brain tissues for TBI study.
- Completion of pre- and post-blast imaging on 13 rabbits including (1) Direct Ophthalmoscope, (2) Slit Lamp, (3) Fundus photography, (4) OCT (retinal), (5) HRT Corneal Conformal, and (7) Ultrasound (UBM, B-scan).
- Identification of potential trauma-related biomarkers of use in ocular trauma studies of the *in vivo* rabbit blast experiments.
- Development and validation of Assisted Laser Desorption Ionization (MALDI) imaging for use in detection of tissue-based biomarkers.

4. REPORTABLE OUTCOMES

Two abstracts/posters submitted by the team were presented at the 2013 ARVO Meeting in Seattle:

(1) A Computational Models for Investigation of Ocular Trauma Due to Primary Blast

Presentation Number: 3045
Posterboard Number: C0208
Session Number: 321
Session Title: Anatomy

(2) Primary Blast-Induced Ocular Trauma Modulated by Peak Pressure

Presentation Number: 3043
Posterboard Number: C0206
Session Number: 321
Session Title: Anatomy

Two abstracts/posters were submitted by the team at the 2014 ARVO Meeting in Orlando:

(1) Computational Modeling of Internal Eye Injury due to Primary Blast

Presentation Number: 4453
Posterboard Number: D0113
Session Number: 423
Session Title: Anatomy Development

(2) The Identification of Trauma-Related Biomarkers Following Blast Injuries to the Eye

Presentation Number: 4469
Posterboard Number: D0129
Session Number: 423
Session Title: Anatomy Development

One abstract/poster submitted by the team was presented for the Biomedical Engineering Society (BMES) Annual Meeting, September 25-28, 2013 in Seattle:

(1) Primary Blast-Induced Ocular Trauma

Submission ID: 2573
Submission Title: Submission Track: Biomechanics
Submission Subtrack: Other/Non-Specified

Three abstracts have been accepted for presentation at the Biomedical Engineering Society (BMES) annual meeting scheduled for October 22-25, 2014 in San Antonio, Texas:

(1) Blast Induced Traumatic Brain Injury: Detection Through Immunocytochemistry and MALDI

Submission ID #543

(2) A Computational Model of the Porcine Eye

Submission ID #537

(3) Primary Blast Influences Incidence and Severity of Ocular Injury in a Porcine Eye Model

Submission ID #1114

A paper titled “*Anatomical manifestations of primary ocular trauma observed in a post-mortem porcine model*” has been published in the journal *Investigative Ophthalmology and Visual Science* (2014; 55:1124-1132).

Two Master’s Degree theses have been submitted by graduate students at UTSA under the supervision of SLOT team members and funded by the VRP Grant:

- (1) Daniel Sherwood, Determining the probability of ocular trauma from survivable primary blast. [Master’s Thesis], University of Texas at San Antonio, 2014.
- (2) Richard Watson, A computational model of the porcine eye for investigation of primary blast. [Master’s Thesis], University of Texas at San Antonio, 2014.

5. CONCLUSIONS

The data generated in in this study has significantly increased our understanding of primary blast-induced ocular injury. This shock tube produced a broad array of closed-globe injuries, many of which would seriously compromise visual function. The experimental techniques and injury characterization methodologies offer an objective assessment as to which injuries were due to blast exposure. Pre-imaging each eye using ultrasound allowed exclusion of eyes that would otherwise contribute artifacts and improves confidence that any damage to the eye after blast exposure is due only to the effects of primary blast rather than preparation or other factor.

A notable strength of this study is the evaluation of the blast trauma with the complimentary methods including UBM, B-scan, gross dissection and histopathology. Specifically, our results show that ultrasound scans give clear information about the chorioretina (pre- and post-impact) while dissection can result in artifact. Conversely, the ultrasound methods were unable to resolve angle recession while histological sections gave more reliable information regarding anterior segment damage. In combination these modalities assist in the primary objective of identifying intraocular injuries that could have lifelong adverse effects.

Previous blunt impact studies conducted with paintballs found an ocular damage threshold of 2-13.5 J (Sponsel et al., 2011). The present study found a similar increasing trend in ocular damage with increasing blast energies, but globe distortion and movement were far less than in the paintball study. This may be due to several factors such as the lower energies associated with the blast, simultaneous compression of the periorbita, and distribution of the energy over the entire exposed surface rather than concentrating the load at the point of projectile impact. None the less, we observed

a broad array of ocular injuries. Petras et al. (1997) observed a similar trend in rats exposed to overpressures of 104 –173 kPa (15-25 psi).

For this study we chose to use porcine eyes to eliminate effects due to age, health history, and other uncontrollable factors. However, porcine eyes are known to have a higher mechanical strength than human eyes (Kennedy et al., 2007), suggesting that blast conditions that produce injuries in porcine eyes will likely induce more serious injuries in the human eye. Thus, the injury data generated from porcine eyes should give conservative estimates of injuries which might occur in human eyes during primary blast events.

Control eyes experienced some apparent damage which was clearly not due to blast exposure. This may indicate continual degradation of the porcine eyes after the pre-screening ultrasound was performed, damage inflicted to the eye due to the presence of the gelatin and/or other artifacts of the preparation. Still, incidence and severity of damage in the exposed eyes was significantly correlated with the impulse indicating that primary blast modulated these injuries.

Ocular trauma scores describe a range of open and closed globe injuries. Current ocular trauma scores, like the Ocular Trauma Classification System (OTCS) or the Birmingham Eye Trauma Terminology (BETT; Kuhn et al., 2004) subdivide open globe injuries between lacerations and ruptures while subdividing closed globe injuries between contusions and lamellar lacerations. Cockerham et al. (2009) noted a need for the development of a universal parlance in describing blast-related ocular injuries. Such a scale must account for the full range of ocular injuries from the subtle, closed-globe nature of primary blast injuries observed here through globe rupture.

Continued experimentation in this area will allow more robust correlation between the blast wave characteristics and frequency of trauma response. Ultimately, a probabilistic regression model predicting the likelihood of a specific type of injury similar to the Bowen curves will enable informed treatment by medical staff. Our parallel computational studies seek to use numerical modeling of blast exposure to understand the mechanisms of these injuries, similar to the approach recently undertaken by Bhardwaj et al. (2013). The modeling should soon provide rapid, inexpensive methods for testing various protective eyewear solutions which might mitigate blast damage to the eye.

The computational eye models provided the opportunity to visualize the interior structures of a surrogate eye during the extreme dynamics of a blast event and provided insight into mechanisms of primary blast injury. Of particular interest was the response of the LS-DYNA model at the interface of the vitreous and retina. A series of snapshots of the model progressing forward in time shows contours the motion of the vitreous as it encounters the retina, compressing it and the choroid against the sclera. This compression is followed by rebound of the vitreous away from the retina. Given the reported tensile strength of the choroid and retina, this finding indicates a high likelihood of damage to the retina via the interaction with the vitreous in both tension and

compression. The degree of compression of the retina was related to the peak overpressure, with maximum compression occurring at the highest blast overpressures. Statistical analysis of the physical experiments also showed increasing risk of retinal injury with the higher blast overpressures.

Differential movement of internal structures, particularly the vitreous was shown to be a likely mechanism of injury to the retina, sclera, and ciliary body. The vitreous accounts for more than 50 percent of the mass of the eyeball, is largely incompressible, and is strongly attached to the sclera and ciliary body over a relatively small area. These characteristics contribute to the stresses imposed by the movement of the vitreous on smaller and more delicate structures of the eye. The characteristics of the retina, mainly the compressibility, play a role in determining the magnitude of movement of the vitreous and in turn the amount of stress at the sclera and ciliary body. The model shows that loading by sub lethal levels of blast overpressure is capable of causing internal injury to the eye, warranting careful examination of the eyes of those exposed to survivable blast.

During *in vivo* rabbit blast experiment an extensive imaging series was conducted on each rabbit before and after blast exposure to identify and characterize any blast-induced ocular trauma. The imaging included (1) Direct Ophthalmoscope, (2) Slit Lamp, (3) Fundus photography, (4) OCT (retinal), (5) HRT Corneal Conformal, and (7) Ultrasound (UBM, B-scan). All imaging analysis was performed on both OD & OS eyes. Slit lamp images were used to observe any surface corneal damage as well as sphincter ruptures that could be present post-blast. The repeated measures ANOVA results reveal an overall increase in the nerve fiber layer (um) after blast (p-value = 0.008). Some retinal edema was observed in fundus images but must be confirmed with OCT measurements. B-scan images have all appeared normal with no indication of retinal detachment. UBM data has not yet been analyzed. No iris sphincter ruptures have been observed in slit lamp images.

6. REFERENCES

- Asejczyk-Widlicka M., Pierscionek B. K., 2008, The elasticity and rigidity of the outer coats of the eye: *British Journal of Ophthalmology*, v. 92, pp. 1415-1418.
- Bhardwaj, R., Ziegler, K., Seo, J.H., Ramesh, K.T., and Nguyen, T.D., 2013, A computational model of blast loading of the human eye: *Biomech Model Mechanobiol*, v. 17 (Epub ahead of print, April 2013).
- Bowen, I.G., Fletcher, E.R., and Richmond, D.R., 1968, Estimate of Man's tolerance to direct effects of air blast: Defense Atomic Support Agency Report, DASA 2113, 44 p.
- Bron, A.J., Tripathi, R.C., and Tripathi, B.J., 1997, *Wolff's Anatomy Of The Eye And Orbit*. Hodder Arnold Publishers, London, eighth edition, 1997.
- Burd, H.J., Judeg, S.J., and Cross, J.A., 2002, Numerical modeling of the accommodating lens: *Vision research*, v. 42, pp. 2235-2251.
- Cockerham, G.C., Goodrich, G.L., Weichel, E.D., 2009, Eye and visual function in traumatic brain injury: *J Rehab Res Dev.*, v. 46, pp. 811-818.
- Collett, D., 2003, *Modeling Binary Data*: Chapman & Hall, 228 p.
- Duke-Elder S, 1954, Concussion injuries, *Text-book of Ophthalmology*, Vol VI: Injuries: Henry Kimpton, London: 5751-5961.
- Duma, S.M., Ng, T.P., Kennedy, E.A., Stitzel, J.D., Hering, I.P., and Kuhn, F., 2005, Determination of significant parameters for eye injury risk from projectiles: *Journal of Trauma*, v.59, pp. 960-964.
- Duma S, and Kennedy, E., 2011, Final Report: Eye Injury Risk Functions for Human and FOCUS Eyes: Hyphema, Lens Dislocation and Retinal Damage: USAMRMC report W*!XWH-05-2-0055, 66 p.
- Esposito, L., Clemente, C., Bonora, N., Rossi, T., and, 2013, Modeling human eye under blast loading: *Computer Methods in Biomechanics and Biomedical Engineering*, <http://www.dx.doi.org/10.1080/10255842.2013.779684>.
- Gray, W., Weiss, C.E., Bonivitch, A.R., Sponsel, W.E., Scribbick, F. W., Miller, P.Armstrong, A.A., Walker, J.D., and Nicolella, D.P, 2008a, Modeling of paintball ocular trauma: A path towards development of an impact and blunt trauma predictive capability: SwRI Internal Research Report No.18.R9664, 59 p.

- Gray, W., Weiss, C.E., Sponsel, W. E, 2008b, Computational and experimental study of paintball impact ocular trauma: Proceedings 24th International Symposium on Ballistics, pp 1260-1267.
- Gray, W., Sponsel, W.E., Scribbick, F.W., Stern, A.R., Weiss, C.E., Groth, S.L., and Walker, J.D., 2011, Numerical modeling of paintball impact ocular trauma: Identification of progressive injury mechanisms: Investigative Ophthalmology and Visual Science, v. 52, pp. 7506-7513.
- Grey, A.C., Chaurand, P., Caprioli, R.M., Schey, K.L., 2009, MALDI imaging mass spectrometry of integral membrane proteins from ocular lens and retinal tissue: J. Proteome Res. V. 8, pp.3278-3283.
- Kennedy, E.A., Voorhies, K.D., Herring, J.P., Rath, A.L., and Duma, S.M., 2004, Prediction of severe eye injuries in automobile accidents static and dynamic rupture of the eye: Annu Proc Assoc Adv Automot Med, v. 48, pp. 165-179.
- Kennedy, E.A., Ng, T.P., McNally, C., Stitzel, J.D., and Duma, S.M., 2006, Risk functions for human and porcine eye rupture based on projectile characteristics of blunt objects: Stapp Car Crash Journal, v. 50, pp. 651-671.
- Kennedy, E.A., McNally, C., and Duma, S.M., 2007, Experimental techniques for measuring the biomechanical response of the eye during impact: Biomedical Science Instrumentation, v. 43, pp. 7-12.
- Kennedy, E.A., and Duma, S.M., 2008, The effects of the extraocular muscles on eye impact force-deflection and globe rupture response: Journal of Biomechanics, v. 41, pp. 3297-3302.
- Kuhn, F., Morris, F., Witherspoon, C.D., and Mester, V., 2004, The Birmingham eye trauma terminology system (BETT): J. Fr. Ophthalmology, v. 27, pp. 206-210.
- Liu, X., Wang, L., Wang, C. et al., 2013. Mechanism of traumatic retinal detachment in blunt impact: a finite element study. *Journal of Biomechanics*: v. 46, pp.1321–1327.
- Mader, T.H., Carroll, R.D., Slade, C.S., George, R.K., Ritchey, J.P., and Neville, S.P. 2006, Ocular war injuries of the Iraq insurgency, January-September 2006. *Ophthalmology*, v. 113, pp. 97-104.
- Panzer, M.B., Myers, B.S., and Bass, C.R., 2013, Mesh considerations for finite element blast modelling in biomechanics. *Computer Methods in Biomechanics and Biomedical Engineering*: v. 16, pp.612–621, 2013. PMID: 22185582.
- Petras, J.M., Bauman, R.A., and Elsayed, N.M., 1997, Visual system degeneration induced by blast overpressure: *Toxicology*, v. 121, pp. 41-49.

- Pieramici, D., Sternberg, P. Aaberg, T.M et al, 1997, A system for classifying mechanical injuries of the eye (globe): American Journal of Ophthalmology, v.123, pp. 820-831.
- Proud, W.G., Goldein, H.T., Esmail, S., and Willianson, D.M., 2009, A review of wound ballistics literature: the human body and injury processes: Security and Use of Innovative Technologies Against Terrorism (Teixeria-Das et al., Editors), Universidade de Aveiro, pp. 67-82.
- Richmond, D.R., and White, C. S., 1962, A tentative estimation of Man's tolerance to overpressures from air blast: Lovelace Foundation for Medical Education and Research, 34 p.
- Richmond, D.R., Damon, E.G., Fletcher, E.R., Bowen, I.G., and White, C.S., 1966, The relationship between selected blast-wave parameters and the response of mammals exposed to air blast: Lovelace Foundation for Medical Education and Research, 36 p.
- Richmond, D.R., Yelverton, J.T., Fletcher, E.R., and Phillips, Y.Y., 1985, Biologic response to complex blast wave: Ninth International Symposium MABS 9, Oxford, England (Los Alamos Report 20000926 077).
- Reilly, M.A., Hamilton, P.D., Perry, G, and Ravi, N., 2009. Comparison of the behavior of natural and refilled porcine lenses in a robotic lens stretcher: *Experimental Eye Research*. V 88(, pp. 483–494.
- Rossi, T., 2011. The pathogenesis of retinal damage in blunt eye trauma. *Investigative Ophthalmology*: v. 52, pp.3994–4002.
- Rossi, T., 2012, Primary blast injury to the eye and orbit: Finite element modeling: *Investigative Ophthalmology*: v. 53, pp. 8057–8066.
- Sanchez, R., Martin, R., Ussa, F., and Fernandez-Bueno, I., 2011, The parameters of the porcine eyeball. *Graefe's Archive for Clinical and Experimental Ophthalmology*: v. 249, pp.475–482.
- Sherwood D, Sponsel WE, Lund BJ et al. 2014, Anatomical manifestations of primary blast ocular trauma observed in postmortem porcine model: *Investigative Ophthalmology and Visual Science* 2014; v. 55, pp.1124-1132.
- Sigal, I.A., Flanagan, J.G., Tertinegg, I., and Ether, C.R., 2005, Factors influencing nerve head biomechanics: *Investigative Ophthalmology and Visual Science*, v. 46, pp. 4189-4199.

Sponsel, W.E., Gray, W., Scribbick, F.W., Stern, A.R., Weiss, C.E., Groth, S.L., and Walker, J.D., 2011, Blunt eye trauma: Empirical histopathologic paintball impact thresholds in fresh mounted porcine eyes: *Investigative Ophthalmology and Visual Science*, v. 52, pp. 5157-5166.

Stuhmiller, J.H., 2008a, Blast Injury: Translating research into operational medicine: *Textbook of Military medicine*, Borden Research Institute.

Stuhmiller, J.H., 2008b, Blast Injury: Translating research into operational medicine: Chapter 10, *Ophthalmic Care of the Combat Casualty*, *Textbook of Military medicine*, Borden Research Institute.

Stewart, C., 2006, Blast injuries: Preparing for the inevitable: *Emergency Medicine Practice*, v 8, pp.1-28.

Thach, et al., 1999, Ocular injuries from paintball pellets: *Ophthalmology*, v. 106, pp. 533-537.

Thach, et al., 2008, Severe eye injuries in the War in Iraq, 2003-2005, *Ophthalmology*, v. 115, pp. 377-382.

Uchio, E., Ohno, S. Kudoh, J., Aoki, K., Andoh, K., and Kisielewicz, L.T., 1999, Simulation model of an eye based on finite element analysis on a supercomputer: *British Journal of Ophthalmology*, v. 83, pp. 1106-111.

Weichel, E.D., Colyer, M.H., Baustista C., Bower, K.S., and French, L.M., 2009, Traumatic brain injury associated with combat ocular trauma: *Journal of Head Trauma Rehabilitation*, v. 24, pp. 41-50.

Yang J, Caprioli RM. Matrix sublimation/recrystallization for imaging proteins by mass spectrometry at high spatial resolution. *Analyt. Chem.* 83:5728-5734, 2011.

Yoo L, Reed J, Shin A, et al. 2011, Characterization of ocular tissues using microindentation and hertzian viscoelastic models: *Investigative Ophthalmology and Visual Science*, v. 52, pp. 3475-3482.

APPENDIX I

Summary of Porcine Blast Experiments and Observed Trauma

Disk refers to the number of aluminum or Mylar sheets used in the driver section of the shock tube. The larger the number of disks, the greater is the peak pressure, specific impulse, and energy of the blast wave.

Summary of Observed Trauma – 6 Disk at 42 cm

Experiment Set	20130411-1	20130411-2	20130411-2	20130417-6	20130502-1	20130502-4	20130502-5	20130711-3'
Eye #	1	2	1	6	1	4	5	3
Purpose	Shot	Shot	Shot	Shot	Shot	Shot	Shot	Shot
Orientation	Right	Right	Right	Right	Right	Right	Right	Left
Pre-Inflation (g)	11.7	11.4	6.4	6.3	8.7	8.2	6.6	
Post-Inflation (g)	12.3	11.5	6.5	6.3	8.7	8.4	6.8	7.3
Inflation Method	Pars Plana	Pars Plana	Pars Plana	Pars Plana	Pars Plana	Pars Plana	Pars Plana	Pars Plana
Raised IOP (mmHg)	87	86	22	46	82	37	85	87
Pre- Blast IOP (mmHg)	10	9	13	32	22	10	51	18
Post Blast-IOP (mmHg)	9	6	5	*too low to	14	6	27	9
Post-Blast Storage	Hank's BSS	Hank's BSS	Hank's BSS	Hank's BSS	Hank's BSS	Hank's BSS	Hank's BSS	Hank's BSS
Exposed Area (sq meter)	0.00049564	0.00045262	0.00042862	0.0003976	0.00046807	0.00044155	0.0003648	0.000292
# Discs	6	6	6	6	6	6	6	6
Reference P_Max (kPa)	199.9	207.4	242.5	245.9	238.6	256.5	214.3	238.4
Reference Duration (ms)	3.54	3.45	3.43	3.56	3.46	3.49	3.52	4.36
Reference Impulse (Pa-sec)	270.1	267.9	285.9	272.8	299	309.3	291.5	323.6
Total P_Max (kPa)	432.6	472.3	554.1	602.3	587	617.9	487.2	518.1
Total Impulse (Pa-s)	487.2	502.1	558.9	522.8	593.9	638.7	564.7	587
Total Duration (ms)	4.14	4.01	4.26	4.08	4.44	4.24	4.48	4.3
Energy (J)	2.370348205	2.24553634	4.41438016	3.42920434	4.44118655	4.73417523	3.1207138	2.01228296
Angle	1	0	0	1	0	0	0	0
Anterior Chamber	0	0	0	0	0	0	0	0
Choroid	0	2	2	0	0	0	0	4
Chorioretina	2	2	2	2	0	0	0	4
Cornea	0	0	0	0	0	0	0	0
Iris	0	0	0	0	0	0	0	0
Lamina Cribosa	0	0	0	0	0	0	0	0
Lens	0	0	0	0	0	0	0	0
Optic Nerve	0	1	2	0	0	0	0	3
Retina	1	2	1	1	0	0	0	4
Sclera	0	0	0	0	0	0	0	1

Summary of Observed Trauma – 6 Disk

Experiment Set	20130110-4	20130124-5	20130131-7	20130613-1	20130620-1
Eye #	4	5 (e?)	7	1	1
Purpose	Shot	Shot	Shot	Shot	Shot
Orientation	Right	Right	Right	Left	Right
Pre-Inflation (g)				10.4	9
Post-Inflation (g)	6.39975	8.03525	5.0745	10.5	9
Inflation Method	Anterior Chamber	Anterior Chamber	Anterior Chamber	Pars Plana	Pars Plana
Raised IOP (mmHg)	23	13	65	51	74
Pre- Blast IOP (mmHg)	4	4	12	5	14
Post Blast-IOP (mmHg)		*too low to	5	*too low to	9
Post-Blast Storage	Plastic Bag	Plastic Bag	Plastic Bag	Hank's BSS	Hank's BSS
Exposed Area (sq meter)	0.00025599	0.00032141	0.00020298	0.00052621	0.00052087
# Discs	6	6	6	6	6
Reference P_Max (kPa)	151.8	155.8	147.2	147.5	155.3
Reference Duration (ms)	2.76	2.78	2.72	2.79	2.9
Reference Impulse (Pa-sec)	190.6	193.5	188.9	186.9	190
Total P_Max (kPa)	289	287.5	289.2	290	307.8
Total Impulse (Pa-s)	289	294.8	286.3	286	291.7
Total Duration (ms)	3.11	3.16	3.14	3.33	3.35
Energy (J)	0.42761082	0.55865583	0.33275603	1.07852686	1.28250493
Angle	0	2	0	0	0
Anterior Chamber	0	0	0	0	0
Choroid	4	0	2	3	0
Chorioretina	4	0	2	3	0
Cornea	0	0	0	0	0
Iris	0	0	0	0	0
Lamina Cribosa	0	0	0	0	0
Lens	0	0	0	0	0
Optic Nerve	4	0	0	0	0
Retina	4	0	2	3	0
Sclera	1	1	3	3	0

Summary of Observed Trauma – 5 Disk

Experiment Set	20130110-3	20130117-2	20130124-7	20130207-8	20130405-1	20130606-1	20130613-2
Eye #	3	2	7	8	1	1	2
Purpose	Shot	Shot	Shot	Shot	Shot	Shot	Shot
Orientation	Right		Right		Left	Right	Right
Pre-Inflation (g)					8.1	8.6	9.9
Post-Inflation (g)	6.944	5.064	7.24175	8	8.5	8.7	9.9
Inflation Method	Anterior Chamber	Anterior Chamber	Anterior Chamber	Pars Plana	Pars Plana	Pars Plana	Pars Plana
Raised IOP (mmHg)	17	9	43	24	87	58	85
Pre- Blast IOP (mmHg)	5	4	7	42	13	5	44
Post Blast-IOP (mmHg)			6		9	6	31
Post-Blast Storage	Plastic Bag	Plastic Bag	Plastic Bag	Hank's BSS	Hank's BSS	Hank's BSS	Hank's BSS
Exposed Area (sq meter)	0.00027776	0.00020256	0.00028967	0.00032	0.00030454	0.00049362	0.0004078
# Discs	5	5	5	5	5	5	5
Reference P_Max (kPa)	152.4	134.3	138.9	137.8	126.1	140	135.2
Reference Duration (ms)	2.67	2.58	2.68	2.5	2.5	2.79	2.61
Reference Impulse (Pa-sec)	162.8	165.5	171.4	158.1	147.8	169.5	164.7
Total P_Max (kPa)	251.1	256.8	259.6	271.3	221.6	271.4	248.9
Total Impulse (Pa-s)	238.4	239.8	252.7	230.7	210.9	253.8	242.3
Total Duration (ms)	3.01	3.07	3.1	3.11	2.96	3.15	3.05
Energy (J)	0.31572735	0.23296037	0.36995082	0.34062394	0.24265706	0.90202689	0.4929803
Angle	0	0	2	0	3	0	0
Anterior Chamber	0	0	0	0	3	0	0
Choroid	4	4	0	0	4	0	0
Chorioretina	4	4	2	1	4	0	1
Cornea	0	0	0	0	0	0	0
Iris	0	0	0	0	2	0	0
Lamina Cribosa	0	0	0	0	0	0	0
Lens	0	0	0	0	1	0	0
Optic Nerve	2	4	4	0	3	0	0
Retina	3	4	4	1	3	0	0
Sclera	3	2	2	1	0	0	1

Summary of Observed Trauma – 4 Disk

Experiment Set	20130117-4	20130131-3	20130405-2	20130606-3	20130613-4	20130620-2
Eye #	4	3	2	3	4	2
Purpose	Shot	Shot	Shot	Shot	Shot	Shot
Orientation	Right	Left	Right	Left	Left	Left
Pre-Inflation (g)			7.7	8.5	8.2	10.2
Post-Inflation (g)	5.8735	5.65025	8.3	8.8	8.3	10.5
Inflation Method	Anterior Chamber	Anterior Chamber	Pars Plana	Pars Plana	Pars Plana	Pars Plana
Raised IOP (mmHg)	11	48	64	84	84	54
Pre- Blast IOP (mmHg)	24	9	6	11	14	5
Post Blast-IOP (mmHg)		*too low to	4	9	11	5
Post-Blast Storage	Plastic Bag	Plastic Bag	Hank's BSS	Hank's BSS	Hank's BSS	Hank's BSS
Exposed Area (sq meter)	0.00023494	0.00022601	0.00034767	0.00054458	0.00049454	0.00053059
# Discs	4	4	4	4	4	4
Reference P_Max (kPa)	119.2	136.6	113.1	117.3	116.1	122.9
Reference Duration (ms)	2.56	2.49	2.42	2.55	2.58	2.53
Reference Impulse (Pa-sec)	136.4	146.8	128.4	143.8	143.3	144.1
Total P_Max (kPa)	214.9	233.1	191	209.2	215	221.2
Total Impulse (Pa-s)	190.5	207.4	177.2	203.6	203.2	206.8
Total Duration (ms)	2.99	2.97	2.93	2.99	2.97	3.02
Energy (J)	0.17052063	0.19443532	0.22864083	0.69849975	0.60833411	0.5733237
Angle	0	4	4	0	0	0
Anterior Chamber	1	2	4	0	0	0
Choroid	2	2	4	0	0	3
Chorioretina	2	2	4	0	0	3
Cornea	0	0	0	0	0	0
Iris	0	0	0	0	0	0
Lamina Cribosa	0	0	0	0	0	0
Lens	0	0	1	0	0	0
Optic Nerve	0	0	4	0	0	3
Retina	1	4	4	0	0	0
Sclera	1	4	2	0	0	3

Summary of Observed Trauma – 3 Disk

Experiment Set	20130110-2	20130131-2	20130405-5	20130606-4	20130613-5	20130620-5
Eye #	2	2	5*	4	5	5
Purpose	Shot	Shot	Shot	Shot	Shot	Shot
Orientation	Right	Right	Right	Right	Right	Right
Pre-Inflation (g)			6.9	8.4	8.3	7.7
Post-Inflation (g)	5.28425	5.04	7.6	8.4	8.1	7.7
Inflation Method	Anterior Chamber	Anterior Chamber	Pars Plana	Pars Plana	Pars Plana	Pars Plana
Raised IOP (mmHg)	17	37	23	56	85	74
Pre- Blast IOP (mmHg)	14	9	5	10	8	9
Post Blast-IOP (mmHg)		5	4	9	6	10
Post-Blast Storage	Plastic Bag	Plastic Bag	Hank's BSS	Hank's BSS	Hank's BSS	Hank's BSS
Exposed Area (sq meter)	0.00021137	0.0002016	0.00034917	0.00043689	0.00049647	0.00047815
# Discs	3	3	3	3	3	3
Reference P_Max (kPa)	99.6	99.8	90	101.2	98.5	101.8
Reference Duration (ms)	2.44	2.43	2.39	2.47	2.48	2.47
Reference Impulse (Pa-sec)	113	114.5	100.4	116.1	116.8	119
Total P_Max (kPa)	170.3	184.5	158.7	176	172.6	174.6
Total Impulse (Pa-s)	147.7	150.1	130.7	157.2	157.1	160.9
Total Duration (ms)	2.64	2.89	2.65	2.75	2.72	2.74
Energy (J)	0.09222196	0.090841	0.1370192	0.28076309	0.37551162	0.38434363
Angle	0	0	0	0	0	0
Anterior Chamber	0	0	0	0	0	0
Choroid	1	0	0	3	4	0
Chorioretina	1	0	0	3	4	0
Cornea	0	0	0	0	0	0
Iris	0	0	0	0	0	0
Lamina Cribosa	0	0	0	0	0	0
Lens	0	0	0	0	0	0
Optic Nerve	1	0	0	2	4	0
Retina	1	0	0	3	4	0
Sclera	0	0	0	0	4	0

Summary of Observed Trauma – 2 Disk

Experiment Set	20130124-2	20130131-4	20130307-6	20130405-6	20130502-7	20130606-5	20130620-6
Eye #	2	4	6	6'	2	5	6
Purpose	Shot	Shot	Shot	Shot	Shot	Shot	Shot
Orientation	Right	Right	Left	Left	Right	Right	Left
Pre-Inflation (g)			8.9	7.1	7.9	8.7	9.3
Post-Inflation (g)	8.04275	5.15375	8.90775	7.3	7.9	8.7	9.5
Inflation Method	Anterior Chamber	Anterior Chamber	Pars Plana	Pars Plana	Pars Plana	Pars Plana	Pars Plana
Raised IOP (mmHg)	*too high to	34	56	89	86	85	47
Pre- Blast IOP (mmHg)	8	5	18	10	15	10	5
Post Blast-IOP (mmHg)	7	*too low to	13	6	10	4	9
Post-Blast Storage	Plastic Bag	Plastic Bag	Hank's BSS	Hank's BSS	Hank's BSS	Hank's BSS	Hank's BSS
Exposed Area (sq meter)	0.00032171	0.00020615	0.00035631	0.00035505	0.00040219	0.0005036	0.0004843
# Discs	2		2	2	2	2	2
Reference P_Max (kPa)	82.8		78.1	70.4	116.1	78	77.7
Reference Duration (ms)	2.35		2.26	2.32	3.08	2.39	2.3
Reference Impulse (Pa-sec)	93.61		88.46	80.61	140.3	86.71	86.54
Total P_Max (kPa)	144.7	140.3	139.1	129	242.3	142	138.3
Total Impulse (Pa-s)	116.8	112.1	111.3	99.96	204.5	111.2	110.7
Total Duration (ms)	2.55	2.46	2.48	2.42	3.33	2.65	2.64
Energy (J)	0.0877769	0.05181131	0.08827716	0.08627375	0.42814618	0.18023194	0.1512637
Angle	0	0	0	0	0	0	0
Anterior Chamber	0	0	0	0	0	0	0
Choroid	0	2	0	0	0	0	0
Chorioretina	0	2	1	0	0	0	1
Cornea	0	0	0	0	0	0	0
Iris	0	0	0	0	0	0	0
Lamina Cribosa	0	0	0	0	0	0	0
Lens	0	0	0	0	0	0	0
Optic Nerve	0	0	0	0	0	0	0
Retina	0	2	0	0	0	1	0
Sclera	0	0	0	0	0	0	1

Summary of Observed Trauma – 1 Disk

Experiment Set	20130110-1	20130117-3	20130307-5	20130328-7
Eye #	1	3	5**	7*
Purpose	Shot	Shot	Shot	Shot
Orientation	Left		Left	Right
Pre-Inflation (g)			8	8.3
Post-Inflation (g)	6.912	5.34725	11.0705	8.5
Inflation Method	Anterior Chamber	Anterior Chamber	Pars Plana	Pars Plana
Raised IOP (mmHg)	22	19	49	87
Pre- Blast IOP (mmHg)	4		38	69
Post Blast-IOP (mmHg)		6	45	44
Post-Blast Storage	Plastic Bag	Plastic Bag	Hank's BSS	Hank's BSS
Exposed Area (sq meter)	0.00027648	0.00021389	0.00044282	0.00026661
# Discs	1	1	1	1
Reference P_Max (kPa)	49.3	47.4	50.2	46.3
Reference Duration (ms)	2.15	2.23	2.08	2.07
Reference Impulse (Pa-sec)	52.98	53.37	52.2	48.31
Total P_Max (kPa)	91.9	86	96.4	79.7
Total Impulse (Pa-s)	60.27	61.04	60.21	55.65
Total Duration (ms)	2.22	2.26	2.17	2.18
Energy (J)	0.02008612	0.01593858	0.03210661	0.01294894
Angle	0	0	3	0
Anterior Chamber	0	0	2	0
Choroid	2	3	0	0
Chorioretina	2	2	0	0
Cornea	0	0	0	0
Iris	0	0	0	0
Lamina Cribosa	0	0	0	0
Lens	0	0	0	0
Optic Nerve	2	2	0	0
Retina	2	2	0	0
Sclera	0	1	0	0

Summary of Observed Trauma – Mylar Disk

Experiment Set	20130117-6	20130124-6	20130307-7	20130328-2	20130606-6
Eye #	6	6	7	2*	6
Purpose	Shot	Shot	Shot	Shot	Shot
Orientation	Right	Right	Right	Right	Right
Pre-Inflation (g)			9.5	7.5	7.7
Post-Inflation (g)	7.12175	6.525	10.97925	8	7.7
Inflation Method	Anterior Chamber	Anterior Chamber	Pars Plana	Pars Plana	Pars Plana
Raised IOP (mmHg)	57	44	47	87	-
Pre- Blast IOP (mmHg)	9	8	38	4	10
Post Blast-IOP (mmHg)	6	6	29	*too low to	-
Post-Blast Storage	Plastic Bag	Plastic Bag	Hank's BSS	Hank's BSS	Hank's BSS
Exposed Area (sq meter)	0.00028487	0.000261	0.00043917	0.00037511	0.00051186
# Discs	0.5	0.5	0.5		0.5
Reference P_Max (kPa)	23.8	21.8	42.3		37.6
Reference Duration (ms)	2.12	2.16	2.07		2.23
Reference Impulse (Pa-sec)	27.36	26.7	44.87		41.46
Total P_Max (kPa)	49.1	48.6	85.4	55.5	76.2
Total Impulse (Pa-s)	29.58	28.75	51.16	30.05	48.35
Total Duration (ms)	2.23	2.19	2.21	2.09	2.28
Energy (J)	0.00498509	0.00431466	0.02298919	0.0079412	0.03977174
Angle	0	0	2	0	0
Anterior Chamber	0	0	2	0	0
Choroid	0	4	2	0	0
Chorioretina	0	4	2	0	1
Cornea	0	0	0	0	0
Iris	0	0	0	0	0
Lamina Cribosa	0	0	0	0	0
Lens	0	0	1	0	0
Optic Nerve	0	3	3	0	0
Retina	0	4	3	0	0
Sclera	0	0	4	0	0

Summary of Observed Trauma – Controls

Experiment Set	20130110-5	20130117-5	20130124-8	20130131-1	20130307-8	20130328-64a	20130328-64b	20130405-7	20130411-4	20130417-8	20130502-8	20130613-6	20130620-8
Eye #	5	5	8	1	8	6,4a	6,4b	7	4	8	8	6	8
Purpose	Shock Tube	Shock Tube	Shock Tube	Shock Tube	Shock Tube	Shock Tube C	Shock Tube C	Shock Tube	Shock Tube	Shock Tube	Shock Tube	Shock Tube	Shock Tube
Orientation	Right	Left		Right	Left	Right	Right	Right	Right	Right	Left		Right
Pre-Inflation (g)					9.9	7.3	7.8	7.7	12.4	6.6	8.2	7.4	7.2
Post-Inflation (g)						7.6	8	8.3	12.5	6.9	8.2	7.4	7.2
Inflation Method	Anterior Chamber	Anterior Chamber	Anterior Chamber	Anterior Chamber	Pars Plana	Pars Plana	Pars Plana	Pars Plana	Pars Plana	Pars Plana	Pars Plana	Pars Plana	Pars Plana
Raised IOP (mmHg)	27	9	41	38	39	87	98	44	86	61		85	78
Pre- Blast IOP (mmHg)	*too low to	5	10	12	*too low to	14	6	6	20	6	12	12	24
Post Blast-IOP (mmHg)		4	8	11	*too low to	10	4	4	13	*too low to	10	12	12
Post-Blast Storage	Plastic Bag	Plastic Bag	Plastic Bag	Plastic Bag	Hank's BSS	Hank's BSS	Hank's BSS	Hank's BSS	Hank's BSS	Hank's BSS	Hank's BSS	Hank's BSS	Hank's BSS
Exposed Area (sq meter)	0.00023117	0.00021389	0.00032233	0.00020802	0.00059998	0.00036811	0.00036921	0.00031351	0.00043906	0.00036963	0.0003225	0.0003748	0.0005271
# Discs	0	0	0	0	0	0	0	0	0	0	0	0	0
Reference P_Max (kPa)	0	0	0	0	0	0	0	0	0	0	0	0	0
Reference Duration (ms)	0	0	0	0	0	0	0	0	0	0	0	0	0
Reference Impulse (Pa-sec)	0	0	0	0	0	0	0	0	0	0	0	0	0
Total P_Max (kPa)	0	0	0	0	0	0	0	0	0	0	0	0	0
Total Impulse (Pa-s)	0	0	0	0	0	0	0	0	0	0	0	0	0
Total Duration (ms)	0	0	0	0	0	0	0	0	0	0	0	0	0
Energy (J)	0	0	0	0	0	0	0	0	0	0	0	0	0
Angle	0	0	0	0	0	4	0	0	0	0	0	0	0
Anterior Chamber	0	0	0	0	0	0	0	0	0	0	0	0	0
Choroid	2	0	0	0	0	1	0	3	3	3	0	0	0
Chorioretina	2	0	0	0	0	1	0	3	3	3	0	0	0
Cornea	0	0	0	0	0	0	0	0	0	0	0	0	0
Iris	0	0	0	0	0	0	0	0	0	0	0	0	0
Lamina Cribosa	0	0	0	0	0	0	0	0	0	0	0	0	0
Lens	0	0	0	0	0	0	0	0	0	0	0	0	0
Optic Nerve	3	0	0	0	0	0	0	1	3	2	0	0	0
Retina	2	0	0	0	0	1	0	3	3	4	0	0	0
Sclera	1	0	0	0	1	4	0	0	0	0	0	0	0

ABSTRACT

This report summarizes the results for all tasks undertaken during Year 1 and 2 of the project “Sub-lethal Ocular Trauma (SLOT): Establishing a Standardized Blast Threshold to Facilitate Diagnostic, early Treatment, and Recovery Studies for Blast Injuries to the Eye and Optic Nerve.” The project is funded by the U.S. Army Medical Research and Materiel Command as Vision Research Program (VRP) Grant W81XWH-12-2-0055. The three year effort aims to fill a gap in our understanding of the physical mechanisms and progression of primary blast-induced ocular trauma. Although ocular injuries resulting from penetration of blast-driven fragments and debris (secondary blast) are well documented and understood, injuries resulting from only the air shock or blast wave (primary blast) have to date received little attention.

Our approach is a fully-integrated experimental and computational study; with blast experiments conducted using the U.S. Army Institute of Surgical Research (ISR) large diameter shock tube, and experiments fully supported with computational analysis using physics-based codes CTH and LS-DYNA. The simulations carefully mimic the experiments with the goal of fully reproducing the trauma observed in the experiments. Experiments increased in complexity from *ex vivo* porcine eyes in Year 1 of the study to *in vivo* rabbit eyes in Year 2. Use of the *in vivo* rabbit model will allow for biochemical marker monitoring and characterization. The project will culminate in Year 3 with development of trauma predictive models. The data generated during the experiments will be used to formulate empirical models useful in predicting the probability of observing a number of sub-globe-rupture injuries under various blast pressure-impulse or energy environments.

Tasks completed to date include (1) development of detailed procedures for preparation and blast testing of eye specimens and the conduct of 85 shock tube experiments on porcine eyes, (2) completion of pathology on the porcine eye specimens, (3) preliminary development of trauma risk curves for a number of sub-globe-rupture trauma categories, (4) preliminary numerical simulations using software packages CTH and LS-DYNA, (5) validation and approval of *in vivo* rabbit blast test protocol and completion of 13 blast experiments, (6) recovery and mounting of optic nerve specimens in preparation for imaging using the Matrix Assisted Laser Desorption Ionization (MALDI) technique, and (7) identification of potential fluid- and tissue-based biomarkers.

The project is being undertaken as a collaborative research effort between personnel from the University of Texas at San Antonio, the U.S. Army Institute of Surgical Research (Ocular Trauma Division), the University of Texas Health Science Center-San Antonio, and the Sponsel Professional Association of San Antonio. The data and predictive models generated to date have significantly increased our understanding of blast-induced ocular injury. The shock tube produced a broad array of closed-globe injuries, many of which would seriously compromise visual function. The experimental techniques and injury characterization methodologies offer an objective assessment as to which injuries were due to primary blast exposure.